

## **Copyright Undertaking**

This thesis is protected by copyright, with all rights reserved.

## By reading and using the thesis, the reader understands and agrees to the following terms:

- 1. The reader will abide by the rules and legal ordinances governing copyright regarding the use of the thesis.
- 2. The reader will use the thesis for the purpose of research or private study only and not for distribution or further reproduction or any other purpose.
- 3. The reader agrees to indemnify and hold the University harmless from and against any loss, damage, cost, liability or expenses arising from copyright infringement or unauthorized usage.

#### **IMPORTANT**

If you have reasons to believe that any materials in this thesis are deemed not suitable to be distributed in this form, or a copyright owner having difficulty with the material being included in our database, please contact <a href="mailto:lbsys@polyu.edu.hk">lbsys@polyu.edu.hk</a> providing details. The Library will look into your claim and consider taking remedial action upon receipt of the written requests.

# DYNAMIC HEAT AND MASS TRANSFER CHARACTERIZATION AND PERFORMANCE ENHANCEMENT OF ABSORPTION THERMAL ENERGY STORAGE SYSTEM

# LIN YAO

PhD

The Hong Kong Polytechnic University

2025

The Hong Kong Polytechnic University			
Department of Building Environment and Energy Engineering			
Dynamic Heat and Mass Transfer Characterization and Performance Enhancement of Absorption Thermal Energy Storage System			
Lin Yao			

A thesis submitted in partial fulfillment of the requirements for the Degree of Doctor of Philosophy

August, 2024

# **CERTIFICATE OF ORIGINALITY**

I hereby declare that this thesis is my own work and that, to the best of my knowledge and
belief, it reproduces no material previously published or written, nor material that has been
accepted for the award of any other degree or diploma, except where due acknowledgement
has been made in the text.
(Signed)
LIN Yao (Name of student)

**ABSTRACT** 

Abstract of thesis entitled: Dynamic Heat and Mass Transfer Characterization and Performance

Enhancement of Absorption Thermal Energy Storage System

Submitted by: LIN Yao

For the degree of: Doctor of Philosophy

at The Hong Kong Polytechnic University in August 2024

The pursuit of sustainable energy solutions has led to the development of advanced thermal

energy storage (TES) systems. Among various TES technologies, absorption TES offers

several advantages over sensible and latent TES, including high energy storage density (ESD),

minor heat loss, high flexibility, and potential for long-term and mobilized storage. The ESD

is the main performance criterion of the absorption TES system. Expanding the concentration

difference of the working fluids is recognized as the most effective method for enhancing ESD.

However, the large concentration difference could also increase the crystallization risks, which

poses a challenge to the exploitation of ESD potential in current research. Besides, despite the

promising ESD potential indicated by thermodynamic modeling in existing studies, there is a

scarcity of experimental studies examining the dynamic characteristics and energy

performance of the absorption TES systems. The main reasons lie in insufficient heat and mass

transfer performance within the heat exchangers, which are critical components of the

absorption TES system.

Therefore, this research aims to enhance the ESD of the absorption TES system at material,

cycle, component, and system levels. The main works and contributions of this research are

detailed as follows.

iv

Firstly, a novel modified LiCl solution is developed for three-phase absorption thermal energy storage. Ethylene glycol (EG) and silica nanoparticles (SNPs) are introduced as additives into the LiCl solution. EG enhances the solubility of LiCl, while SNPs facilitate the growth suspension of fine LiCl crystal slurry in the saturated LiCl solution. The effects of EG and SNPs on the thermal and physical properties of LiCl solution are investigated. A three-phase absorption TES cycle using novel working fluids is proposed, and the ESD of the modified solution is assessed. The results show that the modified working fluids have a significant ESD enhancement potential.

Secondly, a closed absorption TES test rig with novel designed heat exchangers has been built. The dynamic heat and mass transfer characteristics and the energy performance of the two-phase absorption TES system are studied experimentally. The impact of the mass fraction of EG and working conditions are revealed experimentally. The results show that the ESD ranges from 108-177 kWh/m<sup>3</sup> at different working scenarios, with an enhancement of 18-48%.

Thirdly, experimental studies of three-phase absorption TES are conducted. The dynamic charging and discharging characteristics and performance evaluation of the three-phase absorption TES system are conducted experimentally. The ESD is further enhanced by 19.3%-80.3% compared with two-phase absorption TES. After that, a closed three-phase absorption TES model is developed and validated using experimental data. The model is then used to simulate the performance under all working conditions, providing a comprehensive understanding of the system's capabilities.

Finally, the proposed closed three-phase absorption TES system using novel working fluids is investigated with a distributed energy system. An enhanced load following strategy considering the state of storage system is proposed for system capacity design and operational control. The dynamic response, storage performance, and energy-saving potentials are investigated on the

TRNSYS simulation platform, which further extends the application of the absorption TES system.

This PhD study can be regarded as a seminal work in the research field, providing substantial and valuable insights and references for absorption thermal energy storage, with focuses on working fluids modification, dynamic heat and mass transfer characterization, experimental investigation on cycle performance, and the integration with distributed energy system. Additionally, it has the potential to catalyze the development of related industries, especially heat exchanger and absorption machine industry.

## PUBLICATIONS ARISING FROM THE THESIS

## **Journal Papers**

- [1] **Yao Lin**, Fu Xiao\*, and Shengwei Wang. "A novel modified LiCl solution for three-phase absorption thermal energy storage and its thermal and physical properties." *International Journal of Refrigeration*. 130 (2021): 44-55.
- [2] **Yao Lin**, Fu Xiao\*, Shengwei Wang, and Lingshi Wang. "Experimental study on a closed absorption thermal energy storage system using modified LiCl solution for enhancing energy storage density." *Journal of Energy Storage*. 103 (2024): 114551.
- [3] **Yao Lin**, Fu Xiao\*, Lingshi Wang\*, and Shengwei Wang. "Experimental investigation and performance evaluation of a closed three-phase absorption thermal energy storage system." *Energy*. 313 (2024): 134038.
- [4] **Yao Lin**, Fu Xiao\*, and Shengwei Wang. "Enhanced load following strategy for capacity design and operational control of absorption thermal energy storage in distributed energy systems" (to be submitted)

## **Conference Papers**

- [1] **Yao Lin,** Fu Xiao\*, and Shengwei Wang. Novel LiCl solutions for crystallization control in LiCl/H<sub>2</sub>O absorption system. *Proceedings of International Sorption Heat Pump Conference 2021*. In: ISHPC 2021. Berlin, Germany; Aug 21<sup>th</sup>, 2021.
- [2] **Yao Lin**, Fu Xiao\*, and Shengwei Wang. "A mobilized three-phase absorption thermal energy storage system for district heating and cooling supply." *Energy Proceedings of the 15th International Conference on Applied Energy*, 2024. In: ICAE 2023. Doha, Qatar; Dec. 4<sup>th</sup>, 2023.

## ACKNOWLEDGMENTS

More than six years have passed since I first came to Hong Kong. Back then, I had just completed my undergraduate study. Now, with the final page of this dissertation settled into place, I find myself standing on a stage I could scarcely have imagined. I believe this journey is unforgettable, not because of the difficulties I encountered or the knowledge and experience I gained, but more because of the people and moments I met along the way. They were like stars that illuminated my path and ultimately nourished me from within.

My deepest gratitude goes to my supervisor, Prof. Shengwei WANG, and my co-supervisor, Prof. Fu XIAO. They have supported me continuously throughout my Ph.D. study. From the first discussion to the final stop, they have guided me with insight, patience, and kindness. Their academic acumen opened new horizons, their questions sharpened my thinking, and their encouragement carried me through every delay and detour. Even when I faced setbacks and felt depressed, they remained steady and supportive. I also witnessed their devotion and passion for their careers, which have inspired me in both pursuing the degree and personal life.

I am likewise grateful to all team members and former colleagues in our research group for walking beside me throughout my Ph.D. study. Together, we attended classes and group meetings, exchanged ideas on both research and personal development. We also shared many joyful hours in life beyond work. We climbed hills, dived into the ocean, and embraced sunsets over the Hong Kong skyline. In those conversations and adventures, we forged friendships that will last a lifetime.

The main body of this thesis comes from experimental studies. Designing, building, and commissioning the test rig took three and a half years, much of which I worked on alone because of COVID-19. Throughout this process, I faced many practical challenges, including company closures, contract disputes, workers' strikes, and an ammonia leak accident at the

factory. A string of equipment failures also once disappointed and discouraged me. For a long time, my experimental progress was stalled due to force majeure. I was powerless to change anything and could only remain optimistic. But luckily, the experiments were ultimately completed through continual effort. I owe special thanks to Mr.Fuchang HUO, Dr. Junming ZHOU, Dr. Lingshi WANG, Dr. Xiuming LI, and Dr. Chong ZHANG. Their practical and perceptive advice—shared throughout the experiments and during the drafting of the papers—was vital to bringing the experiments to completion and to shaping this dissertation. Books I read during those days were another quiet source of strength, reminding me that perseverance is itself a kind of victory.

I would also like to express my special thanks to Prof. Lizhi Zhang from South China University of Technology and his team. Conducting part of my early experiments in their laboratory accelerated my progress and broadened my knowledge. I am also grateful to Prof. Chengbin Zhang from Southeast University and his students. We conducted experiments in the same factory and experienced some of the same hardships together; they offered help and suggestions unselfishly whenever I was in need.

Last but not least, I would like to express my appreciation to my parents and all my family members for their support and understanding throughout my growth. Especially my wife, Miss Yuman Liu, who has accompanied and supported me through more than eight years of both challenge and delight. Her unconditional love, consistent encouragement, and support have sheltered me when I drifted. We have journeyed from dearest friends and lovers to family. May the road ahead unfold beneath our shared compass.

To everyone who lent time, wisdom, or encouragement, this thesis carries your imprint.

# TABLE OF CONTENTS

CERTIFIC.	ATE OF ORIGINALITY	iii
ABSTRAC	T	iv
PUBLICAT	TIONS ARISING FROM THE THESIS	vii
ACKNOW	LEDGMENTS	viii
TABLE OF	CONTENTS	x
LIST OF F	IGURES	xiii
LIST OF T	ABLES	xvi
Chapter 1	Introduction	1
1.1 M	otivation	1
1.2 Ai	m and Objectives	7
1.3 O	rganization of this Thesis	8
Chapter 2	Literature Review	10
2.1 O	verview of Absorption Thermal Energy Storage	10
2.1.1	Working fluids in absorption TES	10
2.1.2	Absorption cycles	12
2.1.3	Configuration of absorption TES systems	15
2.2 Ex	xperimental Investigations on Absorption Thermal Energy Storage	18
2.3 In	tegration of absorption TES with energy systems	21
Chapter 3	Methodology and Experimental Facilities	25
	verview of the Instruments for Working Fluids' Preparation and Prement	_
3.1.1	Working fluid preparation instruments	25
3.1.2	Description of measurement instruments	25
3.2 O	verview of the Absorption Thermal Energy Storage Test Rig	29
3.3 De	escription of Components in the Test Rig	30
3.3.1	Falling film plate heat exchangers with narrow and wide channels	
3.3.2	Storage tanks, thermostatic baths, electric heaters and chiller	33
3.3.3	Measurement system and control cabinet	
3.4 M	odeling of Absorption Thermal Energy Storage System	35
3 4 1	Modeling of absorption thermal energy storage system	35

3.4	.2 Performance evaluation of absorption thermal energy storage	40
Chapter Storage	• • •	
4.1	Analysis of Three-phase Absorption Thermal Energy Storage Cycle	42
4.2	.1 Crystallization fundamentals	42
4.2	.2 Modeling of absorption TES cycle	43
4.2	Working Fluids for Three-Phase Absorption TES	50
4.2	.1 Selection of working fluids and additives	50
4.2	.2 Thermal and physical properties of the working fluids	53
4.2	.3 Energy storage density of the working fluids	60
4.3	Summary	61
Chapter	Modeling and Experimental Studies on Two-phase Absorption TES	63
5.1	Description of Two-Phase Absorption TES Processes	63
5.2	Experimental Conditions and Operations	64
5.3	Dynamic Charging Characteristics	66
5.3	.1 Influence of charging temperature	66
5.3	5.3.2 Influence of additive	
5.4	Dynamic Discharging Characteristics	71
5.4	.1 Influence of evaporation temperature	71
5.4	.2 Influence of additive	75
5.5	Energy Storage Performance Analysis	78
5.6	Key Factors Influencing Charging and Discharging Processes	81
<b>5.7</b>	Summary	83
Chapter	Experimental Studies and Dynamic Modeling on Three-phase Absorption 85	on TES .
6.1	Description of the Three-Phase Process	85
6.2	Dynamic Charging and Discharging Characteristics	87
6.2	.1 Dynamic charging characteristics under different charging temperatures	87
6.2	.2 Dynamic discharging characteristics under different evaporation temperatures	89
6.2	.3 Model validation and performance mapping	93
6.3	Performance Evaluation of Three-phase Absorption TES	95
6.3	.1 Charging performance	95
6.3	.2 Discharging performance	97
6.4	Summary	98

Chapter 7	Enhanced load following strategy for capacity design and operational	l control of
absorption th	nermal energy storage in distributed energy systems	99
7.1 Des	scription of the proposed distributed energy systems (DES)	99
7.2 Op	timal design and operational control of absorption TES in DES	101
7.3 Res	sults and discussions	104
7.4 Sur	nmary	107
Chapter 8	Conclusions and Recommendations	109
Appendix	113	
References	130	

# LIST OF FIGURES

Figure 1.1 Classification, typical materials and working principles of TES technologies2
Figure 2.1 Absorption thermal energy storage cycle diagram
Figure 2.2 Advantages and disadvantages of the open and closed sorption TES systems16
Figure 3.1 Schematic of vapor pressure measurement apparatus
Figure 3.2 Schematic of absorption TES test rig
Figure 3.3 (a) Photograph of the test rig (b) 3-D drawing of the test rig30
Figure 3.4 Structure of absorber/generator
Figure 3.5 Structure of liquid distributor
Figure 4.1 Schematic diagram of the state of LiCl solution near the crystallization line42
Figure 4.2 Schematic of the working principle of absorption TES: charging and discharging
process
Figure 4.3 Pressure-temperature-concentration (p-T-x) diagram of LiCl absorption TES cycle
45
Figure 4.4 Procedure of novel working fluid preparation and thermal and physical properties
measurement
Figure 4.5 Crystallization temperature of LiCl/H <sub>2</sub> O-EG solution with a different mass fraction
of EG53
Figure 4.6 ESD of LiCl solution containing a different mass ratio of EG54
Figure 4.7 Suspension of crystals in 53% LiCl/H <sub>2</sub> O-EG-SNPs, where LiCl solution: EG:
$SiO_2=50$ : x: y (by weight), from left to right: x=9.75, y=0.25; x=9.5, y=0.5; x=9.25, y=0.75;
x=9, y=1; x=8.75, y=1.25; x=8.5, y=1.5
Figure 4.8 Crystal size of LiCl/H <sub>2</sub> O-EG-SNPs, where LiCl solution: EG: SiO <sub>2</sub> =50: x: y (by
weight). (a) $x=0,y=0$ ; (b) $x=10,y=0$ ; (c) $x=9.25, y=0.75$ ; (d) $x=8.5, y=1.5$

Figure 4.9 Vapor pressure of LiCl/H <sub>2</sub> O-EG, LiCl/H <sub>2</sub> O-EG-SNPs and saturated LiCl solution
at different temperatures57
Figure 4.10 Viscosity of LiCl/H <sub>2</sub> O-EG and LiCl/H <sub>2</sub> O-EG-SNPs at different temperatures: (a)
LiCl/H <sub>2</sub> O-EG, (b) LiCl/H <sub>2</sub> O-EG-SNPs59
Figure 5.1 Temperature, concentration and charging rate variation of LiCl solution in the
charging process (a), (b) 85°C charging; (c), (d) 75°C charging; (e), (f) 65°C charging68
Figure 5.2 Temperature, concentration and charging rate variation of LiCl solution + EG (mass
ratio 100:2.5) in charging process (a), (b) 85°C charging; (c), (d) 75°C charging; (e), (f) 65°C
charging70
Figure 5.3 Temperature, concentration and charging rate variation of LiCl solution + EG (mass
ratio 100:5) in charging process (a), (b) 85°C charging; (c), (d) 75°C charging; (e), (f) 65°C
charging71
Figure 5.4 Temperature, concentration and charging rate variation of LiCl in discharging
process (a), (b) 50°C heating; (c), (d) combined 40°C heating and 20°C cooling; (e), (f) 10°C
cooling74
Figure 5.5 Temperature, concentration and charging rate variation of LiCl with EG (mass ratio
= 100:2.5) in discharging process (a), (b) 50°C heating; (c), (d) combined 40°C heating and
20°C cooling; (e), (f) 10°C cooling
Figure 5.6 Temperature, concentration and charging rate variation of LiCl with EG (mass ratio
= 100:5) in discharging process (a), (b) 50°C heating; (c), (d) combined 40°C heating and 20°C
cooling; (e), (f) 10°C cooling
Figure 5.7 Heat balance analysis of charging and discharging experiments78
Figure 6.1 Operating principles of closed three-phase absorption TES system, (a) charging
process; (b) storage process; (c) discharging process
Figure 6.2 p-T-x phase diagram of closed three-phase absorption TES cycle

Figure 6.3 Schematic of solution storage tank and mechanical filter
Figure 6.4 Dynamic charging characteristics of closed three-phase absorption TES at different
charging temperatures. (a), (b) Charging at 85°C; (c), (d) Charging at 75°C89
Figure 6.5 Dynamic discharging characteristics of closed three-phase absorption TES system
for different application scenarios: (a), (b) Discharging for heating scenario; (c), (d)
Discharging for combined heating and cooling scenario; (e), (f) Discharging for cooling
scenario92
Figure 6.6 Validation of the closed three-phase absorption TES model (a), (b) Temperature and
concentration variations in the charging process; (c), (d), (e) Temperature and concentration
variations in the discharging process
Figure 6.7 Comparison of the ESD of three-phase and two-phase absorption TES95
Figure 6.8 Impact of concentration difference on the charging heat96
Figure 6.9 Impact of concentration difference on ESD
Figure 7.1 Schematic of distributed energy system
Figure 7.2 Load patterns of DES in July
Figure 7.3 Framework of capacity design and optimal control
Figure 7.4 Variations of key parameters of DES integrated with absorption TES106
Figure 7.5 Impact of recovery ratio on solution mass and energy saving

# LIST OF TABLES

Table 1.1 Summary of typical crystallization inhibitors and their effects on LiBr crystallization control
Table 3.1 Validation of crystallization temperature measurement apparatus26
Table 3.2 Validation of DSC measurement
Table 3.3 Validation of vapor pressure measurement apparatus
Table 3.4 Design parameters of the heat exchangers
Table 3.5 Specifications of measurement instruments
Table 4.1 Reference working conditions for ESD calculation
Table 4.2 Effect of EG and PG on LiCl's solubility in water
Table 4.3 Correlation parameters in August Equation for three solutions at different temperatures
Table 4.4 Density of LiCl/H <sub>2</sub> O-EG and LiCl/H <sub>2</sub> O-EG-SNPs
Table 4.5 Volumetric ESD absorption TES using conventional and modified solutions58
Table 4.6 ESD comparison of absorption TES using conventional and modified solutions61
Table 5.1 Experimental conditions of the charging and discharging experiments64
Table 5.2 Summary of the charging process
Table 5.3 Summary of the discharging process
Table 6.1 Summary of the charging and discharging process
Table 7.1 Specifications of the major heating and cooling components

# **Chapter 1** Introduction

#### 1.1 Motivation

The integration of renewable energy sources with energy systems has become an inevitable trend in the face of the growing demand for sustainable development. Solar energy, being the most abundant renewable energy source on earth, presents substantial opportunities. Additionally, a considerable portion of primary energy (around 63%) is ultimately converted and emitted as low-grade waste heat at temperatures below 100°C (Forman et al., 2016). Thermal energy storage (TES) is considered a promising solution for harnessing rich solar heat and recovering low-grade waste heat. Furthermore, the inherent intermittency of the solar and waste heat, coupled with the temporal mismatch between their supply and demand, highlights the potential of TES.

Various types of TES are technically available nowadays, including sensible TES, latent TES, and sorption TES. The classification, typical materials and working principles are shown in Figure 1.1. Sensible TES relies on the specific heat of the storage materials, which has a relatively lower energy storage density (ESD). Latent TES technologies utilize the phase change enthalpy of the storage materials, thus offering a higher ESD compared with sensible TES. However, the low thermal conductivity of latent TES impacts the charging and discharging rates. Besides, both sensible and latent TES suffer from heat loss, preventing their applications in long-term or mobilized TES. In comparison, sorption TES is based on reversible sorption reactions, with a strong binding force between sorbent and sorbate that leads to a high ESD. The separate storage of sorbent and sorbate allows the sorption TES to be used for long-term or mobilized storage with negligible heat loss (Zhang and Wang, 2020). Sorption TES can be further categorized into chemisorption TES, solid-gas adsorption, and liquid-gas absorption based on the reaction types. Although chemisorption TES offers the highest ESD,

it demands the highest charging temperature (above 200°C) (N'Tsoukpoe et al., 2009), which is not suitable for harnessing solar heat. In contrast, solid-gas adsorption and liquid-gas absorption operate at lower charging temperatures, with absorption TES demonstrating better heat and mass transfer performance (Ding et al., 2024), along with higher energy storage efficiency (ESE) and ESD. Meanwhile, absorption technologies are commercially available in markets, including absorption chillers (Zang et al., 2023), absorption refrigeration systems (Hu et al., 2023), and desiccant technologies (Zhou et al., 2023), etc. Absorption cooling systems account for 86% of the sorption cooling technologies, making their integration with absorption TES easier (Ibrahim et al., 2018). Therefore, this research concentrates on the absorption TES system.

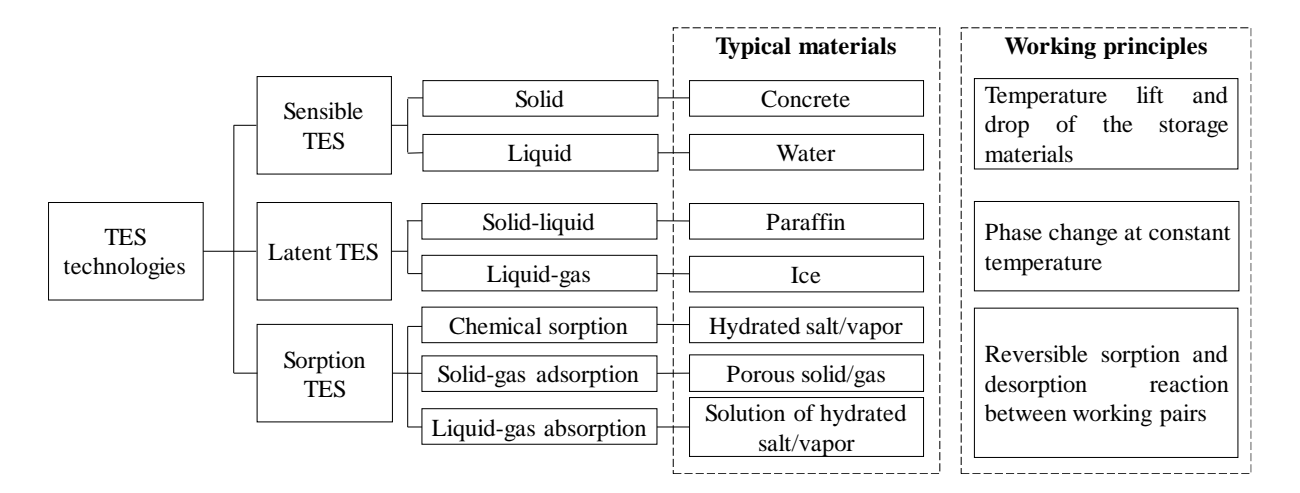


Figure 1.1 Classification, typical materials and working principles of TES technologies

Energy storage density (ESD) is a commonly used index in evaluating the storage capability of energy storage systems, which can be measured by energy stored per unit mass of material or per unit volume. The ESD of sensible heat storage is determined by the material's specific heat capacity and working temperature difference ΔT, while the ESD of latent heat storage depends on the materials' latent heat of fusion or vaporization. Absorption TES usually has a higher ESD and negligible heat loss compared with sensible and latent heat storage. For absorption TES using LiCl, the ESD is typically about 900 kJ·(kg salt)<sup>-1</sup> or 380 kJ·(kg solution)<sup>-1</sup>

when the concentration range is 42-49%. If crystallization is allowed, the ESD of the LiCl solution is 3150 kJ·(kg salt)⁻¹ or 1330 kJ·(kg solution)⁻¹ at the discharging temperature of 35°C (Yu et al., 2014). Crystals generate because the solution concentration exceeds solubility during charging, or the temperature of the concentrated solution drops below the crystallization temperature during the storage process. Absorption TES with crystallization is usually called "three-phase absorption TES".

A few studies have been carried out on determining the ESD of absorption TES and threephase absorption TES, mainly relying on theoretical analysis. Liu et al. (2011) compared the performance of seven working pairs used in seasonal TES. The ESD of absorption TES without crystallization and three-phase absorption TES with a crystallization ratio of 80% are 4387 kJ·(kg salt)<sup>-1</sup> and 5133 kJ·(kg salt)<sup>-1</sup> respectively, which are the highest among the 7 working pairs. However, the discharging temperature in their study was only 25°C, which cannot meet the requirements in most practical applications. The theoretical ESD of three-phase absorption TES using LiCl, LiBr and CaCl<sub>2</sub> as sorbents were calculated by Yu et al. (2014). LiCl solution has the highest ESD in both absorption TES and three-phase absorption TES. Its theoretical ESD of three-phase absorption TES exceeds 4000 kJ·(kg salt)<sup>-1</sup>, which is nearly three times that of absorption TES. N'Tsoukpoe et al. (2012) established a detailed dynamic model for the LiBr absorption TES system. Similarly, they found that a crystallization ratio of 67% can triple ESD. All the above-mentioned ESD values were obtained through thermodynamic analysis based on the known properties of the solutions. There were very few experimental studies quantifying the ESD of three-phase absorption TES considering the difficulty of completing a realistic discharge process in experiments.

Despite higher ESD, crystals in three-phase absorption TES bring practical problems in system configurations and real operations. The low dissolution kinetic of salt crystals restrains

the energy discharge rate. In addition, precipitated crystals may block pipes and pumps (Zhang et al., 2014). N'Tsoukpoe et al. (2013) experimentally investigated the charging and discharging characteristics of a LiBr three-phase absorption TES device. In their experiments, crystals sank and accumulated in the storage tank, resulting in a slow dissolution rate of crystals and a low discharging rate for the device. The company ClimateWell developed a prototype of three-phase absorption TES device using the LiCl solution (Bales and Nordlander, 2005). LiCl monohydrate crystals accumulated in their storage tank and blocked the pipes. Le Pierrés et al. (2017) used the KCOOH solution as the working fluid for absorption heat storage. The growth and dissolution of crystals were observed in the charging and discharging processes. However, the discharging temperature was too low for domestic hot water supply. Wang et al. (2020) designed a three-phase absorption thermal battery using LiCl hydrate salt. The ESD value was 903 kJ·(kg solution)<sup>-1</sup>. Crystallization was induced through active cooling, and dissolution was achieved by mixing the crystallized solution with a weak solution. These processes are different from the typical vapor absorption method and are more applicable to liquid desiccant dehumidification. Blockage by crystals was not concerned since the crystallization and dissolution processes occurred in the same vessel.

There are two possible ways to overcome the problems caused by crystals in the three-phase absorption TES while achieving high ESD, both relying on modification of the properties of the solution using additives. The first is to inhibit solution crystallization at high concentrations and low temperatures. The second is to allow only fine and suspended crystals to grow in the solution, and the solution eventually becomes crystal slurry, which has good fluidity. Two types of additives studied in the literature corresponded are crystallization inhibitors and nucleating agents.

As the LiBr solution is widely used in absorption machines, a lot of studies have been conducted on modifying its properties for crystallization control. Wang et al. (2011) summarized crystallization control technologies for the LiBr solution and provided guidelines for selecting additives to inhibit crystallization. Typical crystallization inhibitors include organic compounds, inorganic salts and ionic liquids, their effects on solution properties are summarized by Wang et al. (2011). For nucleating agents, very few existing studies aimed at adding nucleating agents for crystallization control. Itaya et al. (2012) proposed a modified LiBr solution by dispersing zeolite powder into it. Zeolite assisted the formation and suspension of LiBr fine crystals. Moreover, the LiBr fine crystal slurry maintained good fluidity.

Table 1.1 Summary of typical crystallization inhibitors and their effects on LiBr crystallization control

Type	Typical materials	Effect	Ref.
Organic	Ethylene glycol (EG)	Solubility increases	(Eisa et al., 1988)
compounds	Propylene glycol (PG)	Solubility increases about 8wt%	(Yoon and Kwon,
			1999)
Inorganic	LiNO <sub>3</sub> and LiCl	Crystallization temperature	(Koo et al., 1999)
salts		decreases 30-35K; LiNO <sub>3</sub> increases	
		vapor pressure, LiCl reduces vapor	
		pressure	
	LiI and EG	Solubility increases; vapor pressure	(Kim and Lee, 2001)
		reduces	
	LiCl	Solubility increases 2~5wt%	(Arabi and Dehghani,
			2015)

Ionic	19 different ionic	Solubility increases	(Krolikowska et al.,
liquids	liquids		2018; Krolikowska
			and Hofman, 2019)

The LiCl solution is a promising working fluid for three-phase absorption TES as it has higher ESD as proved by theoretical analysis. However, suppressing the formation of bulky crystals while expanding the concentration difference of the LiCl solution to achieve higher ESD is still a fundamental challenge. The challenges mainly include:

- 1. The thermal and physical properties of LiCl solution with chemical additives are not clear. Despite its potential in expanding the concentration glide and enhancing ESD, other thermal and physical properties could also significantly impact the performance of absorption TES. For example, vapor pressure influences the mass transfer rate especially the absorption rate; both specific heat capacity and viscosity influence the heat transfer rate; while density influence the ESD. The modification of LiCl solution should consider its overall performance, which is limited in existing studies.
- 2. There is a lack of standardized design of heat exchanger for LiCl absorption TES and also system configuration for LiCl absorption TES cycle. The heat exchanger is the critical component in absorption TES and has significant impact on the heat and mass transfer. Due to improper design of the heat exchangers, most existing experimental work suffers from low discharging rate and low discharging temperature.
- 3. The performance of utilizing novel modified LiCl solution in absorption TES cycle is not clear. Expanding the concentration glide could result in more dynamic variations during charging and discharging. The ESD enhancement in real system is also not clear. Typically, for three-phase absorption TES, the crystallization and dissolution is also less studied in existing work. The dynamic characteristics of three-phase absorption remains

- unexplored. The influence of three-phase process on charging and discharging processes, as well as energy storage performance requires further study.
- 4. Apart from the standalone absorption TES, the complexities associated with its integration into larger energy systems remain largely unexplored. The dynamic characteristics of absorption TES when integrated into energy systems are not well understood. The transient behavior during charging and discharging cycles, particularly under fluctuating energy supply and demand scenarios, requires detailed investigation. Also, the overall performance of absorption TES needs to be assessed.

## 1.2 Aim and Objectives

The absorption TES is a promising technology for low-grade waste heat recovery and storage. LiCl/H<sub>2</sub>O has been proved to own the highest ESD among commonly used working fluids through thermodynamic analysis. The ESD is mainly associated with the concentration glide of LiCl/H<sub>2</sub>O. To fully exploit the high ESD potential, the crystallization risks at high concentration need to be addressed. Meanwhile, the performance at real system should be experimentally studied. The aim of this research is to fully exploit the ESD and study the performance of absorption TES system using LiCl/H<sub>2</sub>O as working fluids using both experimental study and numerical study. To sum up, the research objectives based on the aim are summarized as follows:

- Modify the LiCl/H<sub>2</sub>O solution for better use in large concentration glide. Select proper chemical additives to help address the crystallization problem at high concentration. Meanwhile, study other important thermal and physical properties of the modified LiCl/H<sub>2</sub>O solution. Analyze the ESD of modified LiCl/H<sub>2</sub>O solution.
- Conduct experimental study on dynamic characteristics and performance of absorption
   TES system under different experimental conditions. Design and utilize novel heat

- exchangers for better heat and mass transfer performance. Study the impact of operation conditions on the performance of absorption TES system.
- 3. Study the dynamic characteristics and performance of three-phase absorption TES system. Establish a mathematical model for three-phase absorption TES system. Study the relationship between concentration glide and ESD. Study the performance of closed absorption TES under full-range working conditions based on the model.
- 4. Develop a framework for integrating the absorption TES into distributed energy system (DES). Designing optimal capacity and operational control strategies that account for the dynamic characteristics of absorption TES. Evaluate the performance of the integrated system.

## 1.3 Organization of this Thesis

This thesis is organized into seven chapters as below:

Chapter 1 presents the aim and the objectives of this research, and the organization of this thesis. The three-phase absorption TES is introduced. The main research gaps are summarized based on the inadequacies of the current research.

Chapter 2 presents a comprehensive literature review on absorption TES. Existing research on the working fluids, absorption cycle, absorption systems, thermodynamic modeling and experimental studies are summarized.

Chapter 3 presents the experimental facilities established for absorption TES. The facilities for novel working fluids preparation and thermal and physical properties analysis are introduced. For the established experimental test rig, the main components, measurement system, the configuration and the operation of the test rig are briefly described.

Chapter 4 presents the study on novel working fluids for enhancing ESD. The principle of crystallization and three-phase absorption TES is introduced. The selection methods of additives, preparation of working fluids, thermal and physical properties of the modified working fluids are presented. The energy performance of the modified working fluids is investigated.

Chapter 5 presents the experimental study on dynamic characteristics and performance of absorption TES using novel modified working fluids. The impact of the mass fraction of EG and working conditions are revealed experimentally. The ESD results from experiments are compared with the theoretical values.

Chapter 6 presents the experimental study on dynamic characteristics and energy performance of three-phase absorption TES. The performance under different operation conditions is also experimentally investigated. A model is established for absorption TES and validated using experimental data. The performance under all working conditions is then simulated by the model.

Chapter 7 presents the a distributed energy system integrated with absorption TES. An enhanced load following strategy for the capacity design and operational control is proposed. The enhanced load following strategy considers both the mismatch between supply and demand, and the state of solution. The performance of the integrated system at a typical month is studied.

Chapter 8 summarizes the work reported in the thesis. The main conclusions are drawn in this chapter. Also, recommendations are provided for future research and applications.

# **Chapter 2** Literature Review

## 2.1 Overview of Absorption Thermal Energy Storage

#### 2.1.1 Working fluids in absorption TES

Two types of working fluids are most widely used in the absorption systems, namely the ammonia-based working fluids (e.g. ammonia/H<sub>2</sub>O) and water-based working fluids (e.g. LiBr/H<sub>2</sub>O, LiCl/H<sub>2</sub>O). The ammonia-based working fluids are more commonly used in low-temperature environment, since ammonia as a refrigerant has lower boiling point (Jin et al., 2023). The water-based working fluids are more commonly used in low-temperature waste heat recovery. The boiling point of water can be adjusted by varying the system's vacuum degree, making it a proper candidate in waste heat recovery. Among all the commonly used water-based working fluids, LiCl/H<sub>2</sub>O have been proved to have the highest ESD as well as high energy storage efficiency (Yu et al., 2014).

For LiCl/H<sub>2</sub>O in the absorption chillers and absorption heat pumps, the concentration is typically 35~45% and while the working concentration difference is generally lower than 6%. Once the concentration exceeds the solubility or the ambient temperature drops below the crystallization temperature, the absorption system suffers from crystallization risks. Therefore, in their real operations, both the working concentration range and the working temperature require strict control to avoid crystallization.

There are two possible ways to overcome the crystallization risks, both relying on using additives to modify the properties of the solution. The first is to inhibit crystallization at high concentrations and low temperatures. The second is to allow only fine and suspended crystals to grow in the solution. The solution eventually becomes crystal slurries with good fluidity. Two types of additives corresponding to these two possible ways are available in the literature, i.e. crystallization inhibitors and nucleating agents.

Wang et al. (2011) summarized some commonly used crystallization inhibitors for the LiBr solution, including organic compounds, inorganic salts and ionic liquids. Organic compounds, like ethylene glycol (EG) (Eisa et al., 1988) and propylene glycol (PG) (Park et al., 1997), can reduce the crystallization temperature of LiBr/H2O. Biermann (1982) developed a novel mixed fluid called "Carrol" for absorption devices to inhibit crystallization. The mass ratio of LiBr and ethylene glycol in "Carrol" was 4.5:1. Thermodynamic properties of Carrol such as pressure-concentration-temperature equilibrium, crystallization curve, density and viscosity were also measured (Biermann and Riemann, 1979). Since then, "Carrol" was widely adopted in various absorption devices including absorption chillers (Biermann and Reimann, 1982) and absorption heat pumps (Santoyo et al., 1999). Yoon and Kwon (1999) compared the crystallization temperature of LiBr solution with and without propylene glycol. The authors found that propylene glycol can increase the crystallization concentration limit by 8% at a constant vapor pressure. Despite the enhancement of solubility, the concentration of a solution with crystallization inhibitors should still be kept below the enhanced solubility to prevent crystallization. There are very few studies on adding nucleating agents to modify solutions, but in the existing literature, they exhibited good potential for crystallization control. Itaya et al. (2012) proposed a modified LiBr solution by dispersing zeolite powder into it. Zeolite assisted the formation and suspension of LiBr fine crystals. Moreover, the LiBr fine crystal slurries maintained good fluidity. However, nucleating agents cannot increase the solubility of salts. Whether the combination the crystallization inhibitors and nucleating agents can take advantage of both additives remains further investigation.

Apart from the ammonia-based and water-based working fluids, ionic liquids and eutectic solvents have emerged as promising candidates for absorption TES systems. Ionic liquids, known for their negligible vapor pressure and excellent thermal stability, offer a wide range of operating temperatures and the potential to avoid issues like crystallization. Besides, ionic

liquids are non-corrosive, which ensure the safety and cycle stability. The study on the use of ionic liquids in absorption systems mainly focus on their thermal and physical properties (Wu et al., 2020), and performance as alternative working fluids (Wu et al., 2019; Wu et al., 2021; Gao and Xu, 2023). Eutectic solvents, formed by mixing two or more substances to achieve a lower melting point than any of the individual components, can also provide a low vapor pressure. The performance of absorption TES utilizing eutectic solvents are studied by Sui et al. (2023).

## 2.1.2 Absorption cycles

An absorption TES cycle usually includes three processes, namely the charging process, storage process and discharging process. Figure 2.1 shows the three processes in the solution's pressure-temperature-concentration diagram. The red solid lines 1-2-3, 3-4, 4-5-1, represent the charging process, storage process, and discharging process, respectively. In the charging process, the weak solution is heated up by an external heat source. The solution temperature rise follows the iso-concentration line 1-2, and the vapor pressure increases until reaching the condensation pressure (i.e. point 2). After that, the vapor starts to desorb from the solution and the solution concentration rises, this process follows the isobaric line 2-3. After reaching an equilibrium at point 3, the charging process ends.

For the storage process, the solution is isolated from the environment, therefore the concentration stays the same. The temperature gradually drops to ambient, following the isoconcentration line 3-4.

For the discharging process, the vapor evaporates at its evaporation pressure ( $p_{eva}$ ). The rich solution at ambient temperature (point 4) absorbs vapor, the solution temperature increases, following the line 4-5. When the solution pressure equals  $p_{eva}$ , the solution temperature needs

to drop gradually along the line 5-1 to continue the discharging process. During this process, the solution gradually becomes diluted until reaching the discharging temperature.

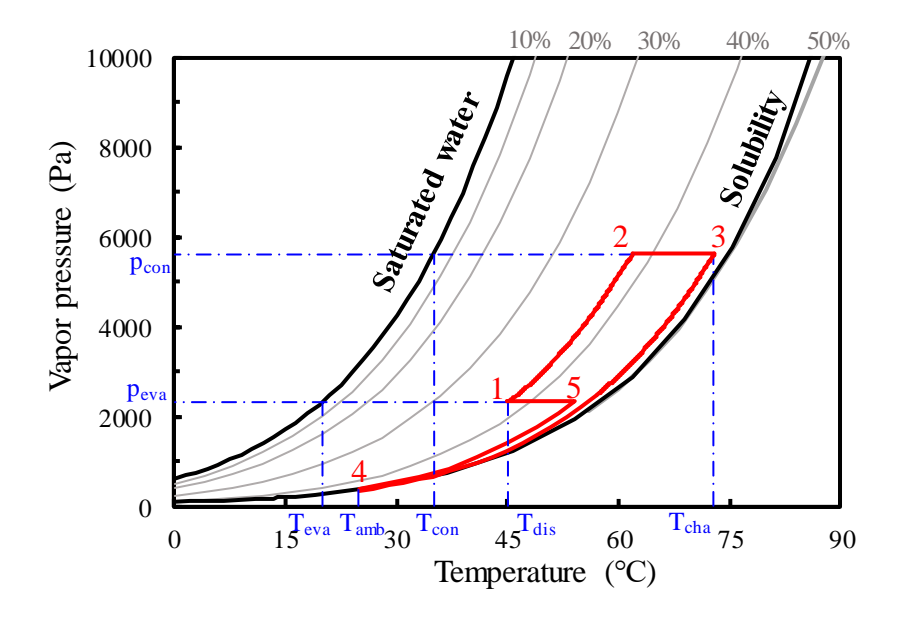


Figure 2.1 Absorption thermal energy storage cycle diagram

It can be seen from Figure 2.1 that the charging, storage and discharging processes are determined by the operating temperature conditions, including the charging temperature, condensation temperature, evaporation temperature, discharging temperature and ambient temperature. The solution enthalpy is determined by solution temperature and concentration. Therefore, once the operating temperature conditions and initial concentration is determined, the thermodynamic analysis can be conducted based on the absorption TES cycle.

For three-phase absorption TES cycle, the main difference is that three-phase absorption cycle functions at a larger concentration glide, where crystallization happens when the solution concentration exceeds the solubility during charging or storage processes. During the discharging process, the crystals dissolve with the dilution of solutions. Compared with the conventional absorption cycle, the three-phase absorption cycle owns higher ESD due to a larger concentration glide.

Thermodynamic analysis is an effective and simple way to analyze the ESD and overall performance of absorption cycles using different working fluids. Liu et al. (2011) compared the ESD and efficiency of seven working pairs using thermodynamic analysis. Both the ESD of two-phase and three-phase absorption TES with a crystallization ratio of 80% were investigated. The highest ESD values were obtained using LiCl as working fluids, which were 4387 kJ·(kg salt)<sup>-1</sup> and 5133 kJ·(kg salt)<sup>-1</sup>, respectively. The corresponding concentration glides were 30-44.3% and 30-52.1% with an efficiency of 95% and 92.3%, respectively. The ESD value of three-phase absorption cycle was the highest mentioned in the literature, which provided a baseline for future studies. Yu et al. (2014) also confirmed that LiCl solution has the highest ESD in both absorption TES and three-phase absorption TES. The ESD values were also studied using thermodynamic approach. The highest ESD, a value greater than 4000 kJ·(kg salt)<sup>-1</sup>, was achieved at three-phase sorption, in which the LiCl solution turns into LiCl hydrated salts after desorption. N'Tsoukpoe et al. (2012) established a detailed dynamic model based on thermodynamic cycle of the LiBr absorption TES system. They also found that three-phase process can significantly enhance the ESD.

The above-mentioned two-phase and three-phase cycles are all closed single-stage close cycles, in which the high ESD is realized by large concentration glide or three-phase process. However, in real applications, crystallizations in three-phase process may cause blockage and damage the system. Therefore, three-phase absorption cycle is only analyzed using the thermodynamic approach. To overcome the limitations of single-stage cycles and expand the application of absorption TES, some researchers proposed advanced absorption TES cycles. For instance, the double-effect cycle can utilize higher charging temperatures with significant enhancement in COP (Ding et al., 2020). Double-stage cycle can significantly increase the temperature lift and ESD (Xu, et al., 2018). Integrating the absorption TES system with a cooling subsystem can obtain an absorption TES cycle with a large concentration glide, which

can obtain high ESD at lower evaporation temperature (Xu, et al., 2017). Compression-assisted cycle can significantly enhance the ESD, charging rate, and discharging rate (Ding, et al., 2020).

## 2.1.3 Configuration of absorption TES systems

Based on the configuration, the absorption TES systems can be categorized into open and closed systems. The open systems operate under atmospheric pressure, utilizing humid air as the sorbate. Therefore, it is easy to construct. However, the performance of the open systems is constraint by the atmospheric conditions. The closed systems function under vacuum conditions, employing water vapor as sorbate (Mehari et al., 2020). The closed systems can produce both heating and cooling by harnessing the heat produced by vapor absorption and cooling energy produced by water evaporation, respectively. The detailed comparison between open and closed absorption TES systems are summarized and compared in Figure 2.2 (ElBahloul AA et al., 2022). The performance of open and closed absorption TES has been studied via thermodynamic analysis of the absorption TES cycles and experimental investigations.

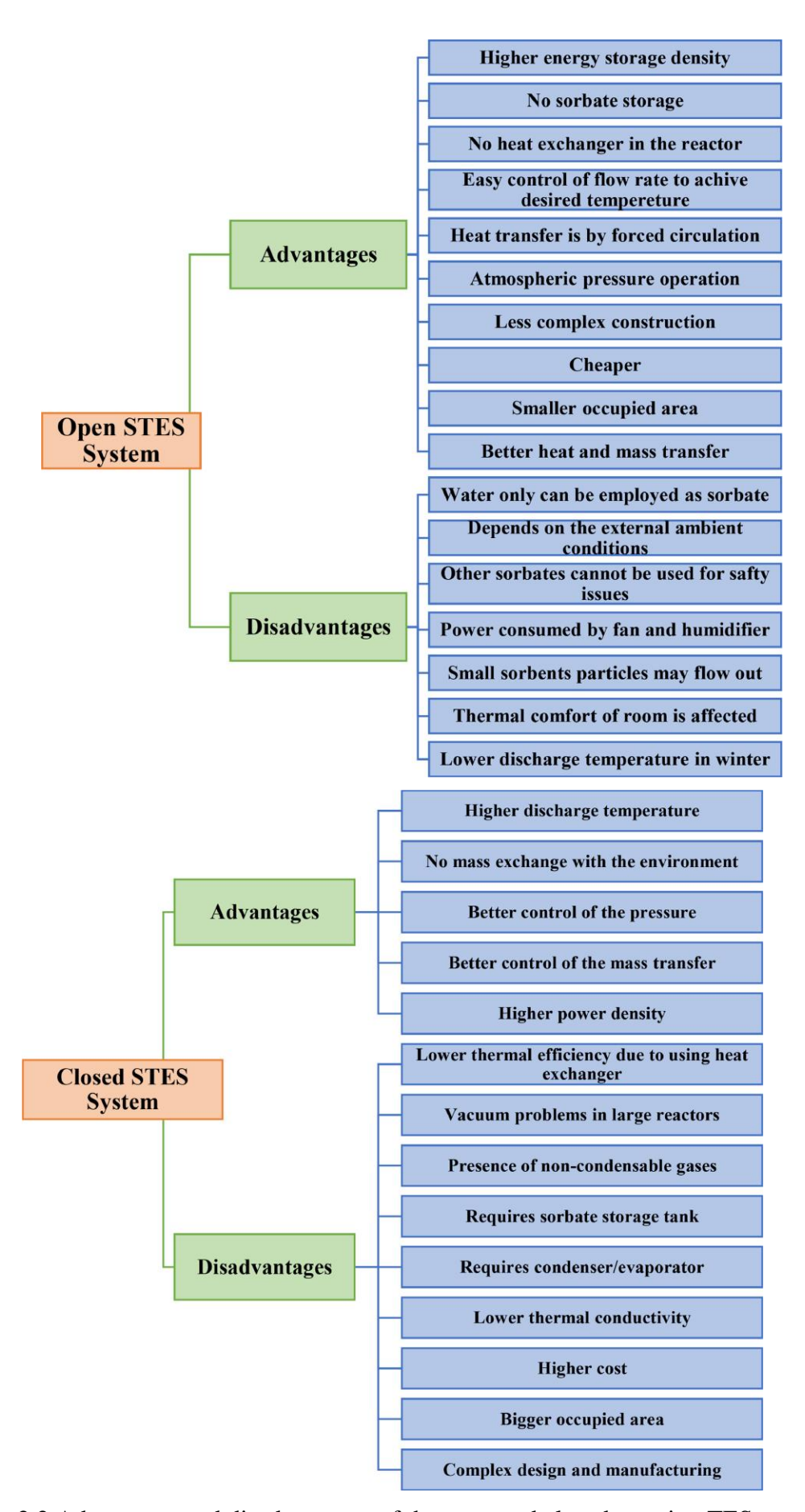


Figure 2.2 Advantages and disadvantages of the open and closed sorption TES systems

For the open system, Mehari et al. (2022) examined the thermodynamic processes and energy storage performance of a three-phase absorption thermal energy cycle using different working pairs, such as LiCl/H<sub>2</sub>O, LiBr/H<sub>2</sub>O and CaCl<sub>2</sub>/H<sub>2</sub>O. The LiCl/H<sub>2</sub>O working pair demonstrated ideal performance, requiring the lowest charging temperature and humidity levels for complete dehydration, achieving a maximum ESD exceeding 600 kWh/m<sup>3</sup>. The ESD was 2.0 and 3.3 times higher than that of the closed cycle and conventional open cycle, respectively. Subsequently, the same authors (2022) performed experimental studies based on the open three-phase sorption cycle. LiCl/H<sub>2</sub>O was used as the working pair to study the dynamic characteristics and ESD of the open system. The maximum ESD potential derived from experimental results is only 12.3% lower than the theoretical value predicted by the thermodynamic analysis. At a charging temperature of 75°C and a relative humidity of 85%, the ESD achieved was 333 kWh/m<sup>3</sup> with a temperature lift of 5-14 °C and the heat storage efficiency was 35.6%. The author then proposed a novel cycle that integrates the open threephase absorption TES system with an evaporative cooler for cooling and dehumidification (2022). A simultaneous large enhancement in ESD and COP was achieved by the proposed system. With the assist of evaporative cooler, the ESD and the COP reached 563 kWh/m<sup>3</sup> and 1.22, respectively under typical summer operating conditions. Wang et al. (2020) established an open three-phase absorption TES experimental platform using LiCl solution. The threephase absorption TES device was integrated with a dehumidifier and an evaporative cooler. The crystals in the three-phase solution dissolved very fast during the discharging process. With a crystallization ratio of 34.4%, the proposed system demonstrated a high ESD of 300 kWh/m<sup>3</sup> and the discharging rate reached up to 1.3kW.

For the closed system, Liu et al. (2011) investigated the ESD and ESE of a conventional closed single-stage absorption TES cycle using various working pairs. The LiCl/H<sub>2</sub>O working pair outperformed six other working pairs in both ESD and ESE. The LiCl/H<sub>2</sub>O working pair

achieved an ESD of 4387kJ/kg material. Moreover, the authors found that the ESD of absorption TES could be further enhanced by extending the concentration difference and allowing crystals in the LiCl solution. The same conclusions are also ascertained by Yu et al. (2014). This study proposed a closed three-phase absorption TES cycle and a closed three-phase sorption TES cycle, charging the solutions into crystallized salt solution and dehydrated salts, respectively. The ESD was enhanced from 126 kWh/m³ to 459 kWh/m³ by the three-phase absorption cycle and further raised to about 700 kWh/m³ by the three-phase sorption cycle.

## 2.2 Experimental Investigations on Absorption Thermal Energy Storage

Experimental analysis on closed systems has also been conducted to assess the performance of absorption TES under real working conditions. Zhang et al. (2014) investigated the charging and discharging performance of a closed absorption TES cycle using LiBr solution as the working fluid. The performance at three application scenarios was studied experimentally. The highest recorded ESD was 110 kWh/m<sup>3</sup> within domestic hot water supply scenarios. N'Tsoukpoe et al. (2013) established a closed absorption TES system using LiBr solution with partial crystallization. The charging and discharging experiments were conducted. The experimental results showed that the storage density can be enhanced by crystallization. However, both the discharging temperature and discharging rate were low due to inadequate absorber design. Therefore the ESD value was not given. The Swedish company ClimateWell (2005) company developed the first absorption TES machine based on the three-phase absorption TES cycle, with LiCl solution as working fluids. The crystallized solution was stored within the storage vessel. However, the ESD and COP results were not disclosed. Additionally, the performance of heat exchangers was not satisfactory and undesired crystal accumulation occurred in the pipes. Le Pierrès et al. (2017) established a closed absorption TES system with KCOOH solution as the working fluid, demonstrating its feasibility. However, the ESD results were not calculated, as the potential of the concentration difference was not fully realized. Apart from the single-stage cycles, experiments have also been conducted based on advanced cycles. Gao et al. (2020) established a closed absorption TES system based on the double-stage cycle using LiBr solution as working fluids. The proposed system can operate in both single-stage and double-stage modes. The concentration glides were 59%-62% for singlestage mode, and 45%-61%/46%-61% for the two solutions in double stage mode. Their respective ESD values achieved were 44 kWh/m<sup>3</sup> and 103 kWh/m<sup>3</sup>. The double-stage mode had an efficiency ranging from 25% to 31% at different evaporation temperatures. Ding et al. (2024) proposed an absorption-enhanced generation method during the charging process to expand the concentration glide at lower charging temperature and thereby increase the ESD. LiBr solution was chosen as the working fluid. An additional solution tank is utilized to further enhance the absorption process of the solution. Under a charging temperature of 70 °C, the absorption-enhanced generation expanded the concentration glide from 48.6%-55.3% to 48.6%-62.5%, reaching a fully-charged state. At this charging condition, the ESD was enhanced from 62.7 kWh/m<sup>3</sup> to 100 kWh/m<sup>3</sup>. Concerning the abovementioned experimental results, the highest ESD values achieved by absorption TES to date are around 100 kWh/m<sup>3</sup>.

Heat exchangers are the core components of absorption thermal energy storage (TES) systems, serving as generators and absorbers for the solution, and as condensers and evaporators for water. For the abovementioned experimental studies, Zhang et al. (2014) employed staggered-arrange tube bundles heat exchanger with 2.47 m² and 3.70 m² of total heat exchange areas for generator/absorber and evaporator/condenser, respectively. These heat exchangers achieved a heat exchange rate of 7kW for both charging and discharging. Gao et al. (2020) utilized a shell-and-tube heat exchanger in a double-stage absorption TES system, although detailed design parameters were not provided; nonetheless, both charging and discharging were successfully demonstrated. Ding et al. (2024) implemented a coil spray heat

exchanger in a two-stage absorption TES system with absorption-enhanced generation, achieving a maximum cooling power of 1.4 kW with a total heat exchange area of 0.24 m<sup>2</sup>. Other studies have adopted various types of heat exchangers, including shell-and-tube and falling film over vertical plate designs. These examples indicate that multiple heat exchanger configurations can be applied in absorption TES systems; however, the heat exchanger design is often underemphasized in the literature.

Falling film absorbers are the most commonly used type in commercial absorption cooling machines. Falling film systems are recommended for their ability to enhance heat and mass transfer during the absorption process. The thin film formed in this mode provides a high heat transfer coefficient and stable operation. Therefore, the adoption of falling film heat exchangers represents a promising option for absorption TES applications.

The thermodynamic analysis and experimental studies have demonstrated the ESD enhancement potential of the three-phase absorption in both open and closed absorption TES cycles. Compared to the closed systems, open systems offer advantages such as greater sorption uptake capability, ease of crystallization handling, and simpler system construction and maintenance (ElBahloul et al., 2022). However, the drawbacks of open systems are apparent, since their performance relies on atmospheric conditions, and the use of humid air as an absorbate limits their applications and results in a lower discharging temperature (Mehari et al., 2020). In contrast, the absorbate used in the closed system can achieve higher discharging temperature and greater power density. Moreover, the closed system can provide heating and cooling simultaneously since the water evaporation happens at a high vacuum degree (Fumey et al., 2019). However, existing studies on closed three-phase absorption mainly focus on the thermodynamic analysis of absorption TES cycles, including single-stage cycles and advanced cycles. Experimental studies that investigate the performance of three-phase absorption TES

under practical working conditions are limited. A comprehensive study of its dynamic characteristics can yield valuable insights to the system's charging and discharging processes, thereby facilitating its practical applications.

## 2.3 Integration of absorption TES with energy systems

Absorption TES owns high ESD, especially working at three-phase absorption cycle. Despite its ESD storage potential, the integration of absorption TES into energy systems has been less extensively studied compared to standalone applications. Previous research has primarily focused on the thermal storage function of absorption TES, with limited exploration of its integration with absorption chillers or heat pumps, which share the same working fluids.

Several studies have highlighted the benefits of integrating absorption TES with solar-powered absorption air-conditioning systems. Al-Ugla et al. (2015) proposed three alternative designs for a solar-powered absorption air-conditioning system, namely heat storage, cold storage and refrigerant storage. The integration of absorption TES can enable the continuous operation of absorption air-conditioning even when solar is insufficient or unavailable. The results show that the refrigerant storage has the best performance. Based on this, El-Shaarawi and Al-Ugla (2016) compared the four hybrid storage configurations, including heat and cold storage, heat and refrigerant storage, cold and refrigerant storage, and heat, cold and refrigerant storage. The combined cold and refrigerant storage exhibited an optimal performance with the lowest storage volume and less system complexity. Ibrahim et al. (2017) developed a solar-assisted absorption chiller integrated with absorption TES. The integration of absorption TES provides flexibility for the chiller operation, proving the feasibility of the integration. The same author also studied the performance of a double-effect absorption chiller integrated with absorption TES (2023). The performance was studied comprehensively including the ESD,

COP, cooling rate, and exergy efficiency, which further demonstrate the feasibility of the integration.

The abovementioned researches mainly consider the variations in heat sources to study the feasibility of the integrated systems. To balance the transient supply and demand, it's important to consider the variations of cooling or heating loads and the dynamic charging and discharging characteristics of absorption TES. Current modeling approaches often rely on steady-state assumptions, which overlook the transient characteristics of absorption TES during periods of fluctuating cooling demand. The slower response time of absorption TES compared to ideal TES can significantly impact the system's ability to respond to peak loads or fluctuations in demand. Therefore, optimal control strategies must account for these dynamic characteristics to effectively balance transient supply and demand.

Recent research has begun to address these challenges. Ding et al. (2023) studied transient supply-demand matching characteristics of a solar-driven absorption TES system for building space cooling. Numerical simulation was conducted in this study to investigate the annual dynamic performance of absorption TES under different climate conditions. This study proved the feasibility of using absorption TES for balancing the energy supply and demand in domestic applications. Crespo et al. (2023) optimized the control of a solar-driven sorption TES for domestic hot water supply. The optimization maximized the performance of sorption TES. Choi et al. (2024) studied the transient characteristics of sorption TES and the optimal discharging under different load patterns. The optimal operating points based on load patterns can be determined.

While existing research has demonstrated the feasibility and investigated the dynamic performance of the absorption TES in buildings, their performance in broader energy frameworks requires further investigation. Distributed energy systems (DES) are currently

considered an attractive option worldwide for their high efficiency and low carbon emission. The integration of TES with DES has shown promising energy-saving potentials (Yuan et al., 2020). The integration serves two primary objectives. Firstly, it enables the operation of the absorption chiller or heat pump during periods of insufficient or unavailable solar energy. Secondly, it balances the mismatch between the supply and demand through energy storage.

In larger energy systems with various energy sources and multiple energy demands, the operational control of TES is critical to its performance. Optimal operational control strategies are essential for maximizing the potential of TES. Commonly employed strategies include full load operation (Mago and Luck, 2013), schedule operation strategy (Zheng et al., 2017), load following strategies (Yuan et al., 2020), etc. Liu et al. (2015) proposed an hourly operational control strategy of a CCHP system with TES under variable loads. The proposed strategy achieved higher energy savings and cost reduction. Also, it can reduce the installed cooling and heating capacity. Zheng et al. (2017) proposed a strategy that can actively adjust the operation of the power generation unit based on the state of the thermal storage device, allowing for maximum heat input and output. These studies collectively demonstrate that optimal control of TES offers multifaceted benefits to energy systems, underscoring the need for further research into the integration of absorption TES with DES.

However, existing literature on the optimal control of TES predominantly employs energy conservation or energy balance models that simulate the energy flow within the system. These models often overlook the internal charging and discharging dynamics, failing to consider the state of the TES system. Furthermore, the TES technologies primarily examined in these studies are mainly sensible or latent TES, while the use of absorption TES remains underexplored due to a lack of understanding of its physical processes. Our previous study has revealed that both the charging and discharging processes of absorption TES are highly

dynamic, influenced by working conditions and the solution state (i.e., temperature and concentration). Consequently, it is crucial to analyze the performance of absorption TES under fluctuating energy supply and demand. This analysis will provide valuable insights into how absorption TES can be effectively integrated into DES, enhancing their operational efficiency and reliability.

# **Chapter 3** Methodology and Experimental Facilities

# 3.1 Overview of the Instruments for Working Fluids' Preparation and Properties Measurement

## 3.1.1 Working fluid preparation instruments

Magnetic stirrer and supersonic vibrator are used to prepare the working fluids. Magnetic stirrer is used for dissolving the LiCl salts and mixing the solutions with additives. Supersonic vibrator is used to improve the suspension of nanoparticles.

## 3.1.2 Description of measurement instruments

The thermal and physical properties of the novel working fluids have a significant impact on the performance of ATES. The measured properties including solubility, crystal size, specific heat capacity, vapor pressure, viscosity and density.

Solubility is the mass concentration of LiCl in water at a given temperature when the solution is saturated. The temperature is the crystallization temperature of the corresponding saturated solution. For a given solution with a known mass concentration, the solubility measurement is equivalent to the crystallization temperature measurement. The visual polythermal method (Inada et al., 2019) was adopted to measure the crystallization temperature of the LiCl solution with a given mass concentration of LiCl and mass ratios of EG. The equipment included a set of 500mL beakers, a set of 50mL Erlenmeyer flasks, a precision thermostatic bath with a measuring range from 268.15K to ambient temperature, and a magnetic stirrer. All the samples were carefully weighted by the precision balance with an accuracy of 0.001g. The prepared sample solutions were placed in Erlenmeyer flasks to stir and heat. The heating temperature was set above the estimated solubility line and the solutions were stirred for 2 hours to completely dissolve LiCl. Then, the undersaturated hot solution samples were cooled down slowly until crystals visibly precipitated. The samples were then preserved

in the thermostatic bath for 48 hours to ensure that they reached an equilibrium state. Then, the temperature was increased slowly (0.1K min<sup>-1</sup> approximately) to dissolve all crystals. The temperature at which the last crystal disappeared was recorded as the crystallization temperature. Each test was repeated 3 times to take the average value.

Table 3.1 shows the validation of crystallization temperature measurement. The measured crystallization temperatures of pure LiCl solution with different concentrations are compared with theoretical values. Theoretical crystallization temperature was calculated using correlations provided by Conde (2004). The crystallization temperatures are measured three times and the measured values are close to each other. The mean absolute error (MAE) was 1.47°C, which indicates the good repeatability of crystallization temperature measurement.

Table 3.1 Validation of crystallization temperature measurement apparatus

Concentration (%)	Measurement value (°C)	Theoretical value (°C)	Absolute error (°C)
51.04	64.0, 66.1, 67.0	69.3	3.6
49.14	53.1, 54.2, 55.5	55.4	1.1
48.00	46.1, 48.0, 46.2	45.9	0.9
46.80	35.5, 36.1, 36.7	35.0	1.1
45.85	23.1, 24.6, 27.7	25.7	0.6

The SNPs dispersion in EG was added into the LiCl solution to facilitate heterogeneous nucleation of LiCl crystal and therefore prevent the formation of bulky crystals. Suspension phenomenon and crystal size were used to evaluate the performance of SNPs in promoting the formation of fine crystals. The mixed solutions were prepared using the same procedure as

described in Section 3.1.1. All the prepared solutions were left to settle for 100 hours after preparation before observing the suspension and measuring the crystal size.

The enthalpy changes of novel working fluids during charging and discharging are important to determine ESD. Three groups of samples were prepared for DSC tests, including the pure LiCl solution, the LiCl solution with EG, and the LiCl solution with EG and SNPs. Each group contains samples whose concentration and mass ratio of solution to additives according to the experimental results present in Section 4.1 and 4.2. The temperature was raised from room temperature (around  $20^{\circ}$ C) to  $T_{cha}$  at a heating rate of  $10^{\circ}$ C/min. The heat flux and temperature were recorded at a constant interval of 1s. The enthalpy changes of the sample during temperature change can be calculated by the integration of the heat flux. All the tests were performed in the nitrogen environment to eliminate the impact of water vapor in the air.

Table 3.2 compares the enthalpy change from DSC measurement and the simple calculation. Solutions with a concentration of 35%, 41%, and 44% were used in the DSC measurement. The temperature was increased from 25°C to 85°C during the DSC measurement. The theoretical enthalpy value was obtained from (Chaudhari and Patil., 2002). It can be found that the enthalpy change from DSC measurement results agrees well with the theoretical value. The MAE was 5.56 kJ·(kg solution)<sup>-1</sup> and the MARD was 3.40%, indicating good accuracy of the DSC measurement.

Table 3.2 Validation of DSC measurement

Concentration Measu	arement (KJ·Kg solution ') I no	neoretical (kJ·kg solution <sup>-1</sup> )	Relative error (%)
35% 167.97	7 158	8.83	5.14
41% 145.80	0 144	4.71	0.20

44% 131.22 137.68 4.85

Vapor pressure, viscosity and density of the working fluid are important properties in studying absorption TES. The vapor pressure difference in the evaporator and absorber is the driving force of the discharging process. Viscosity is a critical parameter in heat and mass transfer. Density influences the ESD and the volume of the storage tank. The static method was used to measure vapor pressure (Wen et al., 2020). The experimental apparatus is shown in Figure 3.1. It consisted of a vacuum pump, a heating rod, measurement devices, a container and insulation material. The measurement instruments included a Platinum resistance thermometer with an accuracy of 0.35K and an absolute pressure meter with an accuracy of 0.5%. The container has an inner volume of 1.7L.

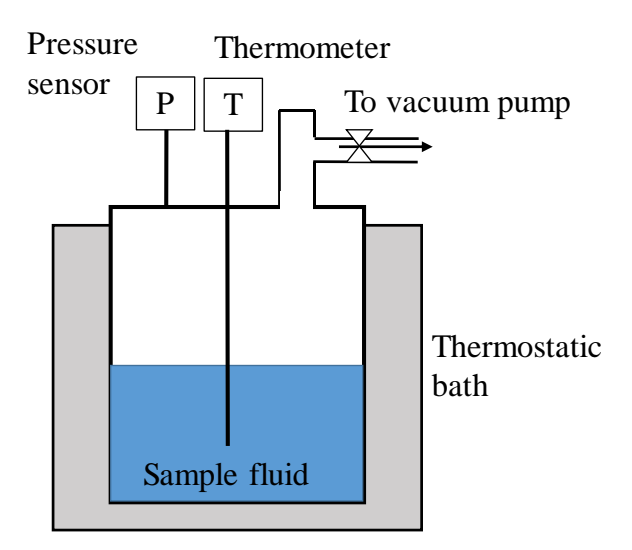


Figure 3.1 Schematic of vapor pressure measurement apparatus

At the beginning of the measurement, a 1.5L sample fluid was added into the container at 0°C. To fully degas the dissolved air, the container was evacuated for 30 seconds until the pressure value stabilized. The fluid was gradually heated to 85°C by the thermostatic bath with an increment of 5°C. The temperature and corresponding vapor pressure were recorded after reaching equilibrium. Each test was repeated three times to ensure the accuracy of measurements.

The saturated water vapor pressure was measured to examine the accuracy of the apparatus. The temperature of the water was set from 25-85°C. The theoretical saturated water vapor pressure was calculated by the Goff-Gratch equation. The comparisons between the theoretical and measured values are shown in Table 3.3. The MAE was 0.78kPa and the MARD was 3.95%, indicating the good accuracy of the apparatus.

Table 3.3 Validation of vapor pressure measurement apparatus

Temperature (°C)	25	30	35	40	45	50	55	60	65	70	75	80	85
Measurement value (kPa)	3	4	5.5	7.2	9.1	11.7	15.2	19.2	24.2	30.2	38.4	45.5	55.5
Theoretical value (kPa)	3.2	4.2	5.6	7.4	9.6	12.3	15.7	19.9	25.0	31.2	38.6	47.4	57.8
Relative error	5.3%	5.7%	2.2%	2.4%	5.1%	5.2%	3.5%	3.6%	3.3%	3.1%	0.4%	3.9%	4.0%

The solution density  $\rho$  was measured using an electronic densimeter. A 50mL sample was placed in a beaker, which was placed in a thermostatic bath to maintain temperature fluctuation within  $\pm 0.1$  °C. The density was measured within the temperature range of 25~85°C.

For viscosity measurement, the fluid type should be considered. The LiCl solution is a Newtonian fluid, where viscosity is only the function of temperature. However, the LiCl/H<sub>2</sub>O-EG and LiCl/H<sub>2</sub>O-EG-SNPs are non-Newtonian fluids. Their apparent viscosity is influenced by temperature and shear rate. The viscosity of the LiCl solution, LiCl/H<sub>2</sub>O-EG and LiCl/H<sub>2</sub>O-EG-SNPs were measured by a rotation viscosity meter with an accuracy of 0.5%.

# 3.2 Overview of the Absorption Thermal Energy Storage Test Rig

An experimental apparatus was constructed to explore the dynamic process of charging and discharging characteristics of absorption TES using innovative working fluids. The schematic of the absorption TES test rig is shown in Figure 3.2. Figure 3.3 (a) and (b) show the actual

photograph and 3-D drawing of the experimental test rig, respectively. The apparatus is composed of 5 main components: the heat exchangers, solution and water tanks, thermostatic water baths, a chiller and sensors.

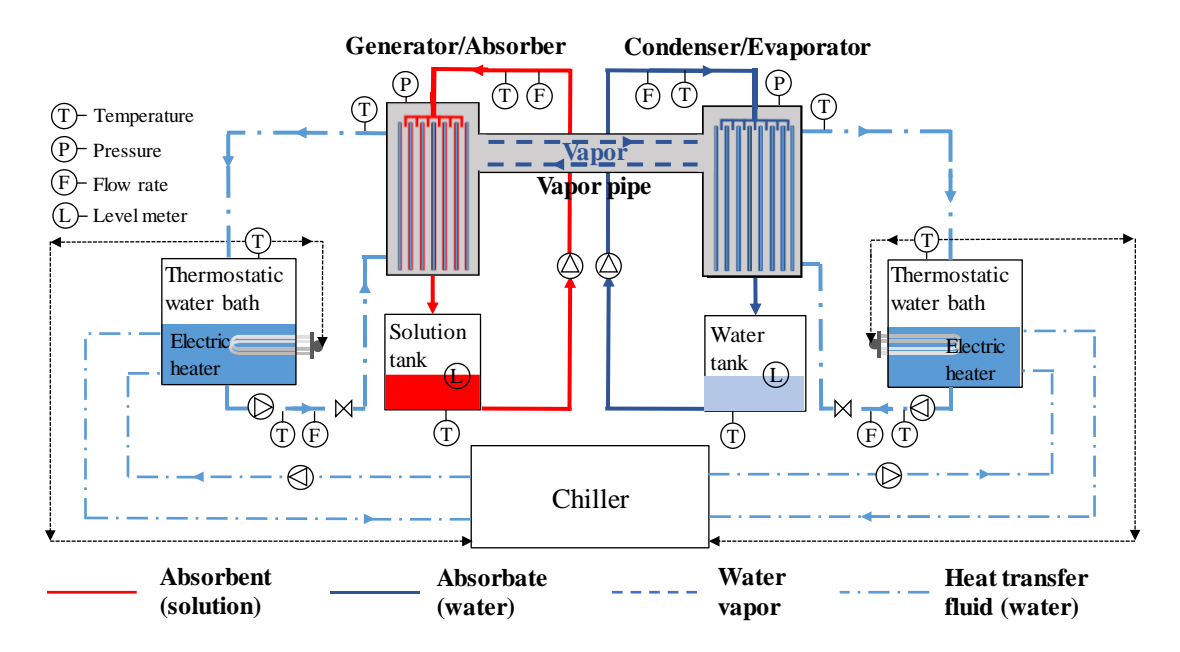


Figure 3.2 Schematic of absorption TES test rig

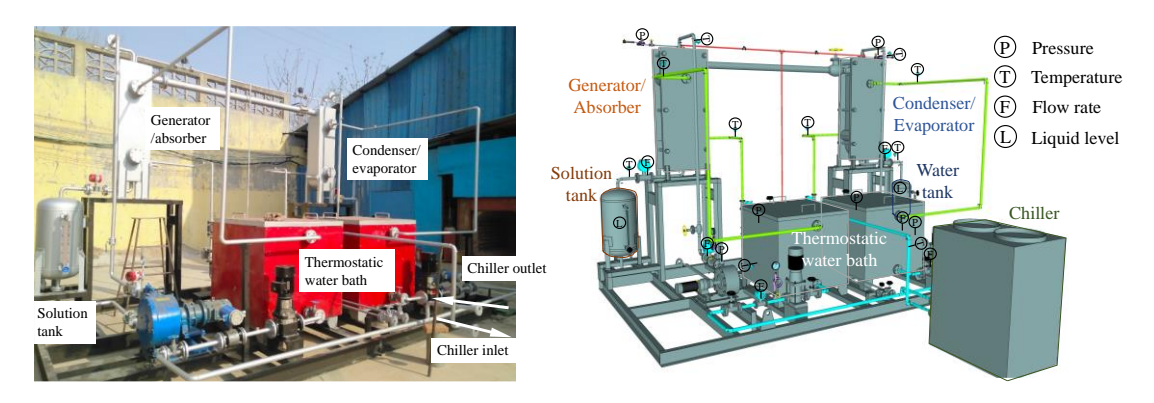


Figure 3.3 (a) Photograph of the test rig

(b) 3-D drawing of the test rig

# 3.3 Description of Components in the Test Rig

#### 3.3.1 Falling film plate heat exchangers with narrow and wide channels

Two heat exchangers are the key components of the test rig. One is referred to as the "Generator/Absorber", which is used for solution generation during the charging process and water absorption during the discharging process. The other one, known as the "Condenser/Evaporator", is used for vapor condensation during the charging process and water

evaporation during the discharging process. These two heat exchangers are interconnected by a vapor pipe, which enables the transportation of vapor from the generator to the condenser during the charging process, and conversely, from the evaporator to the absorber during the discharging process.

The heat exchangers are crucial for achieving the coupled heat and mass transfer in the absorption TES test rig. As the charging and discharging processes operate under high vacuum, even a minor pressure drop can significantly affect mass transfer. Consequently, the heat exchanger with a large heat transfer area as well as a small pressure drop is preferred. A novel plate heat exchanger with narrow and wide channels has been designed for the generator/absorber and the condenser/evaporator in the absorption TES system. The design parameters of heat exchangers are detailed in Table 3.4. The heat transfer area is determined by the heat exchange rate calculated from the designed power (i.e. 10kW desorption rate). The width of the wide channel is 30mm, providing sufficient width for the water vapor transfer with negligible pressure drop. Both generator/absorber and condenser/evaporator have the same structure, thus, the generator/absorber will be used as an example in the subsequent illustration.

Table 3.4 Design parameters of the heat exchangers

	Generator/Absorber	Condenser/Evaporator
Heat transfer area (m <sup>2</sup> )	4.1	5.0
Number of plates	7	8
Type of plates	High theta chevron	High theta chevron corrugated
	corrugated plate	plate
Materials	304 stainless steel	304 stainless steel

Channel width (mm)	30	3

Figure 3.4 presents the front and side views of the absorber/generator. It can be seen that the plate heat exchanger comprises a series of parallel plates, dividing the heat exchangers into several channels. The adjacent channels have different widths. The solution and water vapor flow in the wide channels while the heat transfer fluid (water) flows in the narrow channels. The flow pattern between the solution and water is counter flow. In the experiments, the solution enters the heat exchanger from the top (solution inlet A) and exits from the bottom (solution outlet B), while the heat transfer fluid flows from the lower inlet (inlet C) to the upper outlet (outlet D). The uniform distribution of fluids on the surface of the heat transfer plate is critical to the wetting and heat transfer of the fluids. Therefore, a liquid distributor has been tailored for the plate heat exchanger with narrow and wide channels. Each heat exchange plate has a size of 969mm×559mm. The structure of the liquid distributor is shown in Figure 3.5. The liquid distributor consists of three parts: a large vertical pipe at the top serving as the solution's inlet, several horizontal parallel pipes with slots opened on both sides at the bottom, and another horizontal pipe connecting the vertical pipe and horizontal parallel pipes. The fluids entering from the top will be evenly distributed into the parallel pipes by the horizontal pipe, then exit from the slots and spray onto the plate. The solution flows over the heat transfer plate as a falling film, which can enhance heat transfer efficiency by ensuring a large contact area between the solution and the plate.

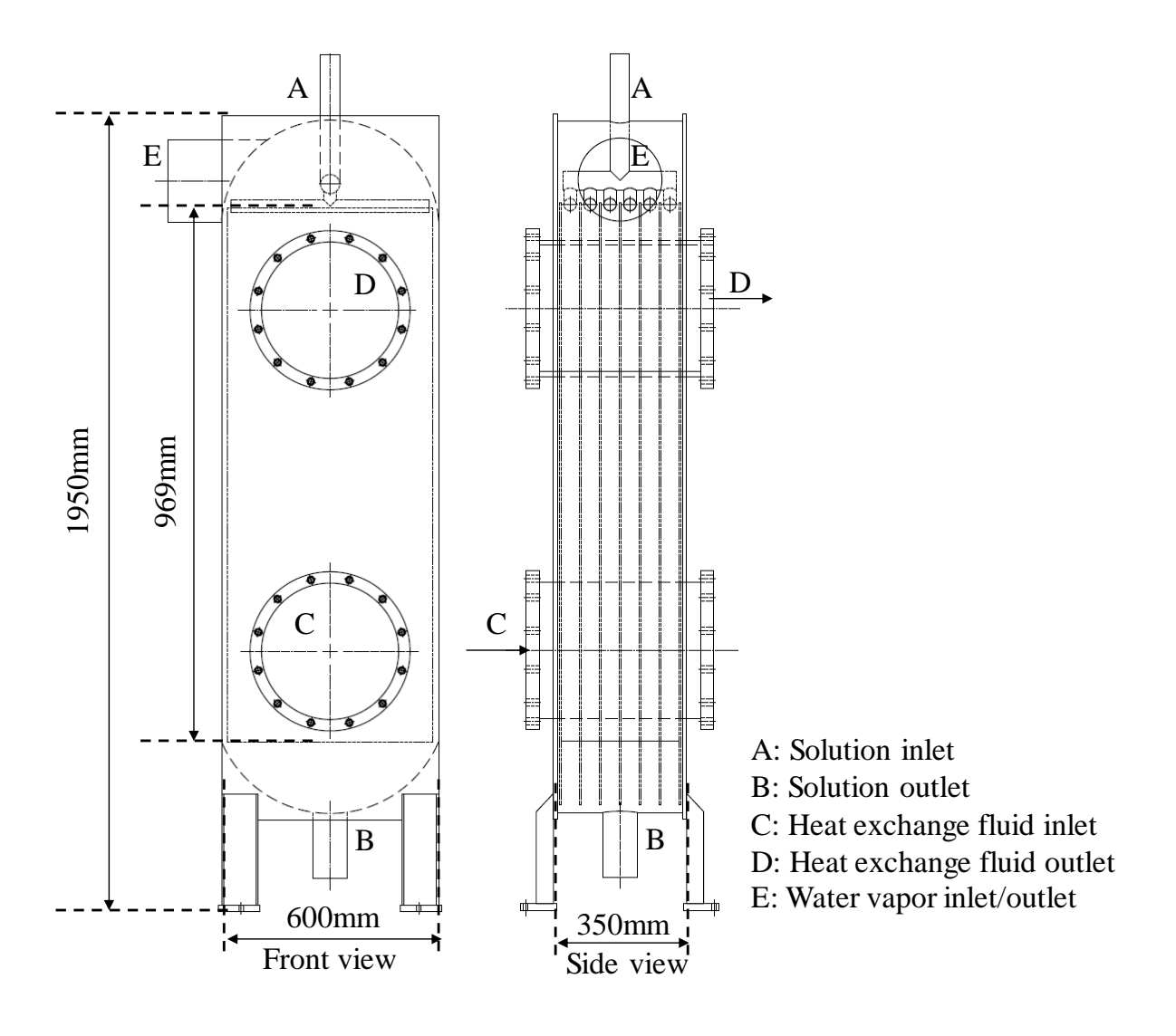


Figure 3.4 Structure of absorber/generator

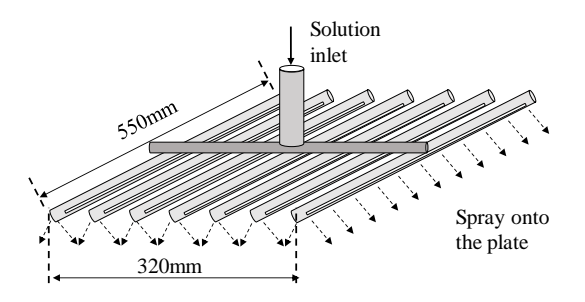


Figure 3.5 Structure of liquid distributor

#### 3.3.2 Storage tanks, thermostatic baths, electric heaters and chiller

Two storage tanks are situated beneath the two heat exchangers, one for solution storage and the other for refrigerant storage. The pumps used for solution and refrigerant are peristaltic pumps. Two thermostatic water baths, one on the solution side and the other on the water side,

are used to provide heat transfer fluids (i.e. water) to the two plate heat exchangers. Four water pumps are utilized to pump the heat transfer fluids into the heat exchangers. The temperatures of both thermostatic water baths are controlled and maintained by electric heaters and a chiller through PID control. To minimize the heat loss during experiments, all pipes, storage tanks and heat exchangers are wrapped with insulation materials, though not depicted in Figure 3.3 (a).

Static thermobaths, electric heaters, chiller are also important instruments to provide the heat transfer fluids and maintain their temperatures. The temperatures of heat transfer fluids in static thermobaths are controlled by PID control in the control cabinet.

#### 3.3.3 Measurement system and control cabinet

The system's pressure, the solution, water and heat transfer fluids' temperature and flow rate are measured, the measuring points are marked in Figure 3.2. All the data from these measurements are collected by a data acquisition system in a control cabinet and stored on a computer. Temperature data are obtained using thermometers. The flow rates of the heat transfer fluids were controlled by electromagnetic valves and measured using electromagnetic flow rate meters. The solution and refrigerant water flow rates are controlled by adjusting the frequency of the corresponding water pumps and measured by turbine flow meters. The solution's concentration before and during the charging and discharging experiments is calculated based on density measurements taken by a float densitometer and liquid level measurements taken by level gauges, respectively. The specifications of the primary measuring instruments can be found in Table 3.5. All the sensors are calibrated before the experiments.

Table 3.5 Specifications of measurement instruments

Devices	Measured quantities	Type	Accuracy	Range	
Thermometer	Fluid's temperature	Pt RTD	0.25%	-50∼100°C	
Pressure transducer	System working pressure	Diffusion silicon pressure transducer	0.5%	-100∼100kpa	
Solution flow meter	Flow rate of solution and refrigerant (water)	Turbine flowmeter	1%	$0.6\sim$ 6 $m^3/h$	
Water flow meter	Flow rate of heat transfer fluids (water)	Electromagnetic	0.5%	$0\sim$ $20$ m $^3$ /h	
Liquid level meter	Liquid level	Scale plate liquid level meter	0.1cm	0∼50cm	
Density meter	Solution's density	Float densitometer	0.01g/ cm <sup>3</sup>	1.20- 1.30g/cm <sup>3</sup>	

# 3.4 Modeling of Absorption Thermal Energy Storage System

## 3.4.1 Modeling of absorption thermal energy storage system

The modeling of the charging and discharging processes is based on the following assumptions: (1) During the charging and discharging processes, the solution temperature and concentration in the solution tank are uniform, and the water temperature in the water tank is uniform. (2) The vapor pressure drop in the heat exchanger and vapor pipe can be ignored. (3) The system's heat loss to the surroundings can be ignored. (4) The heat loss in the heat

exchangers can be ignored. (5) The heat capacities of the components, including heat exchangers, pipes, pumps, measurement instruments etc are ignored. (6) The heat transfer coefficients of both heat exchangers are constant during the charging and discharging processes. (7) No heat loss during the mixing process between the solution at the heat exchanger outlet and the solution in the solution tank. (8) The flash evaporation at the beginning of the charging and discharging processes is ignored.

The dynamic modeling of the three-phase absorption TES cycle is based on energy and mass conservations. In the charging process, the solution is charged by an external heat source in the generator. The heat and mass transfer process in the generator is governed by Eqs. (1-5).

$$q_{\text{cha,s}}(\tau) = \frac{d[M_{\text{sg}} \cdot h_{\text{s}}]}{d\tau} + \dot{m}_{\text{v}} \cdot h_{\text{l}}$$
 (1)

$$m_{\rm v} = \frac{dM_{\rm sg}}{d\tau} \tag{2}$$

$$q_{\rm cha,w}(\tau) = C_{pw}(\tau) \cdot \dot{m}_{\rm g}(\tau) \cdot (T_{\rm g,out}(\tau) - T_{\rm g,in}(\tau)) \tag{3}$$

$$q_{\text{cha,w}}(\tau) = UA_{g} \cdot \frac{(T_{g,\text{in}}(\tau) - T_{g,\text{out}}(\tau))}{\ln\left[\frac{T_{g,\text{in}}(\tau) - T_{g}(\tau)}{T_{g,\text{out}}(\tau) - T_{g}(\tau)}\right]}$$
(4)

$$q_{\text{cha.s}}(\tau) = q_{\text{cha.w}}(\tau) \tag{5}$$

where,  $q_{\rm cha,s}$  and  $q_{\rm cha,w}$  stand for the charging rate calculated from solution heat gain and hot water heat release;  $\tau$  is time;  $M_{\rm sg}$  is the solution in the generator;  $\dot{m}_{\rm v}$  is the vapor's mass flow rate, kg/s;  $h_{\rm s}$  and  $h_{\rm l}$  are the solution's enthalpy and the latent heat of water vapor, respectively;  $C_{\rm pw}$  is the specific heat capacity of hot water in the generator;  $\dot{m}_{\rm g}$  is the flow rate of hot water inside the generator.  $T_{\rm g,out}$ ,  $T_{\rm g,in}$  and  $T_{\rm g}$  are the hot water outlet and inlet temperatures in the generator, and generation temperature, respectively;  $UA_{\rm g}$  is the product of the heat transfer coefficient and heat transfer area of the generator.

The enthalpy of the working fluid is calculated using correlations provided by Chaudhari and Patil (2002). The specific heat capacity of the solution is calculated using the correlations provided by Conde (2004). Since crystallization may happen at a high concentration, the mass conservation in the solution tank is expressed as Eqs. (6-7). Since the heat loss during the solution mixing process is neglected, the enthalpy change in the solution tank is equal to the solution enthalpy change in the generator, as shown in Eq. (8):

$$\frac{\mathrm{d}M_{\mathrm{S}}(\tau)}{\mathrm{d}\tau} = -\dot{m}_{\mathrm{v}} - \dot{m}_{\mathrm{cry}} \tag{6}$$

$$\frac{\mathrm{d}[M_{\mathrm{s}}(\tau)\cdot X(\tau)]}{\mathrm{d}\tau} = -\dot{m}_{\mathrm{cry}} \tag{7}$$

$$\frac{\mathrm{d}[M_{\mathrm{S}}(\tau) \cdot h_{\mathrm{S}}(\tau)]}{\mathrm{d}\tau} = \frac{d[M_{\mathrm{Sg}} \cdot h_{\mathrm{S}}]}{d\tau} \tag{8}$$

where,  $M_s$  is the solution mass;  $\dot{m}_{cry}$  is the crystallization rate; X is the solution concentration.

The generated water vapor from the generator is condensed and collected in the water tank.

The energy and mass conservations in the condenser and water tank are governed by Eqs. (914):

$$\frac{\mathrm{d}M_{\mathrm{rc}}(\tau)}{\mathrm{d}\tau} = \dot{m}_{\mathrm{v}} \tag{9}$$

$$q_{c,r}(\tau) = \dot{m}_{v} \cdot h_{l} - \frac{d[M_{r}(\tau) \cdot h_{r}]}{d\tau}$$
(10)

$$q_{c,w}(\tau) = C_{pw}(\tau) \cdot \dot{m}_c \cdot (T_{c,out}(\tau) - T_{c,in}(\tau))$$
(11)

$$q_{c,w}(\tau) = -UA_c \cdot \frac{(T_{c,in}(\tau) - T_{c,out}(\tau))}{ln\left[\frac{T_c(\tau) - T_{c,out}(\tau)}{T_c(\tau) - T_{c,in}(\tau)}\right]}$$
(12)

$$q_{c,r}(\tau) = q_{c,w}(\tau) \tag{13}$$

$$\frac{\mathrm{d}[M_{\mathrm{rc}}(\tau)\cdot h_{\mathrm{r}}]}{\mathrm{d}\tau} = \frac{\mathrm{d}[M_{\mathrm{r}}(\tau)\cdot h_{\mathrm{r}}]}{\mathrm{d}\tau} \tag{14}$$

where,  $M_{\rm rc}(\tau)$  and  $M_{\rm r}(\tau)$  are the mass of refrigerant water in the condenser and the total mass of refrigerant, respectively;  $q_{\rm c,r}$  and  $q_{\rm c,w}$  are the condensation heat calculated from refrigerant

enthalpy change and heat rejected to the cooling water;  $h_r$  is the refrigerant enthalpy;  $\dot{m}_c$  is the flow rate of cooling water inside the condenser;  $T_{c,out}$ ,  $T_{c,in}$  and  $T_c$  are the condenser outlet and inlet water temperature, and condensation temperature, respectively.  $UA_c$  is the product of heat transfer coefficient and heat transfer area of the condenser.

The total charged heat is the integration of  $q_{\mathrm{cha,s}}(\tau)$  along the charging process:

$$Q_{\text{cha,s}} = \int q_{\text{cha,s}}(\tau) \tag{15}$$

In the discharging process, the refrigerant water evaporates in the evaporator. The cooling discharge rate equals the evaporation heat  $q_e$ . The heat and mass balance in the evaporator can be calculated using Eqs. (15-19).

$$\frac{\mathrm{d}M_{\mathrm{re}}(\tau)}{\mathrm{d}\tau} = -\dot{m}_{\mathrm{v}} \tag{16}$$

$$q_{\rm e,r}(\tau) = \dot{m}_{\rm v} \cdot h_{\rm l} + \frac{\mathrm{d}[M_{\rm re}(\tau) \cdot h_{\rm r}]}{\mathrm{d}\tau}$$
 (17)

$$q_{e,w}(\tau) = C_{pw}(\tau) \cdot \dot{m}_e \cdot (T_{e,in}(\tau) - T_{e,out}(\tau))$$
(18)

$$q_{e,w}(\tau) = UA_e \cdot \frac{(T_{e,in}(\tau) - T_{e,out}(\tau))}{ln \left[ \frac{T_{e,in}(\tau) - T_{e}(\tau)}{T_{e,out}(\tau) - T_{e}(\tau)} \right]}$$
(19)

$$q_{\rm e,r}(\tau) = q_{\rm e,w}(\tau) \tag{20}$$

$$\frac{\mathrm{d}[M_{\mathrm{re}}(\tau)\cdot h_{\mathrm{r}}]}{\mathrm{d}\tau} = \frac{\mathrm{d}[M_{\mathrm{r}}(\tau)\cdot h_{\mathrm{r}}]}{\mathrm{d}\tau} \tag{21}$$

where,  $M_{\rm re}$  is the mass of refrigerant in the evaporator;  $q_{\rm e,r}$  and  $q_{\rm e,w}$  represent the evaporation heat calculated from refrigerant enthalpy change and heat input by chilled water, respectively;  $\dot{m}_{\rm e}$  is the flow rate of chilled water inside the evaporator;  $T_{\rm e,in}$ ,  $T_{\rm e,out}$  and  $T_{\rm e}$  are the chilled water inlet temperature, outlet temperature and evaporation temperature, respectively;  $UA_{\rm e}$  is the product of the heat transfer coefficient and heat transfer area of the evaporator.

The evaporated refrigerant water vapor is absorbed by the solution in the absorber, which produces a heating effect in the absorber. The heat and mass transfer processes in the absorber are expressed as Eqs. (22-26):

$$q_{\text{dis,s}}(\tau) = -\frac{d[M_{\text{sa}} \cdot h_{\text{s}}]}{d\tau} + \dot{m}_{\text{v}} \cdot h_{\text{l}}$$
 (22)

$$m_{\rm v} = \frac{dM_{\rm Sa}}{d\tau} \tag{23}$$

$$q_{\rm dis,w}(\tau) = C_{\rm pw}(\tau) \cdot \dot{m}_{\rm a}(\tau) \cdot (T_{\rm a,out}(\tau) - T_{\rm a,in}(\tau)) \tag{24}$$

$$q_{\text{dis,w}}(\tau) = -UA_{g} \cdot \frac{(T_{a,\text{in}}(\tau) - T_{a,\text{out}}(\tau))}{\ln\left[\frac{T_{\text{dis}}(\tau) - T_{a,\text{out}}(\tau)}{T_{\text{dis}}(\tau) - T_{a,\text{in}}(\tau)}\right]}$$
(25)

$$q_{\rm dis,s}(\tau) = q_{\rm dis,w}(\tau) \tag{26}$$

Where,  $q_{\rm dis,s}$  and  $q_{\rm dis,w}$  are the discharging rate calculated from solution enthalpy change and heated water temperature rise;  $M_{\rm sa}$  is the solution in the absorber;  $\dot{m}_{\rm a}$  is the flow rate of heated water in the absorber;  $T_{\rm a,in}$ ,  $T_{\rm a,out}$  and  $T_{\rm dis}$  are the heated water inlet temperature, outlet temperature and discharging temperature, respectively;  $UA_{\rm a}$  is the product of the heat transfer coefficient and heat transfer area of the absorber.

After absorbing the water vapor, the solution in the generator is then mixed with the solution in the solution tank. The heat and mass balance are governed by Eqs. (27-29):

$$\frac{\mathrm{d}M_{\mathrm{s}}(\tau)}{\mathrm{d}\tau} = \dot{m}_{\mathrm{v}} + \dot{m}_{\mathrm{cry,d}} \tag{27}$$

$$\frac{\mathrm{d}[M_{\mathrm{s}}(\tau)\cdot X(\tau)]}{\mathrm{d}\tau} = \dot{m}_{\mathrm{cry,d}} \tag{28}$$

$$\frac{\mathrm{d}[M_{\mathrm{S}}(\tau) \cdot h_{\mathrm{S}}(\tau)]}{\mathrm{d}\tau} = \frac{\mathrm{d}[M_{\mathrm{Sa}} \cdot h_{\mathrm{S}}]}{d\tau} \tag{29}$$

where,  $\dot{m}_{\rm cry,d}$  is the dissolution rate of the crystals.

The total discharged heat  $(Q_{\rm dis,h})$  and cold  $(Q_{\rm dis,c})$  are the integration of  $q_{\rm dis,w}(\tau)$  and  $q_{\rm e,r}(\tau)$  over the charging process, respectively:

$$Q_{\rm dis,h} = \int q_{\rm dis,w}(\tau) \tag{30}$$

$$Q_{\rm dis,c} = \int q_{\rm e,r}(\tau) \tag{31}$$

Error analysis is crucial for quantifying and understanding the sources of variability and inaccuracies in data. The error of the ESD (u) can be calculated using Eq.(16), which takes into account the measurement uncertainties of each measurement device (u<sub>i</sub>) listed in Table 3.5.

$$u^2 = \sum_{i=1}^{N} \left(\frac{\partial f}{\partial x_i}\right)^2 u_i^2(x_i)$$
 (32)

where, N represents the number of variables that influence the value of ESD, while each individual variable is denoted as  $x_i$ .

### 3.4.2 Performance evaluation of absorption thermal energy storage

Several performance indexes are commonly used to evaluate the performance of absorption TES, including ESD, energy storage efficiency (ESE), temperature effectiveness (TE), etc. ESD is a critical parameter that reflects the storage capability of absorption TES materials and systems. The ESD can be further divided into volumetric ESD ( $ESD_v$ ) and gravimetric ESD ( $ESD_g$ ) based on the different baselines. The  $ESD_v$  analyzes the amount of energy stored in a single unit volume while  $ESD_g$  represents the amount of energy stored per unit mass of the storage materials, as shown in Eqs (32-33).

$$ESD_{v} = \frac{Q_{\text{dis}}}{V} \tag{32}$$

$$ESD_g = \frac{Q_{\text{dis}}}{M} \tag{33}$$

Energy storage efficiency, defined as the ratio of energy output (discharged) to the total energy input (charged) during the charging process, is a critical measure of the effectiveness of absorption TES systems.

$$ESE = \frac{Q_{\text{dis}}}{Q_{\text{cha}}} \tag{34}$$

Temperature effectiveness is defined as the ratio of solution temperature lift during the discharging process and solution temperature lift during the charging process (Fumey et al.).

TE can be used to evaluate the thermal management performance of absorption TES systems.

$$TE = \frac{T_{dis,t} - T_{dis,i}}{T_{cha,t} - T_{cha,i}} \tag{35}$$

# Chapter 4 Novel Modified LiCl Solution for Three-phase Absorption Thermal Energy Storage

# 4.1 Analysis of Three-phase Absorption Thermal Energy Storage Cycle

## 4.2.1 Crystallization fundamentals

The crystallization process often consists of two major steps, nucleation and growth. When the concentration is larger than the corresponding solubility, the solution is supersaturated. Supersaturation is the driving force for both nucleation and crystal growth (Him and Myerson, 1996). The required driving force, or supersaturation degree, for nucleation, is higher than that for crystal growth. Therefore, as shown in Figure 4.1, the supersaturated solution has metastable and labile states depending on the supersaturation degree. In the metastable zone, crystals can grow but nucleation cannot occur spontaneously unless additional nucleation agents or external disturbances are introduced (Ulrich and Strege, 2002). In the labile zone, nucleation and growth will occur simultaneously. The boundary between the metastable and the labile zone is the supersolubility curve, the dashed curve in Figure 4.1.

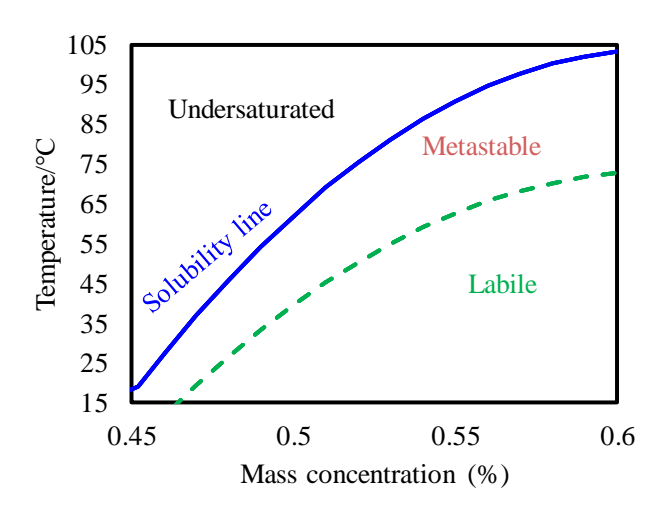


Figure 4.1 Schematic diagram of the state of LiCl solution near the crystallization line

Additives can be used to modify the solubility and crystallization properties of the supersaturated solution. Crystallization inhibitors and nucleating agents are both widely used. Crystallization inhibitors can prevent the nucleation of supersaturated alkali halide solutions

and therefore reduce crystallization temperature (Inada et al., 2019). Additionally, they can increase the metastable zone width of the solution and stabilize the solution at this state (Beckmann, 2013). However, crystallization inhibitors cannot promote the growth of crystals slurry when the concentration is higher than the corresponding solubility. Nucleating agents, on the other hand, can facilitate nucleation and promote the formation of fine crystals in the metastable zone. As a result, the solution becomes slurry, which can guarantee fluidity and avoid the blockage of pipes. The joint effect of both additives requires further experimental studies. The choice of one additive or both additives depends on the working concentration difference of the modified LiCl solutions.

#### 4.2.2 Modeling of absorption TES cycle

A complete working cycle of absorption TES consists of charging and discharging processes, as shown in Figure 4.2. In the charging process, waste heat or solar energy can be used to desorb and concentrate the dilute solution, transforming the low-grade heat into chemical potential stored in the concentrated solution. The desorbed water vapor is condensed in the condenser and the heat is rejected to a heat sink. In the discharging process, the concentrated solution absorbs water vapor from the evaporator and becomes diluted. The dilution of the concentrated solution has a heating effect while the water evaporation leads to a cooling effect, which enables the discharging process to supply heat and cooling energy simultaneously. It is another advantage of absorption TES over sensible and latent TES. In absorption TES, the thermal energy is stored due to the concentration difference between the concentrated and diluted solution. Increasing this concentration difference can significantly increase the energy stored. Crystals will grow in the concentrated solution when the concentration is higher than the corresponding solubility.

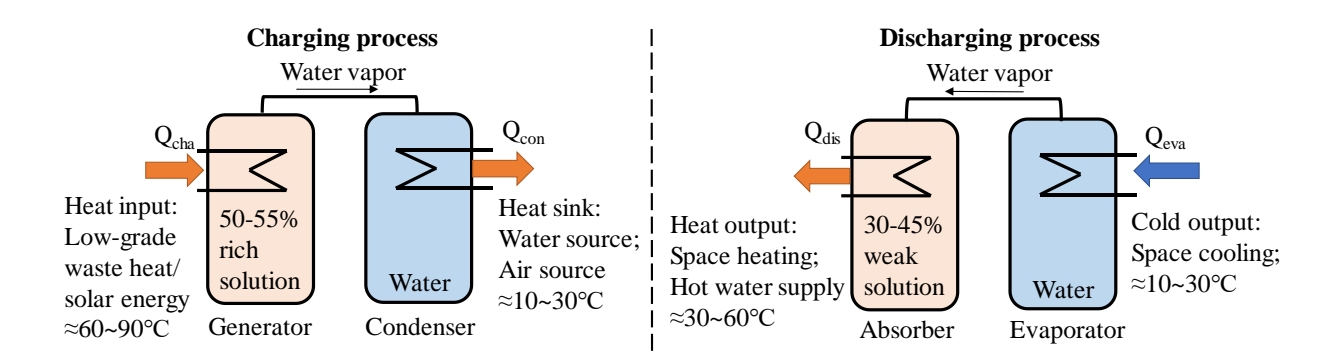


Figure 4.2 Schematic of the working principle of absorption TES: charging and discharging process

Figure 4.3 compares the pressure-temperature-concentration (p-T-x) diagram of a typical LiCl absorption TES cycle (1-2-3-4-5) and three-phase LiCl absorption TES cycle (1'-2'-3'-4'-5'). Processes 1-2-3/1'-2'-3', 3-4/3'-4', and 4-5-1/4'-5'-1' represent charging, storage and discharging respectively. The transition points on the cycle are determined by the temperatures in each process. The charging temperature  $T_{\rm cha}$  and discharging temperature  $T_{\rm dis}$  influence the concentration difference. The condensation temperature  $T_{\rm con}$  and evaporation temperature  $T_{\rm eva}$  determine the condensation and evaporation pressure levels  $p_{\rm con}$  and  $p_{\rm eva}$ . In a typical absorption TES cycle without additives, the concentration at state 3 is limited by the solubility of the LiCl solution. When additives are introduced, the concentration difference in three-phase absorption TES expands as undersaturated State 3 moves to supersaturation State 3'. Solubility is also modified by additives.

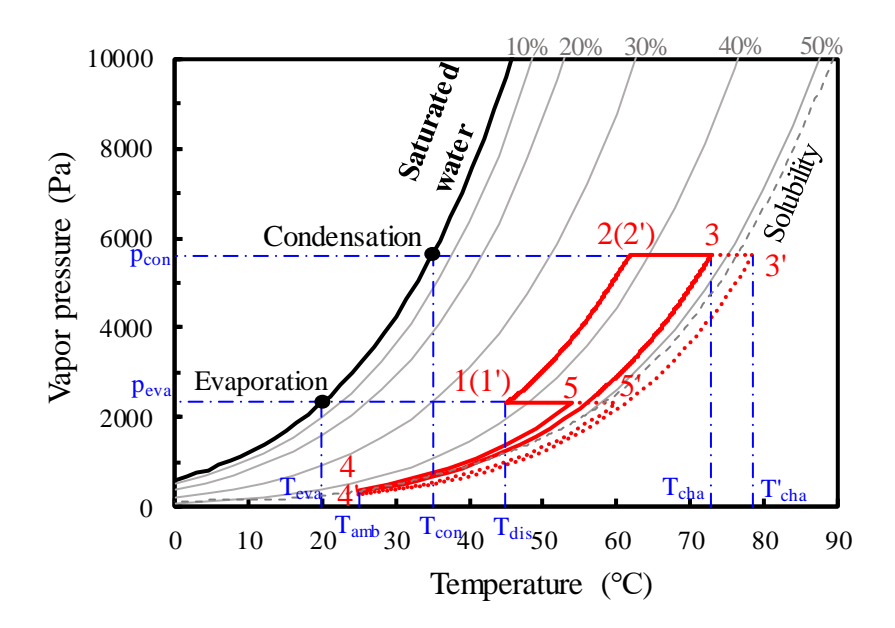


Figure 4.3 Pressure-temperature-concentration (p-T-x) diagram of LiCl absorption TES cycle

ESD calculation is based on the p-T-x diagram of the LiCl absorption TES cycle. In the charging process 1-2-3, the dilute solution at State 1 is heated by an external heat source at  $T_{\rm cha}$ . The solution's temperature increases until State 2, where its vapor pressure reaches the saturation vapor pressure  $p_{\rm con}$  at  $T_{\rm con}$ . After that, water vapor desorbs from the solution continuously until reaching an equilibrium at State 3. The desorbed water vapor is condensed and stored in the condenser. The concentration at State 3 is generally lower than the solubility at ambient temperature to avoid crystallization at the storage state. The enthalpy and vapor pressure of the solution at a given temperature and concentration can be calculated from fitting equations provided by Conde (2004).

The working conditions for ESD calculation are shown in Table 4.1, which correspond to the typical working conditions for heat and cold supply. The concentration after charging  $(x_3)$  is assumed to equal the solubility at around 25°C to avoid crystallization at the  $T_{\rm amb}$  during the storage process. The concentration after discharging  $(x_1)$  is determined by the required discharging temperature at evaporation pressure.

Table 4.1 Reference working conditions for ESD calculation

	Working conditions	Heat storage	Cold storage		
Cl	Charging temperature $T_{\rm cha}/^{\circ}{ m C}$	85	85		
Charging	Concentration after charging $x_3/\%$	Depends on solubility at $T_{amb}$			
process	Condensation temperature $T_{\rm con}$ /°C	30	30		
Storage	Ambient temperature $T_{\rm amb}$ / $^{\circ}$ C	25	25		
<b>.</b>	Evaporation temperature $T_{\rm eva}$ /°C	15	7		
Discharging	Concentration after discharging $x_1/\%$	35	41		
	Discharging temperature $T_{\rm dis}$ /°C	35	35		

The charging heat (i.e. the heat input of processes 1-2  $(Q_{1-2})$  and 2-3  $(Q_{2-3})$ ) as well as the condensation heat during charging can be calculated based on the energy and mass balance, as shown in Eq.(1)-(5):

$$Q_{1-2} = M_{s2}h_{s2} - M_{s1}h_{s1} \tag{1}$$

$$Q_{2-3} = M_{s3}h_{s3} - M_{s2}h_{s2} + \int_{T_2}^{T_3} m_{\rm v}h_{\rm v} dT + m_{\rm v} \int_{\rm T}^{T_3} c_{p\rm v} dT \tag{2}$$

$$Q_{\rm con} = M_{\rm v} h_{\rm l} + M_{\rm v} \int_{T_{\rm con}}^{T_3} c_{pv} dT$$
 (3)

$$M_{s1} = M_{s2} \tag{4}$$

$$M_{\rm v} = M_{\rm s2} - M_{\rm s3} = \int_{T_2}^{T_3} m_{\rm v} dT \tag{5}$$

where  $h_s$  stands for the solution enthalpy at each state.  $h_v$  represents the specific enthalpy of water vapor while  $h_l$  represents the latent heat of condensation or evaporation, both are the

function of temperature.  $M_s$  is the solution mass at each state,  $m_v$  is the mass flow of water vapor during temperature change.

Following the charging process, the concentrated solution and water are separately stored in different tanks. The solution temperature drops to the ambient temperature  $T_{abm}$  during the energy storage process. The sensible heat loss during this process equals the enthalpy change of the concentrated solution and condensed water, which can be calculated by Eq.(6) and (7):

$$Q_{3-4} = -(M_{s4}h_{s4} - M_{s3}h_{s3}) + M_{v} \int_{T_{amb}}^{T_{con}} c_{pw} dT$$
 (6)

$$M_{s3} = M_{s4}$$
 (7)

In the discharging process 4-5-1, water evaporation and water vapor absorption happen simultaneously. Liquid water undergoes a phase change in the evaporator, which extracts heat and produces a cooling effect. The evaporation heat ( $Q_{\text{eva}}$ ) is given by Eq.(8). The solution at State 4 absorbs water vapor and releases heat. The total discharging heat consists of the phase change heat of water vapor and the enthalpy change of the solution due to dilution. However, State 5 in the p-T-x diagram is uncertain, which is related to the real discharge process. Therefore, the discharging heat ( $Q_{\text{dis}}$ ) is calculated based on the energy balance of a complete absorption cycle in Eq.(10).

$$Q_{\text{eva}} = M_{\text{v}} h_{\text{l}} - M_{\text{v}} \int_{T_{\text{eva}}}^{T_{\text{amb}}} c_{pw} dT$$
 (8)

$$M_{\rm v} = M_{\rm S1} - M_{\rm S4} \tag{9}$$

$$Q_{\text{dis}} = Q_{4-5-1} = Q_{1-2} + Q_{2-3} + Q_{\text{eva}} - Q_{\text{con}} - Q_{3-4}$$
 (10)

Since the discharging process produces both heating and cooling effects, ESD can be represented as heat storage density (ESD<sub>h</sub>) or cold storage density (ESD<sub>c</sub>). The heat output by

heating and cooling effects are calculated by  $Q_{dis}$  and  $Q_{eva}$  respectively. ESD<sub>h</sub> and ESD<sub>c</sub> are defined as the ratio of discharging and evaporation heat on the total mass of solution at State 1, which are shown in Eq. (11) and (12):

$$ESD_{h} = Q_{dis}/M_{s1} \tag{11}$$

$$ESD_c = Q_{eva}/M_{s1} \tag{12}$$

In calculating ESD of the three-phase absorption TES, the influences of additives on solution enthalpy change and the crystallization enthalpy  $(h_{cr})$  should be considered. Two methods are adopted to determine the solution enthalpy change during charging and storage processes. The first one is to measure the enthalpy change of the solution using differential scanning calorimetry (DSC). The second one is to calculate the enthalpy of the mixed solution by adding the enthalpy values of the individual component. The mixing enthalpy, which is the enthalpy liberated or absorbed from a substance upon mixing, is assumed to be 0. The second method is more convenient in engineering applications; however, its accuracy needs to be verified by the results of the DSC measurement. The definitions of concentration of the LiCl solution with and without additives are the same in this study. The enthalpy and vapor pressure of the LiCl solution are assumed to be not influenced by the additives. For crystallization enthalpy, the crystals are mainly monohydrate LiCl in the typical working temperature range of the three-phase absorption TES cycle. The crystallization enthalpy  $h_{\rm cry}$  is assumed to be constant in the temperature and concentration range. The crystallization enthalpy of monohydrate LiCl can be calculated from the standard enthalpy of formation (Monnin et al., 2002), which is shown in Eq.(13).

$$h_{\text{cry}} = \Delta H_f^0(\text{LiCl} \cdot \text{H}_2\text{O(s)}) - \Delta H_f^0(\text{LiCl(aq)}) - \Delta H_f^0(\text{H}_2\text{O(l)})$$
(13)

where  $\Delta H_{\rm f}^0({\rm LiCl}\cdot {\rm H_2O(s)})$ ,  $\Delta H_{\rm f}^0({\rm LiCl(aq)})$  and  $\Delta H_{\rm f}^0({\rm H_2O(l)})$  represent the standard enthalpy of formation of LiCl monohydrate, LiCl solution at standard concentration and water respectively.

In the charging process of the three-phase absorption TES cycle (i.e. process line 1'-2'-3'), crystallization can happen in process 2'-3' with the increase of concentration. The heat absorbed in process 1'-2' ( $Q_{1'-2'}$ ) and process 2'-3' ( $Q_{2'-3'}$ ) are calculated using Eq.(14) and Eq.(15). Crystallization may happen when the solution concentration exceeds the solubility. The required charging heat is higher than the conventional cycle as additives also absorb heat, i.e. the last term in Eq. (14) and Eq. (15). In the storage period 3'-4', crystallization may happen when the solution temperature decreases during the storage process, particularly in long-term storage. The sensible heat loss during this period is calculated by Eq.(16). The condensation heat ( $Q_{con}$ ) and evaporation heat ( $Q_{eva}$ ) are not influenced by additives. The discharging heat ( $Q_{dis}$ ') is also obtained based on the energy balance of the whole cycle as shown in Eq.(17). Heat and cold storage density, i.e. ESD'<sub>h</sub> and ESD'<sub>c</sub> of the three-phase absorption TES are defined as Eq.(18) and (19), in which the mass of additives ( $M_{add}$ ) are considered.

$$Q_{1'-2'} = M_{s2'}h_{s2'} - M_{s1'}h_{s1'} + \int_{T_{1'}}^{T_{2'}} M_{add}c_{p,add}dT$$
 (14)

$$Q_{2'-3'} = M_{s3'}h_{s3'} - M_{s2'}h_{s2'} + \int_{T_{2'}}^{T_{3'}} m_{v}h_{v} dT + m_{v} \int_{T}^{T_{3'}} c_{pv} dT - M_{cry}h_{cry} + \int_{T_{2'}}^{T_{3'}} M_{add}c_{p,add} dT$$
(15)

$$Q_{3'-4'} = M_{s3'}h_{s3'} - M_{s4'}h_{s4'} + M_{v}\int_{T_{\text{amb}}}^{T_{\text{con}}} c_{pw}dT - M_{\text{cry}}h_{\text{cry}} - \int_{T_{3'}}^{T_{4'}} M_{\text{add}}c_{\text{p,add}}dT$$
(16)

$$Q_{\text{dis}}' = Q_{4'-5'-1'} = Q_{1'-2'} + Q_{2'-3'} + Q_{\text{eva}} - Q_{\text{con}} - Q_{3'-4'}$$
 (17)

$$ESD'_{h} = Q'_{dis}/(M_{s1'} + M_{add})$$
 (18)

$$ESD'_{c} = Q'_{eva}/(M_{s1'} + M_{add})$$
 (19)

# 4.2 Working Fluids for Three-Phase Absorption TES

## 4.2.1 Selection of working fluids and additives

By referring to previous research on crystallization control of the LiBr solution, EG and PG were the most widely adopted crystallization inhibitors and therefore they were considered as potential crystallization inhibitors of the LiCl solution in this study. Three types of widely-used nanoparticles were considered as potential nucleating agents, namely  $SiO_2$ ,  $\alpha$ - $Al_2O_3$  nanoparticles and multi-walled carbon nanotubes. It is not easy to realize the ideal dispersion of nanoparticles in the LiCl solution. Therefore, well-dispersed nanoparticles in the base fluid were used to modify the LiCl solution in the experiments carried out in this study.  $SiO_2$  and  $\alpha$ - $Al_2O_3$  nanoparticle dispersion in EG and PG with a mass fraction of 20%, and multi-walled carbon nanotubes dispersion in water with a mass fraction of 2.8% were used. All aqueous solutions of LiCl were prepared with distilled and deionized water.

Experiments were carried out to select the appropriate crystallization inhibitors and nucleation agents from the potential candidates. The solubility of LiCl in water containing different mass ratios of EG and PG was measured to select an appropriate crystallization inhibitor. The temperature is set at 25°C, which is the  $T_{\rm amb}$  in the calculation. Considering LiCl's poor solubility in EG and PG, the mass fraction of LiCl to LiCl+H<sub>2</sub>O is used to indicate the solubility of LiCl. Table 4.2 shows the solubility measurement results. Compared with PG, EG created a greater increase in LiCl's solubility in water and is therefore chosen as the crystallization inhibitor.

Table 4.2 Effect of EG and PG on LiCl's solubility in water

Mass ratio of LiCl solution: additive	LiCl mass fraction
LiCl solution without additives	0.458
LiCl solution: EG=8:1	0.467
LiCl solution: EG=5:1	0.485
LiCl solution: PG=8:1	0.463
LiCl solution: PG=5:1	0.472

To select the nucleating agents, the suspension of three nanoparticles in LiCl solution was tested. SiO<sub>2</sub> nanoparticles (SNPs) had the most stable suspension in the LiCl solution in the temperature range of 10-90 °C. An obvious separation of Al<sub>2</sub>O<sub>3</sub> nanoparticles and multi-walled carbon nanotube from the LiCl solution was observed at high temperatures. Therefore, SNPs were selected as nucleating agents. However, if add only the nucleating agent, the LiCl solution will crystalize at an even lower concentration compared with that of the pure LiCl solution, which reduces the working concentration difference. Only when it is combined with crystallization inhibitors, the LiCl solution may grow fine crystals at a concentration higher than its solubility.

Figure 4.4 shows the procedure adopted for searching the novel working fluids. Preselection shows that EG and SNPs are suitable additives. The solubility of LiCl in water with different mass fractions of EG was first measured to determine the optimal mass ratio of LiCl solution to EG. Suspension and crystal size measurements were then carried out to find the optimal mass ratio of LiCl solution to EG and SNPs. The concentration after charging is the maximum LiCl concentration that can fully dissolve for the solution with EG and the concentration that LiCl crystals have good suspension for the solution with EG and SNPs. The working concentration difference can be determined accordingly. Next, the enthalpy changes

of the novel working fluids at a given temperature range are determined by the experimental test of DSC or calculation. Then, the ESD is calculated using the enthalpy changes obtained from two methods, respectively. The working fluid with higher ESD was proposed for three-phase absorption TES. Last, vapor pressure, viscosity and density of the working fluids are also measured and compared.

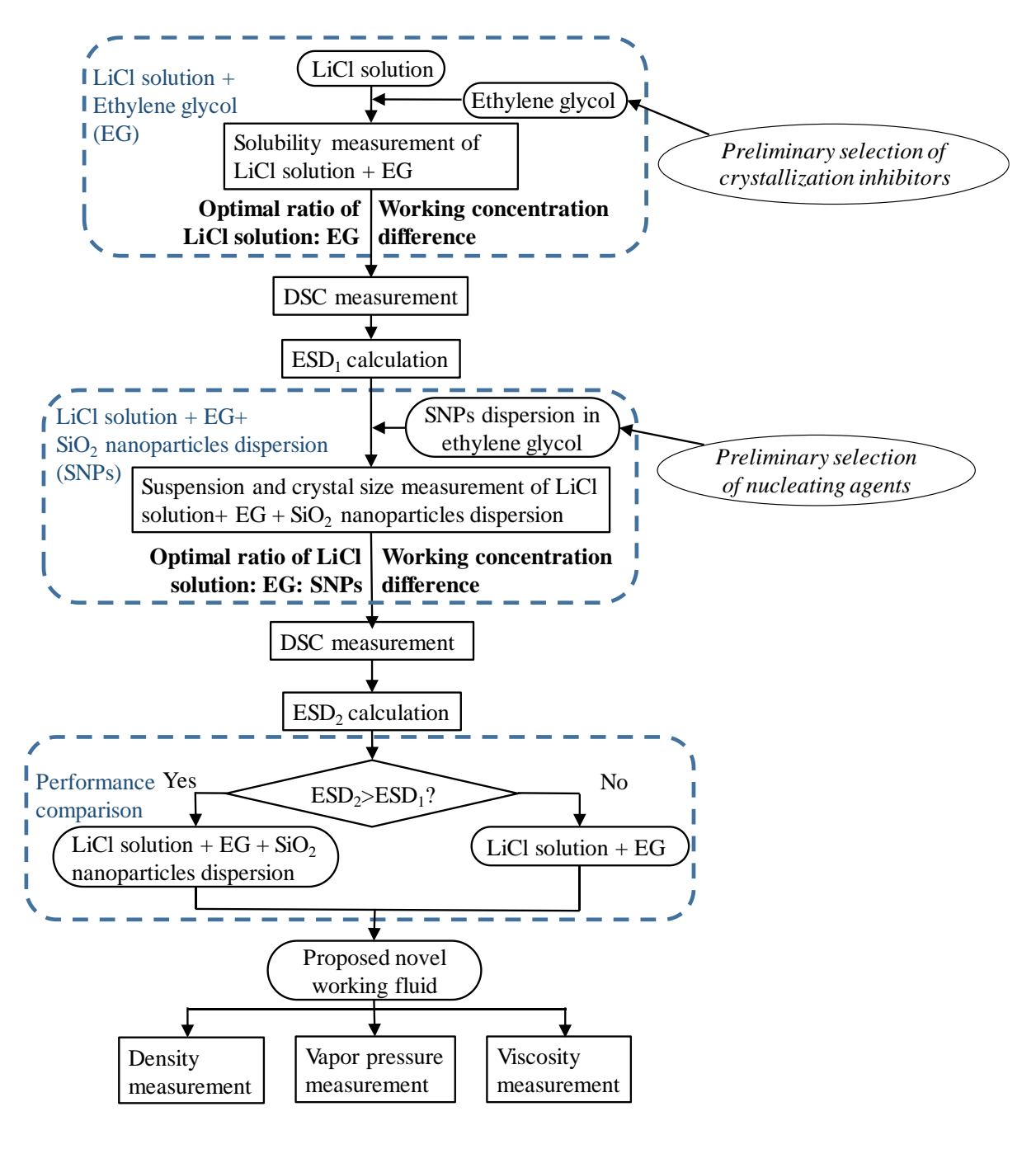


Figure 4.4 Procedure of novel working fluid preparation and thermal and physical properties

measurement

#### 4.2.2 Thermal and physical properties of the working fluids

Crystallization temperature of the LiCl/H<sub>2</sub>O-EG solution is important to determine the concentration difference and the ESD. The measured crystallization temperatures in LiCl solutions with EG are plotted in Figure 4.5. The solubility, i.e. the LiCl mass concentration at the corresponding crystallization temperature in the x-axis, increases significantly with the increase in the mass fraction of EG. Therefore, the working concentration difference increases with the increase in solubility, which is beneficial to enhance ESD.

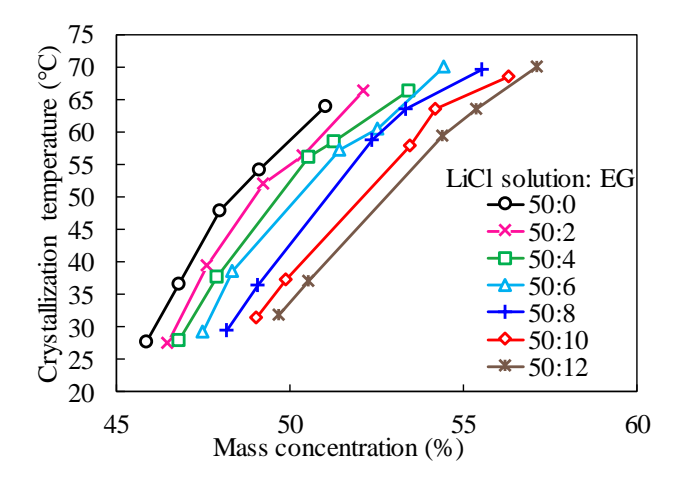


Figure 4.5 Crystallization temperature of LiCl/H<sub>2</sub>O-EG solution with a different mass fraction of EG

However, ESD does not necessarily increase with an increase in concentration difference. The mass of additives also has a strong impact on ESD since it consumes additional heat to charge but has no storage capability. Besides, the additives increase the total mass of the solution. The heat and cold storage density can be calculated using Eq. (3), (8) and (14)-(19). The impact of different mass ratios of LiCl solution: EG on ESD is shown in Figure 4.6. With an increase in EG, the heat storage density fluctuates slightly while the cold storage density gradually increases. However, the increase in cold storage density becomes less prominent when the mass ratio of LiCl solution: EG exceeds 50:10. When the mass ratio of LiCl solution: EG=50:10, heat storage density and cold storage density increase by 2% and 18.7%

respectively. Therefore, the optimal mass ratio of LiCl solution to additives is set to 50:10 in further experimental studies and analysis.

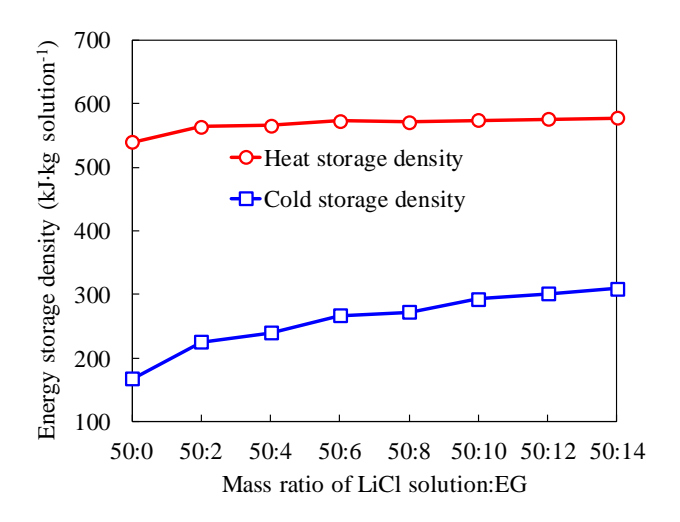


Figure 4.6 ESD of LiCl solution containing a different mass ratio of EG

EG can help reduce crystallization by decreasing the crystallization temperature of concentrated LiCl solution. However, crystal nucleation and growth may still take place when the concentration is higher than the solubility. SNPs can help modify the suspension and size of crystals to ensure good fluidity. Figure 4.7 vividly shows the suspension of LiCl monohydrate crystals in LiCl/H<sub>2</sub>O-EG-SNPs solution with different additive mass ratios. The solution was prepared and settled for 100 hours before observing the suspension. No bulky crystals form at a concentration of 53%. The suspension of LiCl crystals is improved after adding SNPs. When mass ratio LiCl solution: EG: SNPs=50:8.5:1.5, there is almost no visible separation between crystals and the solution and the solution becomes slurry, indicating good suspension.

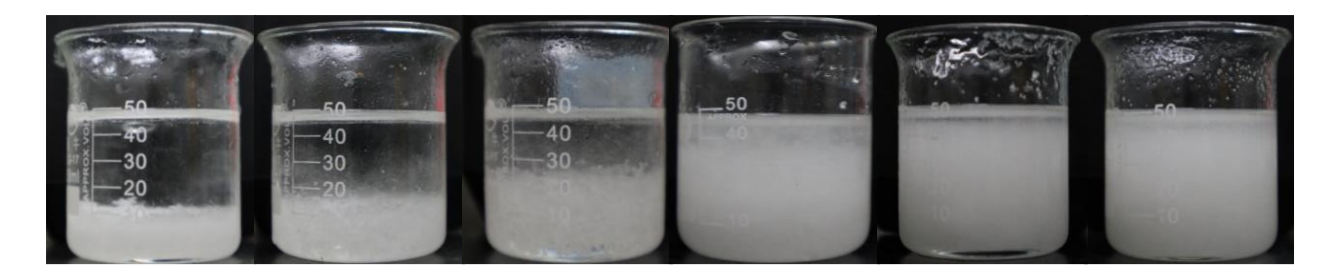


Figure 4.7 Suspension of crystals in 53% LiCl/H<sub>2</sub>O-EG-SNPs, where LiCl solution: EG: SiO<sub>2</sub>=50: x: y (by weight), from left to right: x=9.75, y=0.25; x=9.5, y=0.5; x=9.25, y=0.75; x=9, y=1; x=8.75, y=1.25; x=8.5, y=1.5

Figure 4.8 (a)-(d) show the crystal sizes in LiCl/H<sub>2</sub>O-EG-SNPs solutions with a different mass ratio of components. The solutions with a higher ratio of SNPs have a smaller crystal size. The minimum crystal size occurs at a mass ratio of LiCl solution: EG: SNPs=50:8.5:1.5 as shown in Figure 4.8 (d), which in accord with the one with the best suspension by direct observation. This can be attributed to the nucleation sites provided by SNPs. More nucleation sites for crystallization reduces the amount of LiCl that will grow on individual nucleation sites. The average crystal size therefore decreases. Smaller crystals are therefore easier to suspend in the solution. Thus, a mixed solution with a mass ratio LiCl solution: EG: SNPs= 50:8.5:1.5 is chosen for further study.

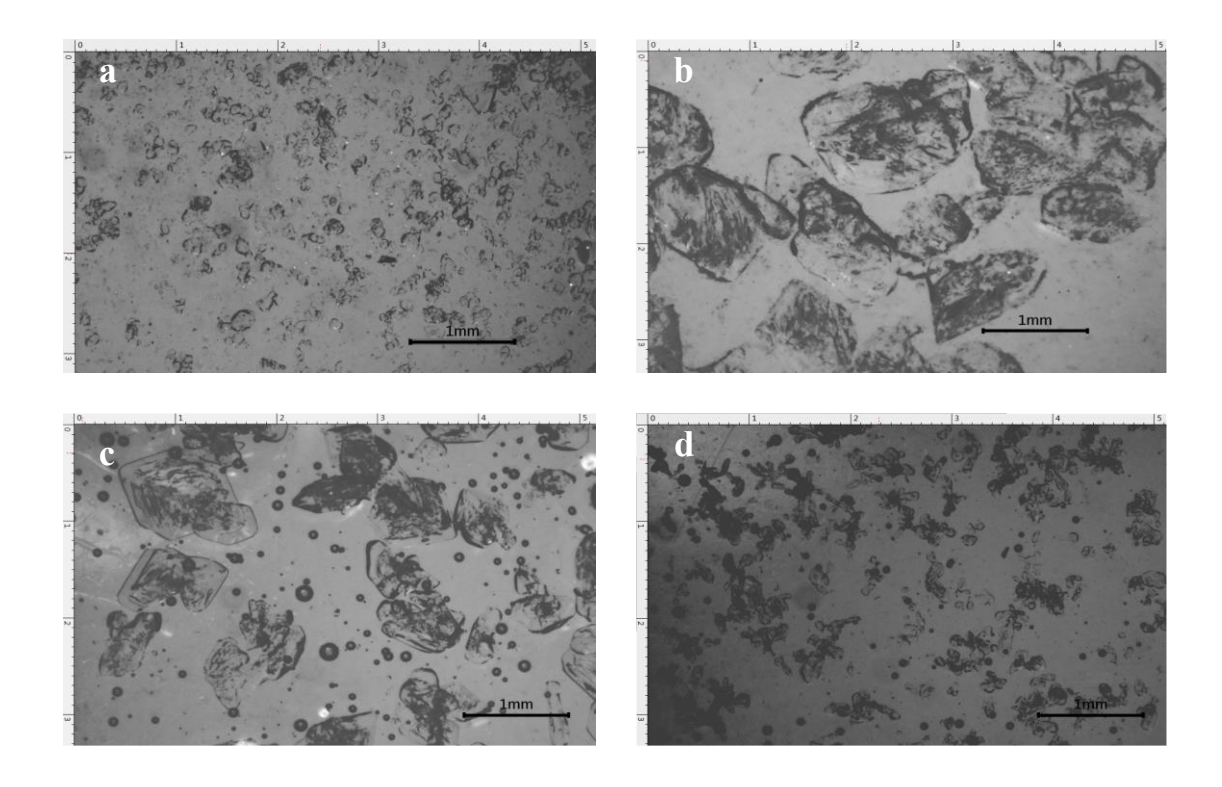


Figure 4.8 Crystal size of LiCl/H<sub>2</sub>O-EG-SNPs, where LiCl solution: EG: SiO<sub>2</sub>=50: x: y (by weight). (a) x=0,y=0; (b) x=10,y=0; (c) x=9.25, y=0.75; (d) x=8.5, y=1.5

For the LiCl/H<sub>2</sub>O-EG and LiCl/H<sub>2</sub>O-EG-SNPs solutions with optimal additive mass ratios, their vapor pressure, density and viscosity are measured with the LiCl concentration in water of 53%. As crystallization occurs in the LiCl solution with such a high concentration, the vapor pressure and density of the saturated LiCl solution are measured and compared. The viscosity of the LiCl solution is not presented in this study because the viscosity of the modified solutions and the LiCl solution are not comparable as the formers are non-Newtonian fluids and the latter is a Newtonian fluid.

Figure 4.9 shows the variations of vapor pressure with the temperature of the three solutions. The vapor pressure of LiCl/H<sub>2</sub>O-EG and LiCl/H<sub>2</sub>O-EG-SNPs are about the same across the working temperature range. Both are lower than the saturated LiCl solution, especially at high temperatures, leading to a favorable higher absorption rate and higher discharging temperature during the discharging stage. However, the vapor pressures of both modified solutions at  $T_{\rm cha}$ 

are still higher than the saturated vapor pressures at  $T_{\rm con}$ , which have a small impact on the vapor desorption of the charging process. The measured vapor pressures of the three solutions are fitted with the August Equation, Eq. (20), which is widely used to correlate the relationship between vapor pressure and temperature. A and B are concentration-dependent parameters, but they are constants here since the concentration in the measurement is fixed. The fitting coefficients A and B are determined by the least squares method, with results summarized in Table 4.3.

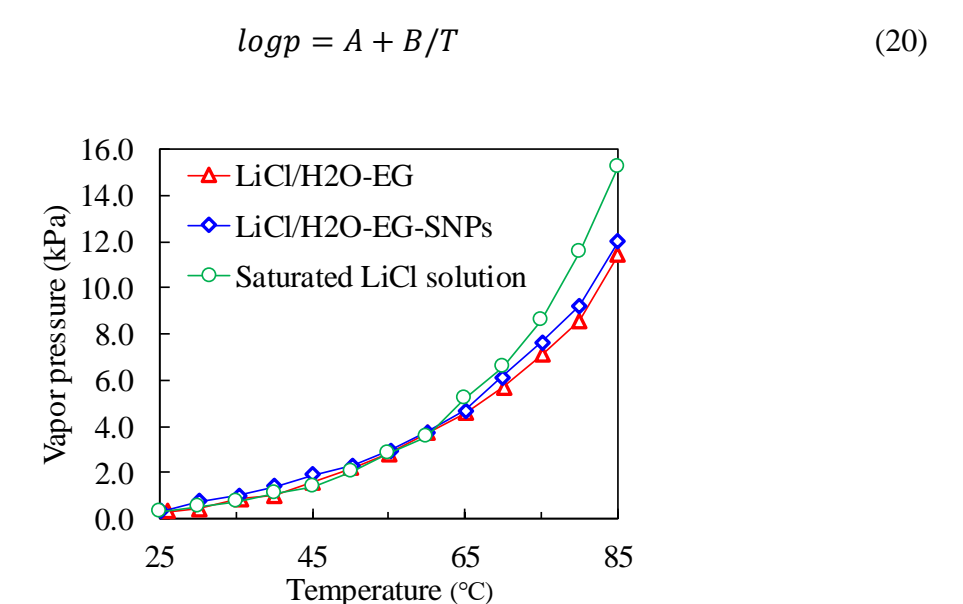


Figure 4.9 Vapor pressure of LiCl/H<sub>2</sub>O-EG, LiCl/H<sub>2</sub>O-EG-SNPs and saturated LiCl solution at different temperatures

Table 4.3 Correlation parameters in August Equation for three solutions at different temperatures

	A	В
Saturated LiCl solution	9.4488	-2.9579×10 <sup>3</sup>
LiCl/H <sub>2</sub> O-EG	8.7712	$-2.7534 \times 10^3$

The densities of the saturated LiCl solution, LiCl/H<sub>2</sub>O-EG and LiCl/H<sub>2</sub>O-EG-SNPs at different temperatures are shown in Table 4.4. The densities of LiCl/H<sub>2</sub>O-EG and LiCl/H<sub>2</sub>O-EG-SNPs lie within the range of 1.24~1.31g·cm<sup>-3</sup>, which is slightly lower than that of saturated LiCl solution. The density of both solutions reduces as temperature increases. When the temperature is higher than 60°C, the density of LiCl/H<sub>2</sub>O-EG-SNPs decreases slower, which is the dissolution temperature of crystals.

Table 4.4 Density of LiCl/H<sub>2</sub>O-EG and LiCl/H<sub>2</sub>O-EG-SNPs

Temperature/	25.0	30.0	35.0	40.0	45.0	50.0	55.0	60.0	65.0	70.0	75.0	80.0	85.0
°C													
Saturated													
LiCl solution/	1.301	1.305	1.309	1.314	1.319	1.324	1.330	1.336	1.342	1.349	1.357	1.366	1.376
g·cm <sup>-3</sup>													
LiCl/H <sub>2</sub> O-	1 202	1.206	1 205	1 205	1 200	1.076	1 072	1 071	1.260	1.260	1.266	1.062	1.250
EG/ g·cm <sup>-3</sup>	1.292	1.286	1.285	1.285	1.280	1.276	1.273	1.271	1.269	1.269	1.266	1.263	1.259
LiCl/H <sub>2</sub> O-													
EG-SNPs/	1.308	1.300	1.291	1.287	1.273	1.266	1.258	1.253	1.251	1.250	1.249	1.247	1.245
g·cm <sup>-3</sup>													

The volumetric ESD of three solutions are calculated by the gravimetric ESD in Table 4.5 times the densities at  $T_{\rm amb}$  in Table 4.3. The results are listed in.

Table 4.5 Volumetric ESD absorption TES using conventional and modified solutions

	Volumetric heat storage	Volumetric cold storage
	density (kJ·m <sup>-3</sup> )	density (kJ·m <sup>-3</sup> )
Conventional LiCl solution	7.025×10 <sup>5</sup>	2.186×10 <sup>5</sup>
Modified LiCl/H <sub>2</sub> O-EG solution	7.416×10 <sup>5</sup>	3.786×10 <sup>5</sup>

Figure 4.10 (a) and (b) show the relationship between temperature, shear rate and the apparent viscosity of LiCl/H<sub>2</sub>O-EG and LiCl/H<sub>2</sub>O-EG-SNPs. For both solutions, the apparent viscosity has a roughly linear relation with the shear rate, showing a shear thickening characteristic as commonly seen in fluids with suspension particles (Youssef et al., 2013). The apparent viscosity increases with the decrease in temperature. LiCl/H<sub>2</sub>O-EG-SNPs has a much higher apparent viscosity than LiCl/H<sub>2</sub>O-EG, which is caused by the suspended LiCl crystals in LiCl/H<sub>2</sub>O-EG-SNPs. However, the apparent viscosity of both modified solutions is smaller than that of ice slurry with only 0.09% of ice phase volume at -18°C, indicating a good fluidity (Stokes et al., 2005). Besides, as shown in Figure 4.10 (b), the slopes of the curves at temperatures lower than 65°C are larger than those at 65°C, 75°C and 85°C. This is due to the dissolution of LiCl crystals in LiCl/H<sub>2</sub>O-EG-SNPs at around 60°C.

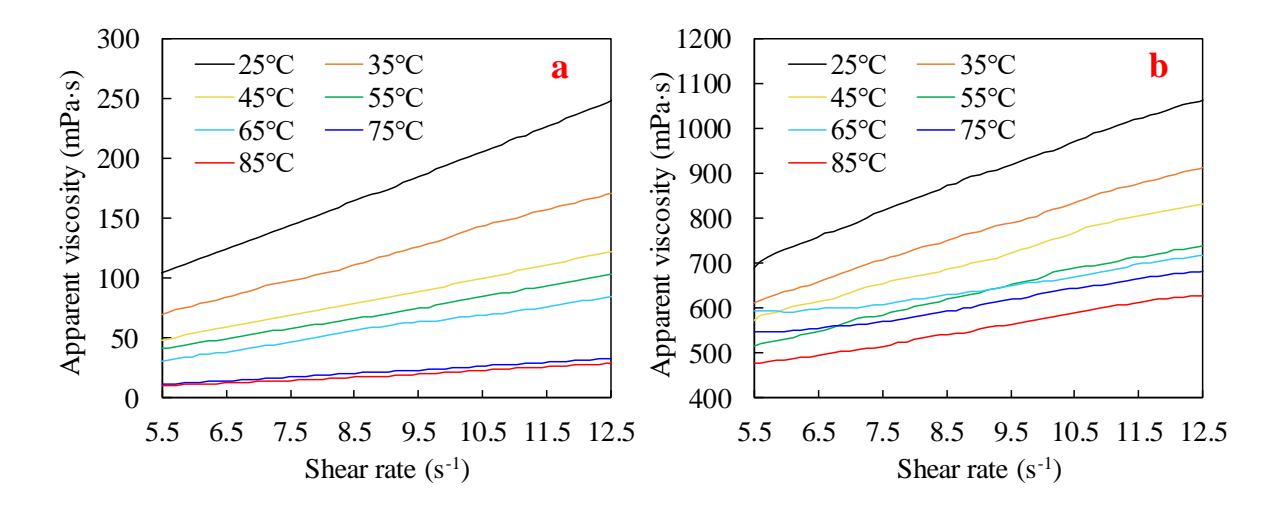


Figure 4.10 Viscosity of LiCl/H<sub>2</sub>O-EG and LiCl/H<sub>2</sub>O-EG-SNPs at different temperatures: (a) LiCl/H<sub>2</sub>O-EG, (b) LiCl/H<sub>2</sub>O-EG-SNPs

The stability of the proposed working fluids was evaluated by analyzing their suspension, thermal, and physical properties over time. All samples were stored in isolation from the

ambient environment after preparation. The thermal and physical properties showed no significant changes even after one year. Regarding suspension properties, the fine crystals in the proposed LiCl/H2O-EG-SNPs solution remained stably suspended for nearly six months. After this period, although some crystals settled at the bottom, they could be easily resuspended with simple stirring, demonstrating the solution's long-term stability.

## 4.2.3 Energy storage density of the working fluids

Solubility measurements of LiCl/H<sub>2</sub>O-EG solution show that the optimal mass ratio of LiCl solution: EG is 50:10, with a corresponding solubility of around 48% at 25°C. The suspension and crystal size measurement of LiCl/H<sub>2</sub>O-EG-SNPs proves that SNPs can further increase the concentration difference by enabling fine LiCl crystals to suspend at a concentration of 53%, which is higher than the solubility at 25°C. The optimal mass ratio of LiCl solution: EG: SNPs is found to be 50:8.5:1.5. The LiCl concentration and the mass ratio of LiCl solution to additives used in DSC measurement follow the optimal mass ratio and concentration. The DSC measurement results are then used to calculate the heat and cold ESD.

The working conditions of the absorption TES using LiCl/H<sub>2</sub>O-EG-SNPs are the same as shown in Table 4.1. Table 4.6 shows the results of ESD values of absorption TES using conventional LiCl solution and two modified LiCl solutions by DSC and theoretical calculation, respectively. The ESD values from DSC measurement results agree with the theoretical ESD. LiCl/H<sub>2</sub>O-EG increases heat and cold storage density by 6.3% and 74.4% compared with the conventional LiCl solution without modification. LiCl/H<sub>2</sub>O-EG-SNPs increases the heat and cold storage density by 24.8% and 156.0% compared with the conventional LiCl solution without modification. LiCl/H<sub>2</sub>O-EG-SNPs outperforms in the three fluids due to its highest ESD.

Table 4.6 ESD comparison of absorption TES using conventional and modified solutions

	Heat storage			Cold storage				
	Concentration	ESD from	Theoretical	Concentration	ESD from	Theoretical		
	range	DSC test	ESD (kJ·kg	range	DSC test	ESD (kJ·kg		
		(kJ·kg mixed	mixed		(kJ·kg mixed	mixed		
		solution <sup>-1</sup> )	solution <sup>-1</sup> )		solution <sup>-1</sup> )	solution <sup>-1</sup> )		
Conventional	35-44%	540 (-)	535	41-44%	168 (-)	173		
LiCl solution								
Modified	35-48%	574 (6.3%)	591	41-48%	293 (74.4%)	288		
LiCl/H <sub>2</sub> O-EG								
solution								
Modified	35-53%	674 (24.8%)	696	41-53%	430 (156.0%)	421		
LiCl/H <sub>2</sub> O-EG	-							
SNPs solution	1							

# 4.3 Summary

This chapter proposes a novel modified LiCl solution for three-phase absorption thermal energy storage to enhance energy storage density while maintaining good fluidity. EG and SNPs are chosen as additives to modify the properties of the LiCl solution and their optimal mass ratios are determined by experimental study. EG increases the solubility of LiCl which expands the working concentration difference and hence increases the ESD. SNPs provide nucleation sites for heterogeneous crystallization, which contributes to the good fluidity of the solution with fine crystals. It further enhances the ESD as the modified solution can work under an even higher concentration compared with adding EG only. The concentration after charging can be enhanced from 44% to 48% by adding EG and to 53% by adding both EG and SNPs.

The effects of additives are evaluated by examining the ESD and the thermal and physical properties of the conventional LiCl solution without additives and the modified LiCl solutions, i.e. LiCl/H<sub>2</sub>O-EG and LiCl/H<sub>2</sub>O-EG-SNPs. The two additives with the opposite mechanism bring even higher ESD. The optimal mass ratio of LiCl solution to EG is 50:10, with which the heat and cold storage density are increased by 6.3% and 74.4% respectively, compared with the conventional LiCl solution without additives. The optimal mass ratio of LiCl solution: EG: SNPs is 50:8.5:1.5. SNPs increase heat and cold storage density by 24.8% and 156.0% respectively. The vapor pressure, viscosity and density of LiCl/H<sub>2</sub>O-EG and LiCl/H<sub>2</sub>O-EG-SNPs are measured and provided in this study. The two modified solutions have lower vapor pressure and density. The lower vapor pressure is beneficial to the discharging process. The viscosity of LiCl/H<sub>2</sub>O-EG-SNPs is quite high but still smaller than the ice slurry.

In general, the proposed novel working fluid has advantages of high ESD, which can help reduce the system volume. Besides, the use of additives reduces the crystallization risks of concentrated solutions and provides new ideas for crystallization control. However, the higher viscosity of novel fluids may bring new challenges in heat and mass transfer. The overall performance of modified solutions is not experimentally investigated. The next chapter will focus on the experimental investigation of the two-phase absorption TES using the novel modified solution.

# Chapter 5 Modeling and Experimental Studies on Two-phase Absorption TES

# 5.1 Description of Two-Phase Absorption TES Processes

The working principle of absorption TES is categorized into three processes: the charging process, the storage process, and the discharging process. During the charging process, diluted solution is pumped into the generator and charged into concentrated solution by external heat source. This process elevates the temperature of the solution and desorbs the water vapor. The vapor is then transferred to the condenser where it is condensed into refrigerant water and subsequently collected and stored in a water tank. In the storage process, the concentrated solution and refrigerant water are separately stored in their respective storage tanks. The temperatures of the solution and water gradually decrease to ambient levels. There is no internal heat and mass transfer between the solution and refrigerant water during this phase. In the discharging process, the stored refrigerant water evaporates in the evaporator under a high vacuum degree, producing a cooling effect. The water vapor is then transported and absorbed by the concentrated solution, generating a heating effect and diluting the solution.

In this chapter, LiCl solution was selected as the working fluid due to its potential for the highest ESD among commonly used water-based working fluids, including LiCl solution, LiBr solution and CaCl<sub>2</sub> solution (Yu et al., 2014). LiCl solution with a concentration of 38% was used as base working fluid. Ethylene glycol was chosen as an additive to extend the concentration glide based on the analysis from the author's previous work (Lin et al., 2021). Three working fluids with different mass ratios of LiCl solution to EG were used. The mass ratios of LiCl solution to EG were 100:0, 100:2.5 and 100:5. The thermal and physical properties of the modified LiCl solution are also detailed in (Lin et al., 2021).

# **5.2** Experimental Conditions and Operations

In this study, several charging and discharging experiments were conducted. The experimental conditions of these experiments are outlined in Table 5.1. For the charging process, the charging temperature ( $T_{\rm cha}$ ) ranged from 65 to 85°C, reflecting the temperature level of low-grade waste heat. For the discharging process, three discharging modes (i.e. heating, combined heating and cooling, cooling) with different discharging temperatures ( $T_{\rm dis}$ ) were selected for different application scenarios (i.e. domestic hot water supply, heating and precooling, cooling). The ambient temperature was approximately 30°C for the charging experiments and 20°C for the discharging experiments.

The base working fluid used in this study was LiCl solution with a concentration of 38%. EG was added to 38% LiCl solution to expand the concentration glide of the LiCl solution. The mass ratios of LiCl solution to EG are 100:0, 100:2.5 and 100:5.

Table 5.1 Experimental conditions of the charging and discharging experiments

Energy supply and output		Charging/Discharging temperature (°C)	Condensation temperature (°C)	Evaporation temperature (°C)	
Charging	Waste heat	65, 75, 85	30	/	
	Heating	50	/	30	
Discharging	Combined heating and cooling	20 and 40	/	23	
	Cooling	10	/	12	

Before the charging and discharging experiments, the vacuum pump was utilized to extract the non-condensable gases from the test rig. Non-condensable gases significantly impact the desorption, condensation, evaporation and absorption of the water vapor and may cause the corrosion issue. Therefore, it is crucial to maintain a high vacuum level not only during the charging and discharging processes, but also for during non-experimental period. Also, the pH value of the solution is kept within the range of 9-10 to further reduce corrosion.

Prior to the charging process, the solution mass and concentration were adjusted to approximately 115kg and 38%, respectively. The temperatures of both thermostatic water baths were set to the appropriate values corresponding to the working conditions. The cooling water temperature in the water tank was adjusted to the condensation temperature. Then, the hot water and cooling water were pumped into the generator and condenser, respectively. The hot water and cooling water were circulated until the outlet temperature equaled the inlet temperature, indicating that both heat exchangers had reached thermal equilibrium with the heat transfer fluids. After that, the solution pump and water pump were turned on and the charging process began. The charging process will be considered complete and all the devices will be turned off when the solution's liquid level remains unchanged for 5 minutes, indicating the solution has reached an equilibrium state. After the charging process, the solution and water were stored separately in two tanks, and their temperatures gradually decreased to the ambient levels.

Before the discharging process, the temperatures of both thermostatic water baths were adjusted to the appropriate values corresponding to the working conditions. The water temperature in the water tank was adjusted to the evaporation temperature. The heated water and chilled water were then pumped into the generator and condenser, respectively. These fluids were circulated until the outlet temperature equaled the inlet temperature, indicating that both heat exchangers had reached thermal equilibrium with the heat transfer fluids. For the

heating conditions, in particular, the water pump for the heated water was closed until the solution temperature exceeded the discharging temperature. Then, the solution and water pump were turned on and the discharging process began. The discharging process will be considered complete and all the devices will be turned off when the solution's liquid level remains unchanged for 5 minutes, indicating the solution has reached the equilibrium state.

## **5.3** Dynamic Charging Characteristics

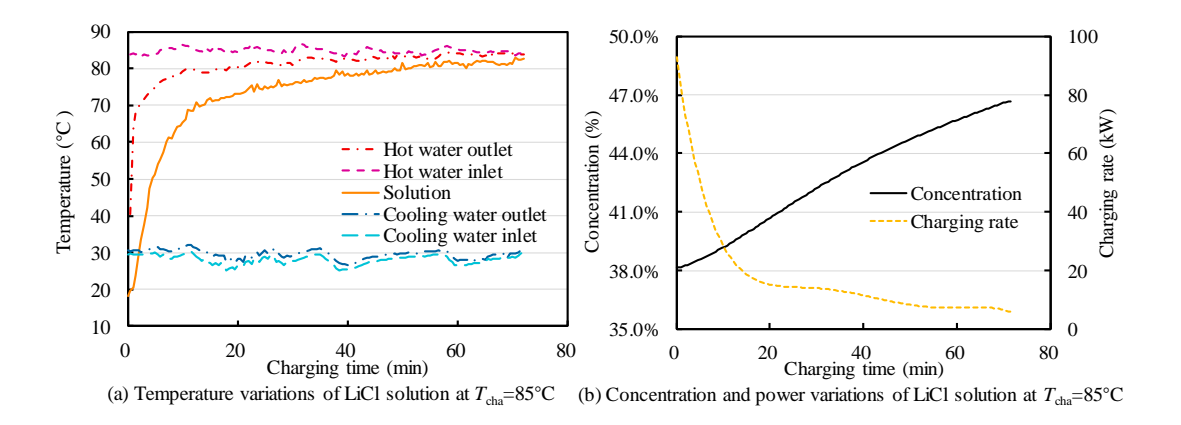
## **5.3.1** Influence of charging temperature

As mentioned above, LiCl solution with different mass ratios of EG were used as working fluids. For the charging process, three different hot water temperatures, 85°C, 75°C and 65°C, were used to simulate solar energy with different levels from solar collectors. Cooling water temperature was maintained at 30°C. The initial concentration of the solution is set around 38%. The influences of the charging temperature and the EG's mass ratio on the charging process were experimentally investigated. Test data were recorded every minute. The charging rate, concentration glide and total charged heat were calculated and compared with the experimental data.

The dynamic charging characteristics of the LiCl solution, including the time-dependent temperature, concentration and charging rate variations under different  $T_{\text{cha}}$  are shown in Figure 5.1. The charging process can be divided into two stages depending on the temperature difference between solution and hot water. In the first stage, a large temperature difference results in a high charging rate. The charged heat is used for both solution sensible heat gain and vapor desorption. Both the solution temperature and concentration rise rapidly. The charging rate decreases as the solution temperature increases. The temperature difference between the hot water inlet and outlet also decreases. When the solution temperature is high, the charging process goes into the second stage. In this stage, the temperature difference

between solution and hot water is small (below 5°C). The charging rate remains approximately constant around a certain value, exhibiting only slight fluctuations, but it gradually decreases slightly over the charging time as the solution concentration increases.. The charged heat is primarily used for vapor desorption. The solution temperature fluctuates and the solution concentration continues to increase.

The vapor desorption rate can be inferred from both the increase in concentration and the temperature difference between the cooling water's inlet and outlet, which results from the vapor condensation in the condenser. It can be seen that when  $T_{\rm cha}$  is 85°C or 75°C, the desorption rate is low in the initial few minutes, then increases as the solution temperature rises rapidly. The charging process terminates when the solution concentration reaches about 46.3%, which is the solubility of LiCl at 30°C. When  $T_{\rm cha}$  is 65°C, the desorption rate remains low during the charging process. The final concentration is only 44.3%, as at lower  $T_{\rm cha}$ , the vapor pressure is lower and gradually drops to the condensation pressure along the charging process. Consequently, less vapor can be desorbed from the solution. It should be noted that at a certain time, the heat for desorption may slightly exceed the charging rate. Since the charging rate is calculated as the sum of the solution enthalpy change and the heat for desorption, fluctuations in temperature can result in a negative value of the enthalpy change, thereby impacting the charging rate.



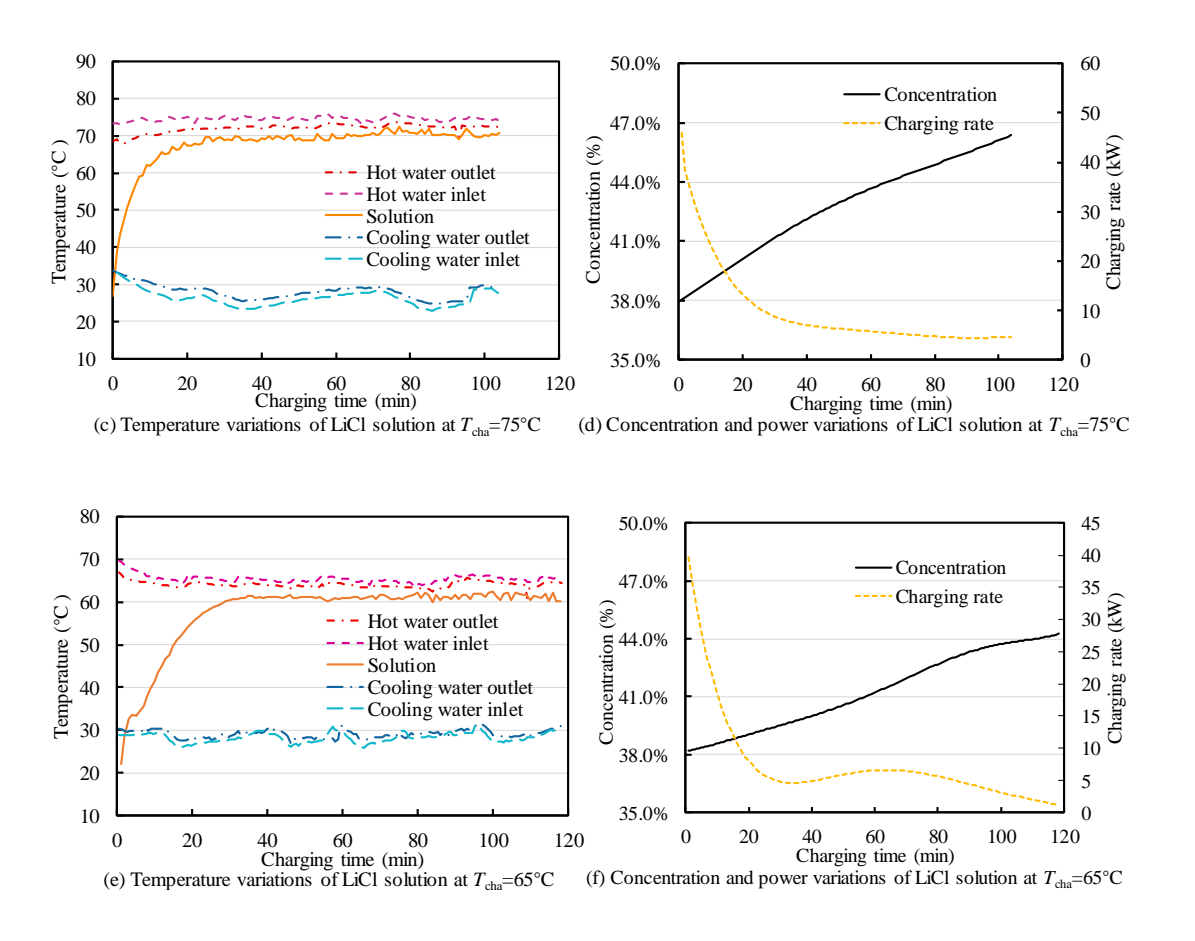


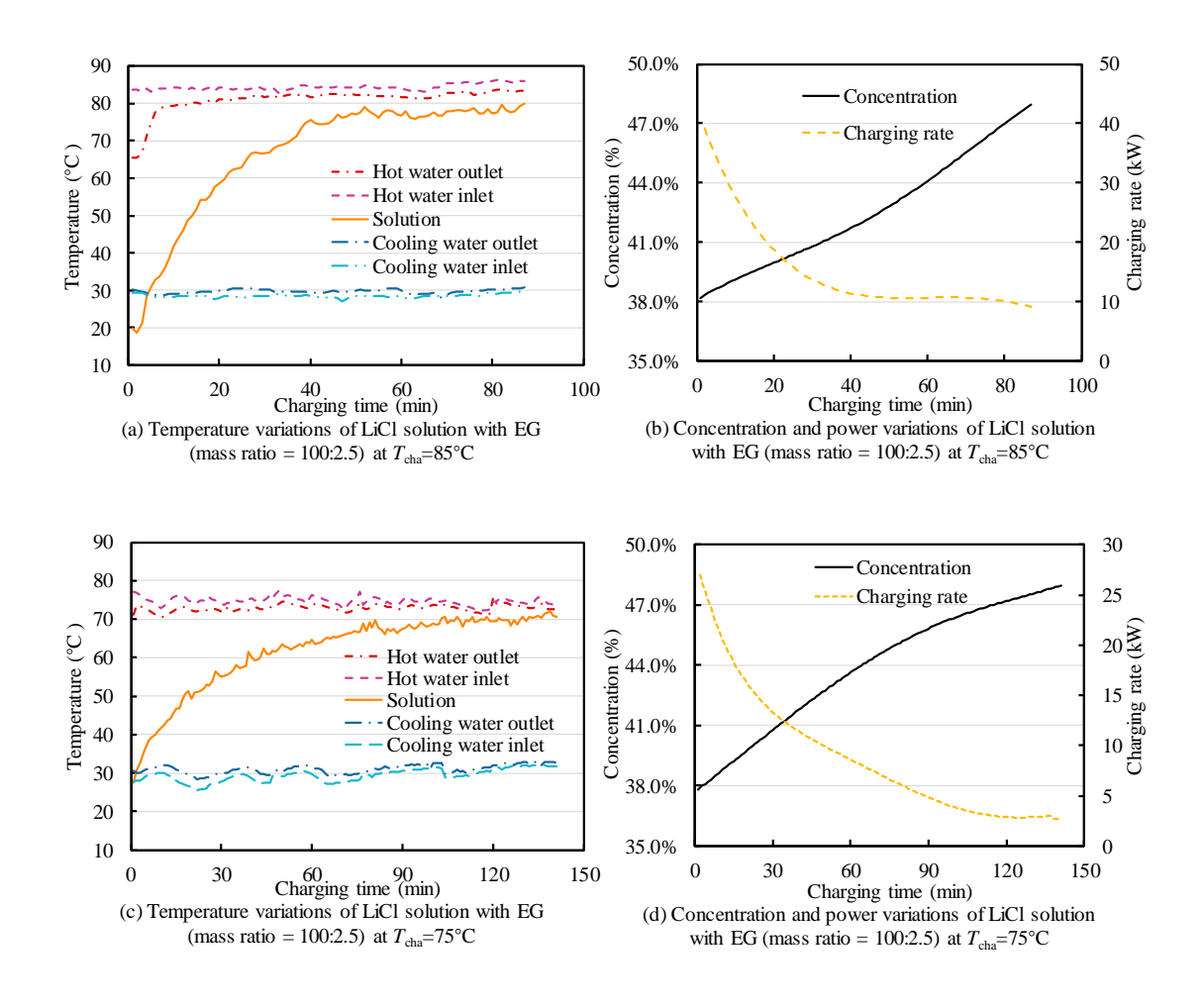
Figure 5.1 Temperature, concentration and charging rate variation of LiCl solution in the charging process (a), (b) 85°C charging; (c), (d) 75°C charging; (e), (f) 65°C charging

### 5.3.2 Influence of additive

Figure 5.2 shows the dynamic charging characteristics of LiCl solution with EG (mass ratio 100:2.5). The variations of temperatures, concentration and charging rate during the charging process show similar trends to that of LiCl solution. In the first stage, the solution temperature gradually increases until approaches the hot water temperature. Compared with the pure LiCl solution, the charging rate is lower due to the lower thermal conductivity of EG. However, the vapor desorption rate is similar to that of the LiCl solution, indicating that the introduction of EG has no significant impact on the solution's pressure. In the second stage, the solution temperature is close to  $T_{cha}$  and the charging rate stays constant. Both the charging rate and

vapor desorption rate are close to that of the LiCl solution under the same  $T_{\rm cha}$  as the charged heat is primarily used for vapor desorption.

When  $T_{\text{cha}}$  is 85°C or 75°C, the charging time the wide channels in the heat exchangers facilitate high mass transfer rates with small pressure drops under high vacuum working conditions is longer due to the larger concentration glide. The final concentration is the solubility of working fluid measured at 30°C. When  $T_{\text{cha}}$  is 65°C, the final concentration is almost identical to that of LiCl solution, further proving that the introduction of EG has no significant impact on the solution's vapor desorption.



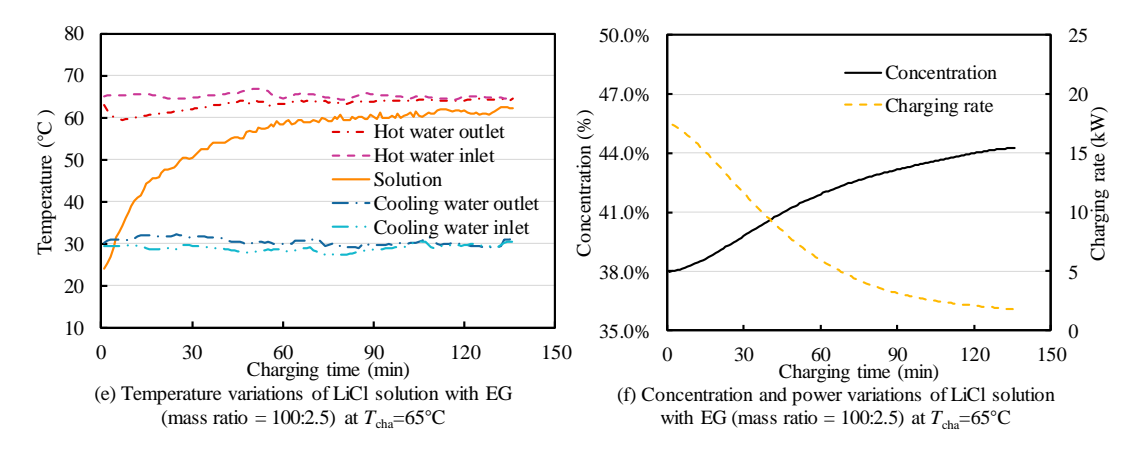
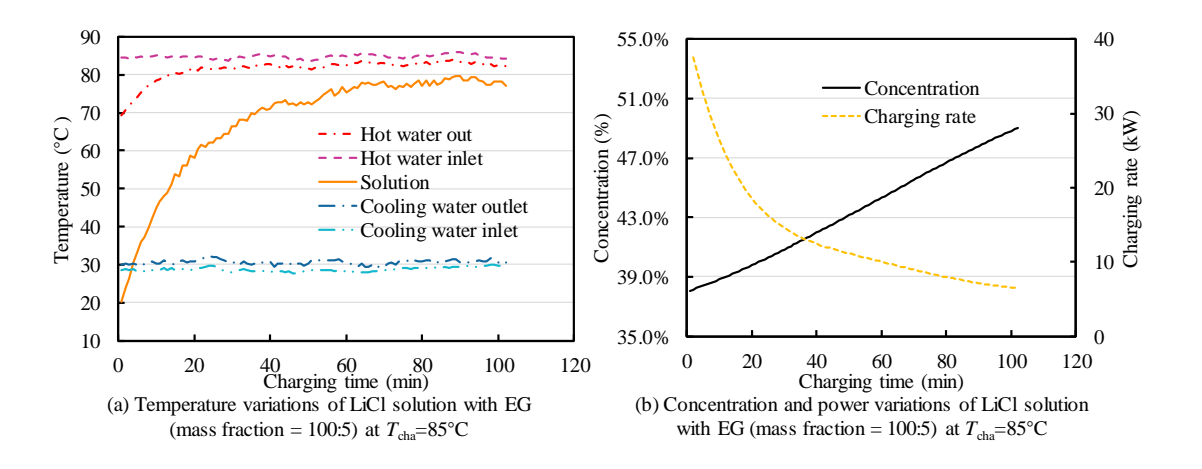


Figure 5.2 Temperature, concentration and charging rate variation of LiCl solution + EG (mass ratio 100:2.5) in charging process (a), (b) 85°C charging; (c), (d) 75°C charging; (e), (f) 65°C charging

Figure 5.3 presents the dynamic charging characteristics of LiCl solution with EG (mass ratio 100:5). Two stages can also be observed during the charging process. The first stage takes a longer time under the same charging temperature. The charging rate is lower than that of LiCl with 2.5% EG, but the desorption rate is unaffected. In the second stage, when  $T_{\rm cha}$  is 75°C and 85°C, the charging rate and desorption rate are slightly lower than the previous two working fluids. This is because the desorption rate decreases with the increase of concentration, especially at a larger concentration glide. When  $T_{\rm cha}$  is 65°C, the concentration glide is even slightly smaller and the charging process takes longer to finish, indicating that the effect of EG is limited at lower  $T_{\rm cha}$ .



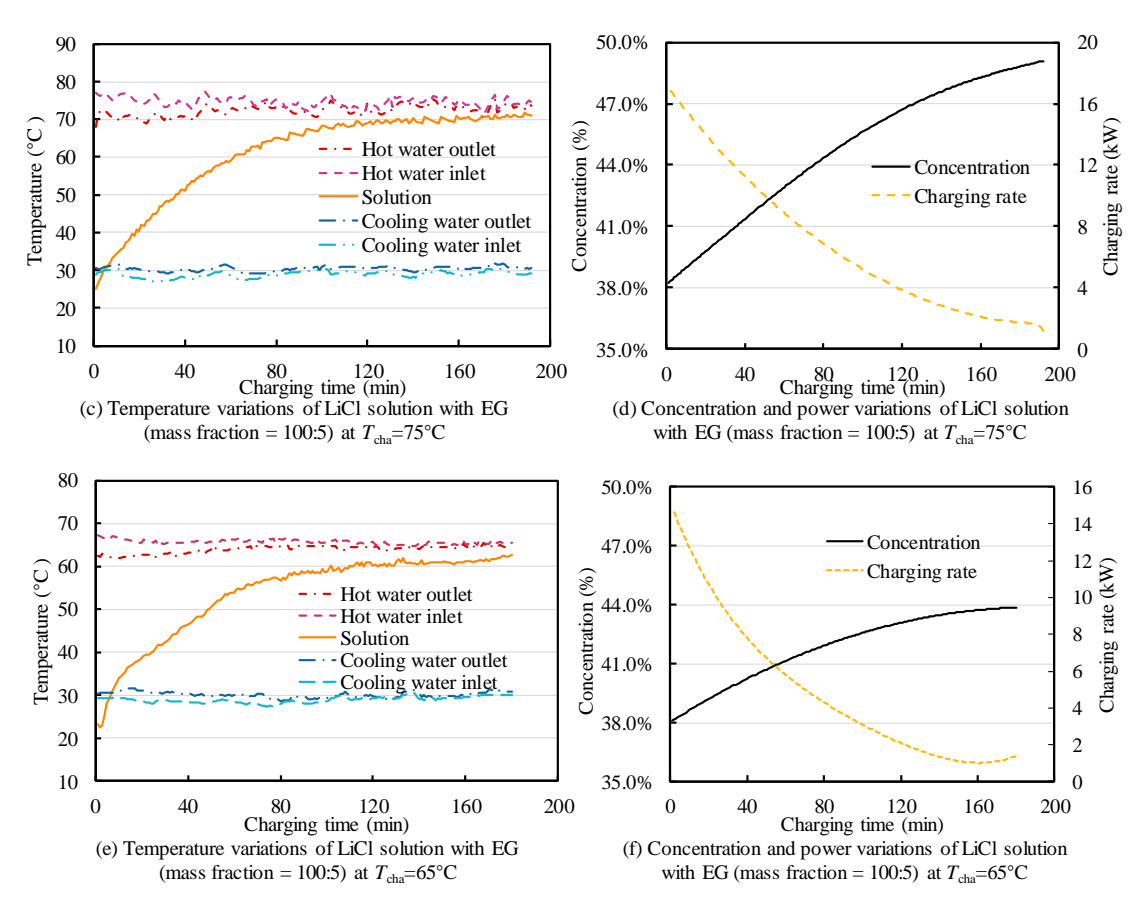


Figure 5.3 Temperature, concentration and charging rate variation of LiCl solution + EG (mass ratio 100:5) in charging process (a), (b) 85°C charging; (c), (d) 75°C charging; (e), (f) 65°C charging

# 5.4 Dynamic Discharging Characteristics

## **5.4.1** Influence of evaporation temperature

In the discharging process, the experimental conditions are chosen based on three discharging modes, heating output, cooling output and combined heating and cooling output. The impact of the additive's mass ratio and evaporation temperature on discharging characteristics was investigated. The discharging temperatures and evaporation temperatures of three experimental conditions have been listed in Table 2. The discharging process was terminated either when the discharging temperature failed to meet the experimental condition or when the solution's liquid level remained constant for 5 minutes. The dynamic discharging

characteristics were recorded throughout the experiments. After that, the ESD is calculated and compared based on the dynamic discharging characteristics.

Figure 5.4 shows the dynamic discharging characteristics of the LiCl solution. The discharging process was found to be more prolonged than the charging process. For the heating mode, the discharging process can also be divided into two stages. The first stage takes 12 minutes, during which the solution temperature is lower than  $T_{dis,h}$  (50°C). No heated water is pumped into the heat exchanger, resulting in no discharging heat. A large amount of refrigerant water evaporates from the evaporator due to a large pressure difference. The solution absorbs the evaporated water and gets heated up rapidly. In the second stage, heated water is pumped into the heat exchanger once the solution temperature exceeds  $T_{\rm dis,h}$ . The discharging heat is then taken away by the heated water. The discharging rate is relatively stable until the solution temperature falls below  $T_{\text{dis,h}}$ . It can also be seen that the absorption rate in the second stage is comparable to that in the first stage. In this stage, the discharging rate is highly dependent on the absorption rate (i.e. mass transfer), which is associated with the evaporation temperature, solution temperature and concentration. Therefore,  $T_{\text{dis,h}}$  and discharging rate can be manipulated by adjusting the evaporation temperature. In this experiment, the temperature of the heated water is reduced twice in the 70<sup>th</sup> and 90<sup>th</sup> minutes to keep the discharging rate at a relatively higher level. The solution temperature increases from 26.7°C and its maximum temperature exceeds 55°C. The  $T_{\rm dis,h}$  reaches 53°C at a  $T_{\rm eva}$  of 30°C. Such a high temperature lift is beneficial for real applications. Given that a  $T_{\text{eva}}$  of 30°C is the highest among the three discharging modes, the concentration glide is also the largest.

For the combined heating and cooling mode, two stages can also be found in the discharging process. The total discharging time is similar to that of the heating mode while the first stage is more prolonged. In the first stage, there's no heating output due to the low solution

temperature. The cold discharging rate is the highest at the beginning of the discharging process due to a large pressure difference. The first stage takes 25 minutes, which is longer than in the heating application since  $T_{\rm eva}$  is lower. In the second stage, heated water is pumped into the heat exchanger, and the solution temperature gradually decreases over time. The heat discharging rate is initially higher than the cold discharging rate. The potential reason is that the evaporated water producing a cooling effect may not be immediately absorbed by the solution, but instead accumulates in the evaporator and is transported into the absorber before being absorbed by the solution. Therefore, the heat and cold discharging rates may not always align. The heat and cold discharging rates are close to the phase change heat of refrigerant water. Since evaporation temperature and heat discharging temperature are closely linked, it's difficult to achieve high heating output and low cooling output temperature simultaneously. The maximum solution temperature is 45°C at a  $T_{\rm eva}$  of 20°C. Furthermore, the heat and cold discharging rate are lower than the heat discharging rate in the heating mode, and the concentration glide is also smaller.

For the cooling mode, no distinct two stages are evident during the discharging process. As only cooling output is required, the solution temperature can be maintained at a lower level, thereby keeping the solution vapor pressure low. This allows for the discharging process at a lower evaporation temperature. As the discharging process progresses, the solution's concentration drops, and its vapor pressure increases, the refrigerant temperature also needs to increase to continue the discharging process. The maximum discharging rate occurs at around 60 min but not at the beginning of the discharging process. This may be due to the solution pressure decreasing during the first 60 minutes. As the discharging rate is heavily dependent on mass transfer, a lower solution temperature facilitates a higher mass transfer rate. The discharging process ends when the discharging rate falls to 0, and the refrigerant temperature

exceeds 12°C. The concentration glide and discharging rate are comparable to the previous two experimental conditions.

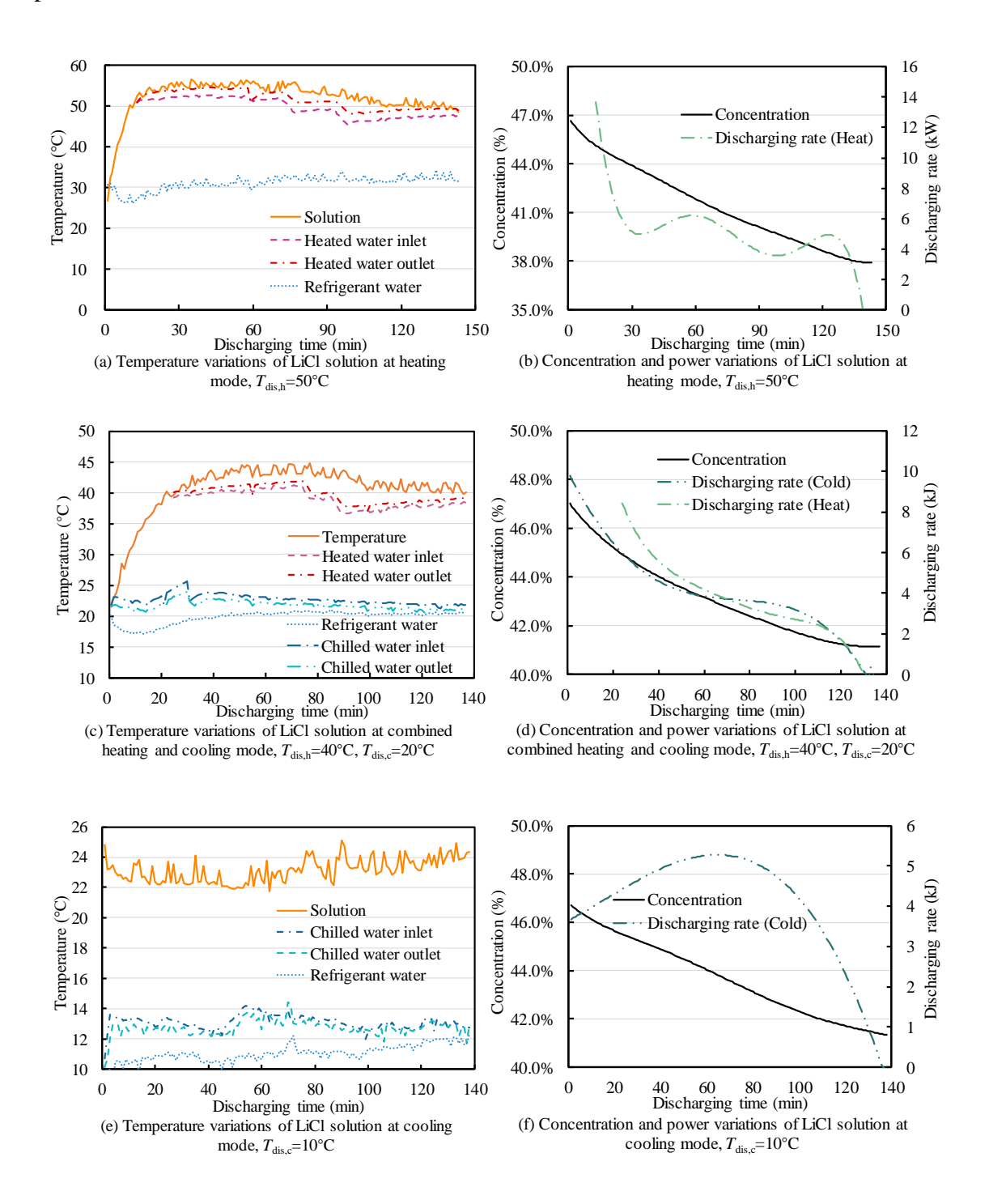
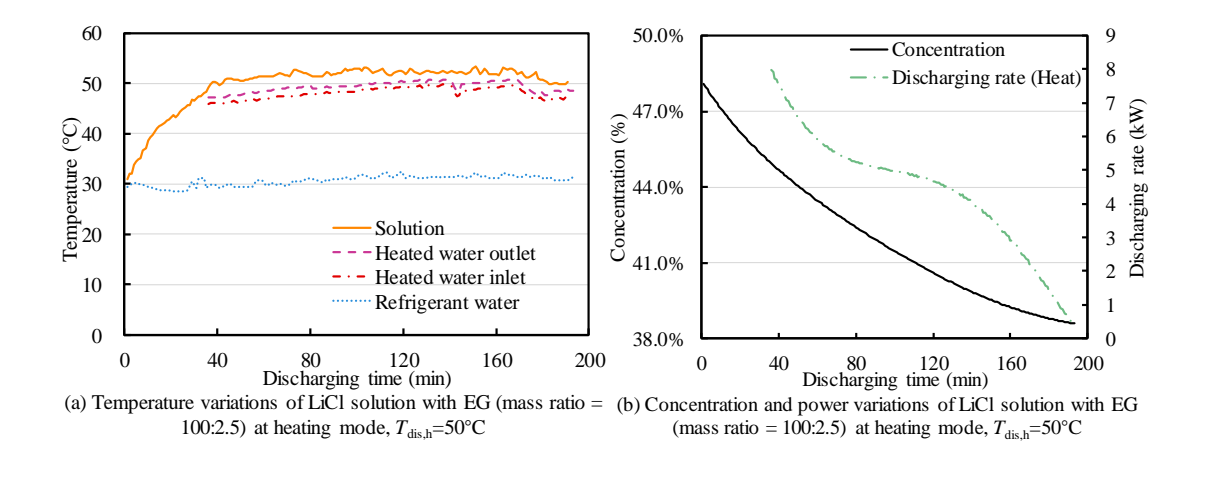


Figure 5.4 Temperature, concentration and charging rate variation of LiCl in discharging process (a), (b) 50°C heating; (c), (d) combined 40°C heating and 20°C cooling; (e), (f) 10°C cooling

#### **5.4.2** Influence of additive

Figure 5.5 presents the dynamic discharging characteristics of LiCl solution with EG (mass ratio 100:2.5). Similar to the previous results, two stages can also be found in both the heating mode and the combined heating and cooling mode. However, compared with the result of the LiCl solution, both stages are more prolonged. This can be attributed to two factors: 1) the introduction of EG extends the concentration glide, allowing more water vapor to be absorbed by the solution during discharging, and 2) EG reduces the solution's thermal conductivity. However, it can be observed that the absorption rate is almost unaffected. The extended discharging time in the first stage of discharging has a more significant impact on heat discharging rather than on cold discharging, suggesting that EG has a smaller impact on mass transfer than on heat transfer. The discharging rates can be maintained above 2kW most of the time during the discharging processes.

For the cooling mode, the temperature conditions are identical to those of the LiCl solution. The maximum cold discharging rate is observed at the beginning of the discharging process and then gradually declines. The introduction of EG appears to have only a minor impact on the discharging process.



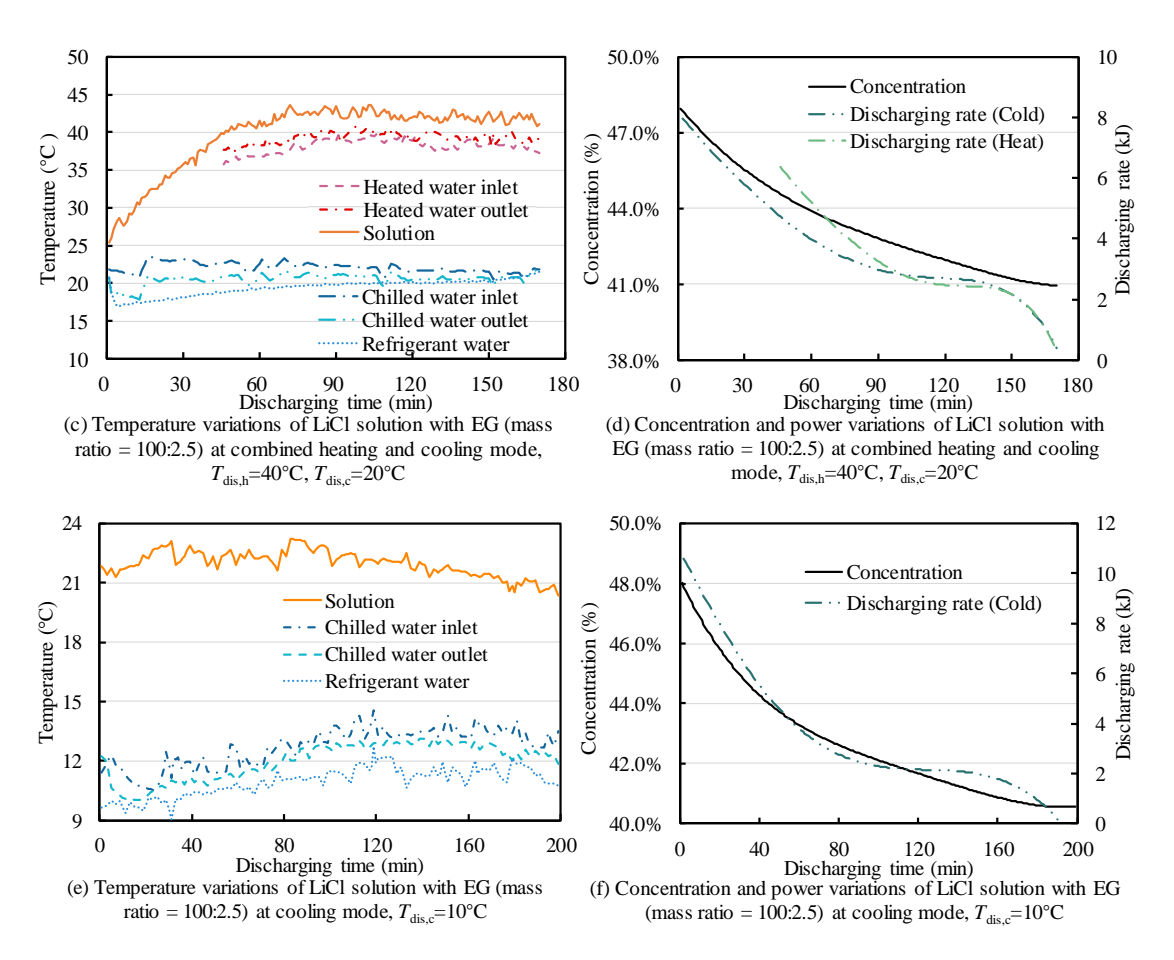


Figure 5.5 Temperature, concentration and charging rate variation of LiCl with EG (mass ratio = 100:2.5) in discharging process (a), (b) 50°C heating; (c), (d) combined 40°C heating and 20°C cooling; (e), (f) 10°C cooling

Figure 5.6 shows the dynamic discharging characteristics of the LiCl solution with EG (mass ratio 100:5). At all experimental conditions, the discharging characteristics, including the temperature variations and discharging rate, follow the same pattern as in previous tests. The major difference is the increase in discharging time, especially for the cooling mode. The prolonged discharging time can also be attributed to the extended concentration glide and reduced thermal conductivity. The discharging rate is also not significantly affected. These results further validate the feasibility of using EG to extend the concentration glide.

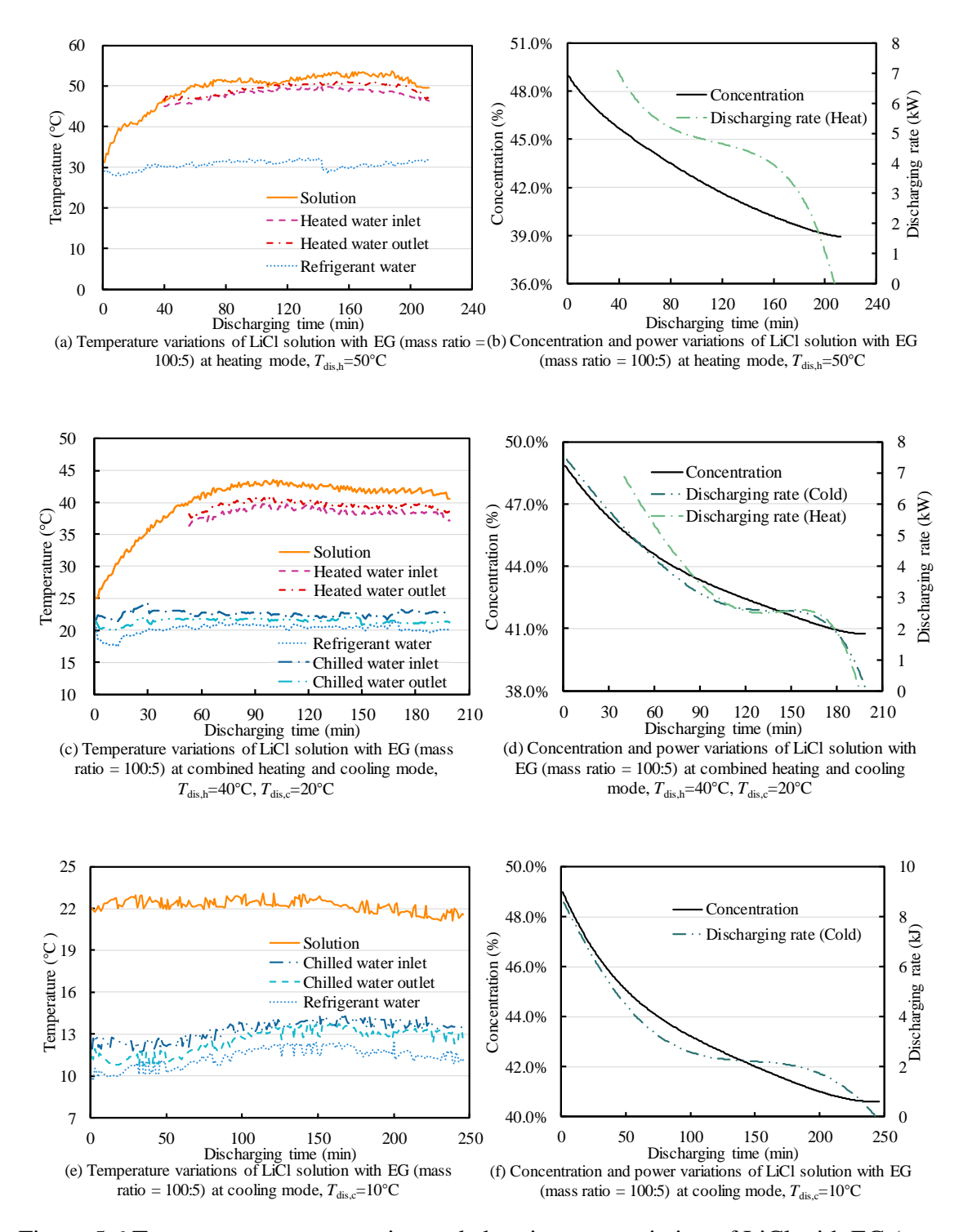


Figure 5.6 Temperature, concentration and charging rate variation of LiCl with EG (mass ratio = 100:5) in discharging process (a), (b) 50°C heating; (c), (d) combined 40°C heating and 20°C cooling; (e), (f) 10°C cooling

Figure 5.7 (a) and (b) present the heat balance analysis results of the experimental test rig under various operating conditions. The heat exchanged by the hot and cold fluids is calculated

and compared, including: the heat input to the solution and heat supplied by the hot water during the charging process; the heat released by the solution and heat gained by the heated fluid in the absorber during discharging; and the heat released by the cooling water and heat absorbed by the refrigerant water in the evaporator during discharging.

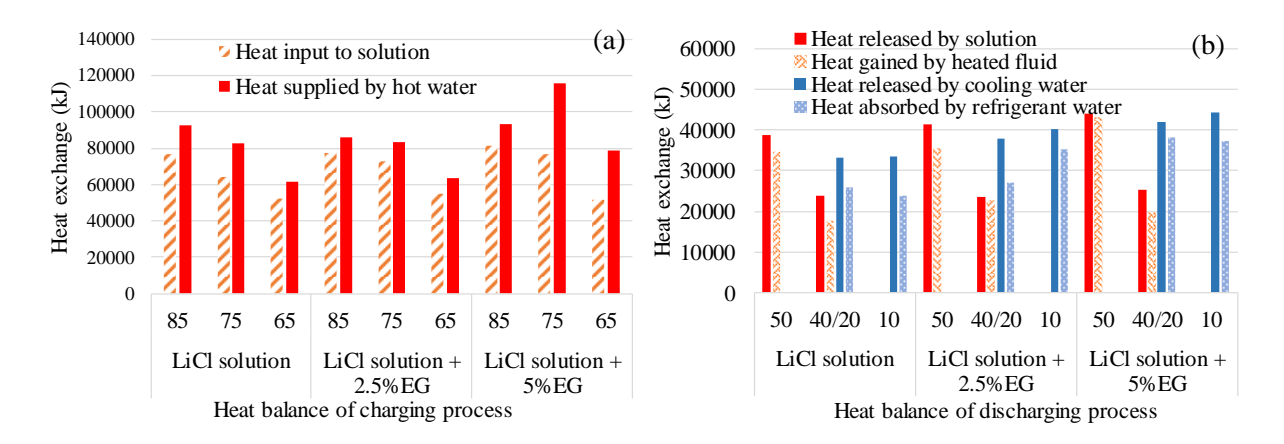


Figure 5.7 Heat balance analysis of charging and discharging experiments

As shown in the bar charts, the heat exchanged by the hot fluids is consistently higher than that absorbed by the cold fluids. This discrepancy is primarily attributed to heat transfer with the metal components of the heat exchanger. During both charging and discharging, the hot fluid exchanges heat not only with the cold fluid but also with the metal structure of the heat exchanger, despite insulation efforts to minimize heat loss to the surroundings.

The average heat transfer efficiency of the system is calculated to be 82.9%, which is considered acceptable given the substantial mass of metal involved (approximately 400 kg per heat exchanger). This analysis highlights the impact of the metal mass on the overall heat balance and provides insight into potential areas for thermal performance improvement.

## **5.5** Energy Storage Performance Analysis

Table 5.2 summarizes the concentration difference, charging time, theoretical  $Q_{\rm cha}$  and experimental  $Q_{\rm cha}$  of three working fluids under different charging temperatures. The effect of

EG on the charging process is shown. According to the theoretical  $Q_{\rm cha}$ , the introduction of EG enhances the concentration glide at higher  $T_{\rm cha}$  (e.g. 75°C and 85°C), thereby increasing the total charged heat. The experimental  $Q_{\rm cha}$  is the actual heat input from hot water. The discrepancy between theoretical and experimental results primarily arises from heat loss. The heat is greater when the charging time is longer. At a lower  $T_{\rm cha}$  (e.g. 65°C), the concentration differences are smaller compared with that of higher  $T_{\rm cha}$ . This is due to the smaller difference between the solution's vapor pressure and condensation pressure. Besides, EG also reduces the solution's vapor pressure. The total charged heat of the three working fluids is almost identical regardless of the increase in EG's mass ratio concentration. Furthermore, the addition of EG to the solution results in a longer charging time, particularly during the first stage. The longer charging time is primarily attributed to a larger concentration glide and lower thermal conductivity. The maximum amount of relative uncertainty of the experimental  $Q_{\rm cha}$  is calculated through uncertainty propagation. The average value is 10.6%.

Table 5.2 Summary of the charging process

Working flu	ids	LiCl solution			LiCl solution + 2.5%EG			LiCl solution + 5%EG		
Charging		85	75	65	85	75	65	85	75	65
temperature	(°C)									
Concentration	on	38.1-	37.9-	37.7-	38.2-	37.8-	38.0-	38.1-	38.3-	38.1-
glide (%)		46.8	46.4	44.3	48.0	48.0	44.3	49.0	49.1	43.9
Charging	time	72	104	119	87	141	136	102	192	180
(mins)	time	12	104	117	07	141	130	102	1)2	100
Theoretical	$Q_{cha}$	75717	63957	52342	76964	73082	54771	80744	76685	51397
(kJ)										

Experimental $Q_{cha}$	92924	82941	61230	86043	83278	63435	93318	115444	78688
(kJ)	±	±	±	±	±	土	土	±	土
	5742	7922	11545	6350	9803	8147	6562	11038	9803

Table 5.3 summarizes the results of the discharging experiments. The concentration glide, discharging time, theoretical  $Q_{\rm dis}$  and experimental  $Q_{\rm dis}$  are calculated and summarized. Theoretical  $Q_{\rm dis}$  reveals the maximum potential discharged heat or cold can be obtained without considering heat loss. Experimental  $Q_{\rm dis}$  is the actual discharged heat or cold. The ESD values are calculated using the experimental  $Q_{\rm dis}$ .

The maximum gravimetric ESD at heating mode, cooling mode and combined heating and cooling mode are 357 kJ/kg solution, 310 kJ/kg solution, and 437 kJ/kg solution, which are 123 kWh/m³, 108 kWh/m³ and 177 kWh/m³ in volumetric ESD, respectively. Here, the ESD of the combined heating and cooling mode is the sum of ESD<sub>c</sub> and ESD<sub>h</sub>. The maximum ESD values are all achieved using LiCl solution with EG (mass ratio = 100:5). The enhancements compared with that of LiCl solution are 18%, 18% and 61%, respectively. Their concentration glides are 49.0%-38.9%, 48.9%-40.8% and 49.0%-40.6%, respectively. However, a larger concentration glide also requires a longer discharging time. Especially for the heating mode, since the time at the first stage of discharging is also prolonged, the enhancement of ESD<sub>h</sub> is less significant. For the combined heating and cooling mode, only part of the heat produced during the discharging process is utilized, therefore the ESD<sub>h</sub> is lower than ESD<sub>c</sub>. In comparison to the existing experimental studies, the proposed working fluids demonstrated the highest ESD. Moreover, the proposed heat exchanger achieved efficient heat and mass transfer, with the solution's temperature lift approaches the theoretical limit.

Table 5.3 Summary of the discharging process

Working fluids	LiCl so	lution		LiCl	solution	+ EG	LiCl	solution	+ EG
				(100:2.	5)		(100:5)		
T <sub>dis</sub> (°C)	50	40/20	10	50	40/20	10	50	40/20	10
Concentration glide (%)	46.7-	47.0-	46.7-	48.1-	48.0-	48.0-	49.0-	48.9-	49.0-
	37.9	41.2	41.3	38.6	41.0	40.6	38.9	40.8	40.6
Discharging time (mins)	143	137	138	193	170	199	212	199	247
Theoretical $Q_{dis,h}$ (kJ)	38795	23701	/	41485	23505	/	43999	25373	/
Experimental $Q_{\text{dis,h}}$ (kJ)	34712	17811	/	35424	22702	/	43122	19859	/
	±4686	±9411		±7158	±4466		±7854	±5358	
Theoretical $Q_{\rm dis,c}$ (kJ)	/	33162	33527	/	37863	40315	/	42089	44310
Experimental $Q_{\text{dis,c}}$ (kJ)	/	25945	23920	/	27162	35363	/	38305	37390
		±11995	±12913		±4344	±10835		±7720	±10363
ESD <sub>g,h</sub> (kJ/kg solution)	302	155	/	300	192	/	357	164	/
ESD <sub>g,c</sub> (kJ/kg solution)	/	216	193	/	310	300	/	273	310
$ESD_{vol,h}$ ( $kWh/m^3$ )	103	43	/	102	50	/	123	66	/
$ESD_{vol,c}$ (kWh/m <sup>3</sup> )	/	78	73	/	80	106	/	111	108

# 5.6 Key Factors Influencing Charging and Discharging Processes

In general, the charging and discharging processes are experimentally studied. All the design working conditions are realized. The following discussions focus on the key factors that have impacts on the charging and discharging processes of the absorption TES system.

First of all, working fluids play a fundamental and crucial role in the absorption TES system. The concentration glide has a significant impact on the ESD. Efficient heat and mass transfer are important to realize the charging and discharging processes of the absorption TES cycle. Additives influence the heat and mass transfer by altering the properties of the solution, including the solubility and vapor pressure. Therefore, when selecting the working fluids or additives, the overall impact on the absorption TES system needs to be considered. In this work, EG extended the concentration glide by acting as a crystallization inhibitor, thereby increasing the solubility of LiCl. A larger concentration difference in the LiCl solution leads to a higher ESD. However, EG may affect the charging and discharging rates, which needs future study.

Temperature conditions determine the concentration glide of a particular working fluid in both the charging and discharging processes. Specifically, the concentration after charging (if neglects the crystallization issue) is determined by the condensation temperature and charging temperature. Similarly, the concentration after discharging is determined by the evaporation temperature and discharging temperature. Therefore, the temperature conditions need to be carefully chosen and controlled before and during the operation to achieve a high ESD.

The pressure difference between the solution and refrigerant water governs the mass transfer during the charging and discharging processes. Compared with the charging process, the discharging process is more sensitive to temperature variations due to the smaller pressure difference. Therefore, the control of the temperatures is essential for stable operation.

Moreover, heat exchangers also significantly impact the charging and discharging processes. Large heat transfer areas, good wetting conditions and small pressure drop are all crucial for efficient heat and mass transfer. In this research, the wide channels in the heat exchangers facilitate high mass transfer rates with small pressure drops under high vacuum working conditions. The liquid distributor ensures good wetting performance. Therefore, a high

 $T_{\rm dis}$  with large temperature lift and high discharging rate at the given evaporation temperature can be realized. However, the adoption of the wide channel in heat exchangers compromises compactness and heat transfer efficiency, resulting in a higher heat input from hot water compared to solution heat gains, especially at higher  $T_{\rm cha}$ . Similarly, the experimental discharging heat is also lower than the theoretical values.

Besides, several other factors, including measurement uncertainties, heat loss, and the presence of non-condensable gas, could also affect experimental accuracy. Although efforts were made in this study to minimize these impacts, complete elimination was unattainable.

# 5.7 Summary

Absorption TES has gained increasing attention in recent years. On one side, its high ESD stands out compared with sensible and latent TES. Besides, it has the advantages of negligible heat loss, high flexibility, low charging temperature, etc. The ESD can be further enhanced by extending the concentration glide. Previous studies have revealed the potential of using EG as an additive to extend the concentration glide. On the other side, its heat and mass transfer, vacuum, and crystallization issues are several challenges that need to be addressed. Moreover, the potential of additives has never been experimentally tested on a real absorption TES system.

To address these issues, a closed absorption TES system for multiple application scenarios is established. A novel-designed heat exchanger is used for the generator/absorber and condenser/evaporator. LiCl solution and LiCl solutions with EG were used as the working fluids. The performances of the working fluids were tested through charging and discharging experiments under different working conditions. The charging and discharging characteristics were revealed based on the experiment data. The main conclusions are drawn as follows:

- (1) The feasibility of using EG as an additive was proved. Charging at different temperatures and discharging with different temperature outputs were achieved. In the charging process, the charging rate varies significantly, starting off high and gradually decreasing as the concentration increases. A higher charging temperature (75°C or 85°C) was preferred for a larger concentration difference. The concentration differences were around 8.6% for the LiCl solution, 9.5% for the LiCl solution + 2.5% EG, and 10.8% for the LiCl solution + 5% EG. However, when the charging temperature is 65°C, the solution can not be fully charged due to the low vapor pressure difference.
- (2) During the discharging process, the discharging rate also changes over time. However, in all application scenarios, a discharging rate exceeding 2kW can be maintained for most of the duration. The temperature lift is close to the maximum value, indicating the effective heat and mass transfer of the novel-designed heat exchanger. EG enhanced the ESD by extending the concentration glide. LiCl solution + 5% EG has the highest ESD values, which are 123 kWh/m³, 177 kWh/m³, 108 kWh/m³ for the heating mode, combined heating and cooling mode, and cooling mode, respectively. The enhancements led by EG are 18%, 46% and 48%, respectively. The experimental ESD values obtained in this study are also the highest, compared to previous studies on closed absorption TES. The theoretical ESD can be even higher if the heat loss is neglected.

In summary, the modified working fluids with EG have proven to extend the concentration glide and enhance ESD. There remain opportunities to further explore other candidate crystallization inhibitors as additives with better thermal conductivity and to develop efficient heat exchangers with better compactness.

# Chapter 6 Experimental Studies and Dynamic Modeling on Three-phase Absorption TES

## **6.1** Description of the Three-Phase Process

The operating principle of the closed three-phase absorption TES is illustrated in Figure 6.1 (a-c). The system consists of four major parts: one generator/absorber for solution generation and absorption, one condenser/evaporator for water vapor condensation and evaporation, a storage tank for solution storage and a water tank for refrigerant water storage. The operation of three-phase absorption TES includes three processes, charging, storage and discharging processes. During the charging process, the hot water heated by the solar or lowgrade waste heat is used to charge the weak solution. The solution generation (i.e. vapor desorption) happens in the generator and the vapor condensation takes place in the condenser. The charging temperature is usually 60-100°C. During this process, the solution temperature and concentration increase. Then, in the storage process, the rich solution and condensed refrigerant water is stored separately in their respective storage tanks. With no heat and mass transfer between solution and refrigerant, their temperatures gradually drop to the ambient. Three-phase process can happen during the charging or storage process if the concentration exceeds the solubility at the current temperature. In the discharging process, the water evaporation happens in the evaporator and its absorption takes place in the absorber. During this process, the evaporator and absorber produce cooling and heating, respectively. The solution becomes diluted again and the crystals dissolve during the discharging process.

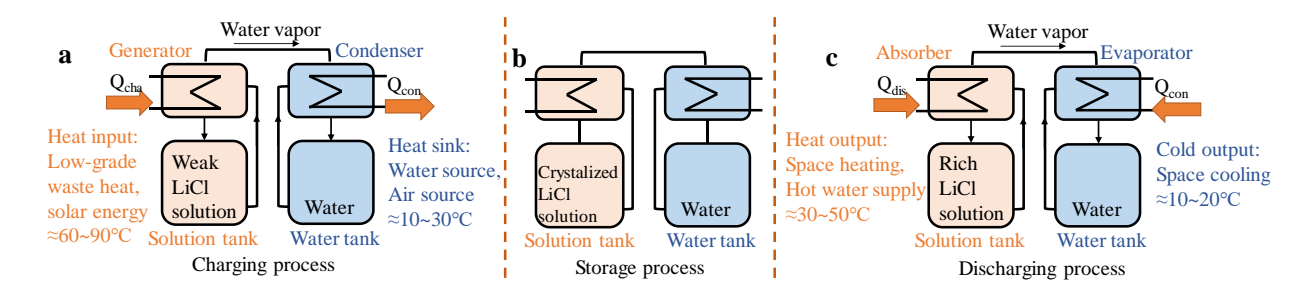


Figure 6.1 Operating principles of closed three-phase absorption TES system, (a) charging process; (b) storage process; (c) discharging process

The cycle diagram of closed three-phase absorption TES using LiCl solution is shown in Figure 6.2. The charging process, storage process and discharging process are represented by line 1-2-3, 3-4 and 4-5-1, respectively. Theoretically, the states 1-5 are governed by the temperature conditions during the charging and discharging processes. At the beginning of the charging process (state 1), the vapor pressure of LiCl solution is lower than the condensation pressure  $(p_{con})$ . Therefore, in principle, no vapor will be absorbed from the solution and the solution's temperature will increase follow the isoconcentration line. When the solution pressure reaches  $p_{con}$  (state 2), the vapor starts to generate following an isobaric process. The desorbed refrigerant vapor condensed in the condenser at the same pressure. The charging process ends when the solution temperature reaches  $T_{\rm cha}$ , when its pressure reaches an equilibrium state (state 3) at  $T_{cha}$ . If the concentration at state 3 is higher than the solubility, crystallization will happen during the charging process. During the storage process, the solution temperature declines to ambient temperature  $(T_{amb})$  at state 4. The crystallization will also happen with the decrease of solution temperature. At the beginning of the discharging process (state 4), the solution's pressure is lower than the evaporation pressure ( $p_{\text{eva}}$ ). During the discharging process, the refrigerant water evaporates from the evaporator at the evaporation temperature  $(T_{\text{eva}})$ . Cooling water is produced at evaporator. The vapor is then absorbed by the solution, both the solution's temperature and vapor pressure increase until the solution's pressure reach an equilibrium at  $p_{\text{eva}}$ . Then, the solution's temperature needs to drop to continue the discharging process. When the solution temperature drops below the discharging temperature ( $T_{\rm dis}$ ) at state 5, the discharging process ends. In this process, the dissolution of LiCl crystals happens with the increase in solution's temperature and decrease in concentration.

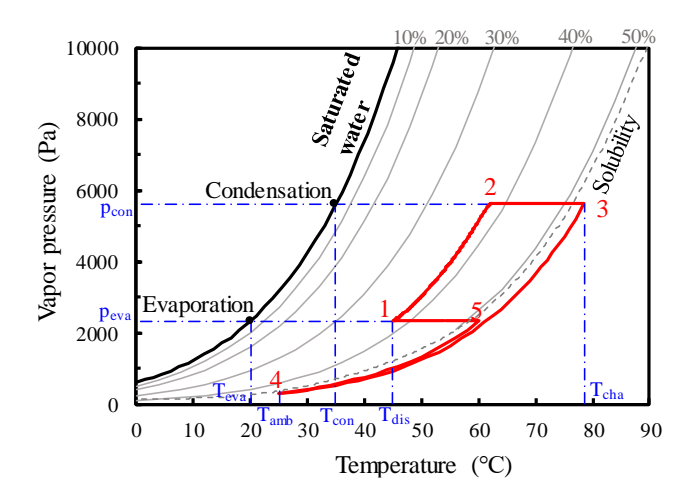


Figure 6.2 p-T-x phase diagram of closed three-phase absorption TES cycle

The experiments are conducted on the same test rig with previous two-phase absorption TES experiments. To prevent the crystals from entering the pump, an additional mechanical filter is installed in the outlet of solution tank, which is shown in Figure 6.3.

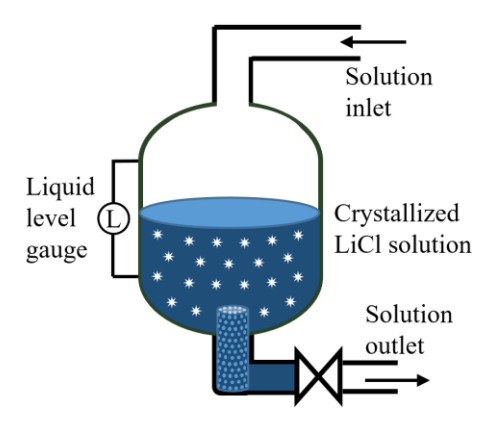


Figure 6.3 Schematic of solution storage tank and mechanical filter

# 6.2 Dynamic Charging and Discharging Characteristics

## 6.2.1 Dynamic charging characteristics under different charging temperatures

Figure 6.4 (a)-(d) shows the dynamic charging characteristics, including the variations of temperature, concentration and charging rate. At the  $T_{\rm cha}$  of 85°C and 75°C, the charging

process takes 144 minutes and 185 minutes to finish. Their concentration glide is 38.00%-54.26% and 37.99%-50.81%, respectively. Compared with two-phase absorption TES, whose maximum concentration glide is 38.00%-45.76% under the same working conditions, the concentration glide is largely extended. The total charged heat is 99696 kJ and 80018 kJ, respectively.

For the charging process of three-phase absorption TES cycle, the dynamic temperature and power variations follow the similar trend with that of two-phase absorption. In the beginning of the charging process, the heat charged is used for solution temperature rise and vapor desorption. The temperature difference between hot water inlet and outlet is also larger. The highest charging rate occurs in the beginning of the charging process and then gradually decreases. As the charging process progresses, the temperature difference between solution and hot water decreases, but the desorption rate does not drop significantly. This is because, during the charging process, the water vapor is continuously desorbed from the hot heat transfer plate in the falling film plate heat exchanger. The charging heat is mainly used for vapor desorption during this process. The desorption rate reduces only when the solution pressure approach the condensation pressure, at which the solution reaches an equilibrium state, signaling the end of the charging process.

The major difference between three-phase absorption and two-phase absorption lies in the final concentration of the working fluids. For the two-phase absorption, the highest concentration after charging is limited by the solubility. The charging process ends either when the solubility is reached or when the solution achieves thermodynamic equilibrium with respect to temperature, concentration and pressure. For the three-phase absorption, the charging process only ends when the solution reaches the equilibrium state.

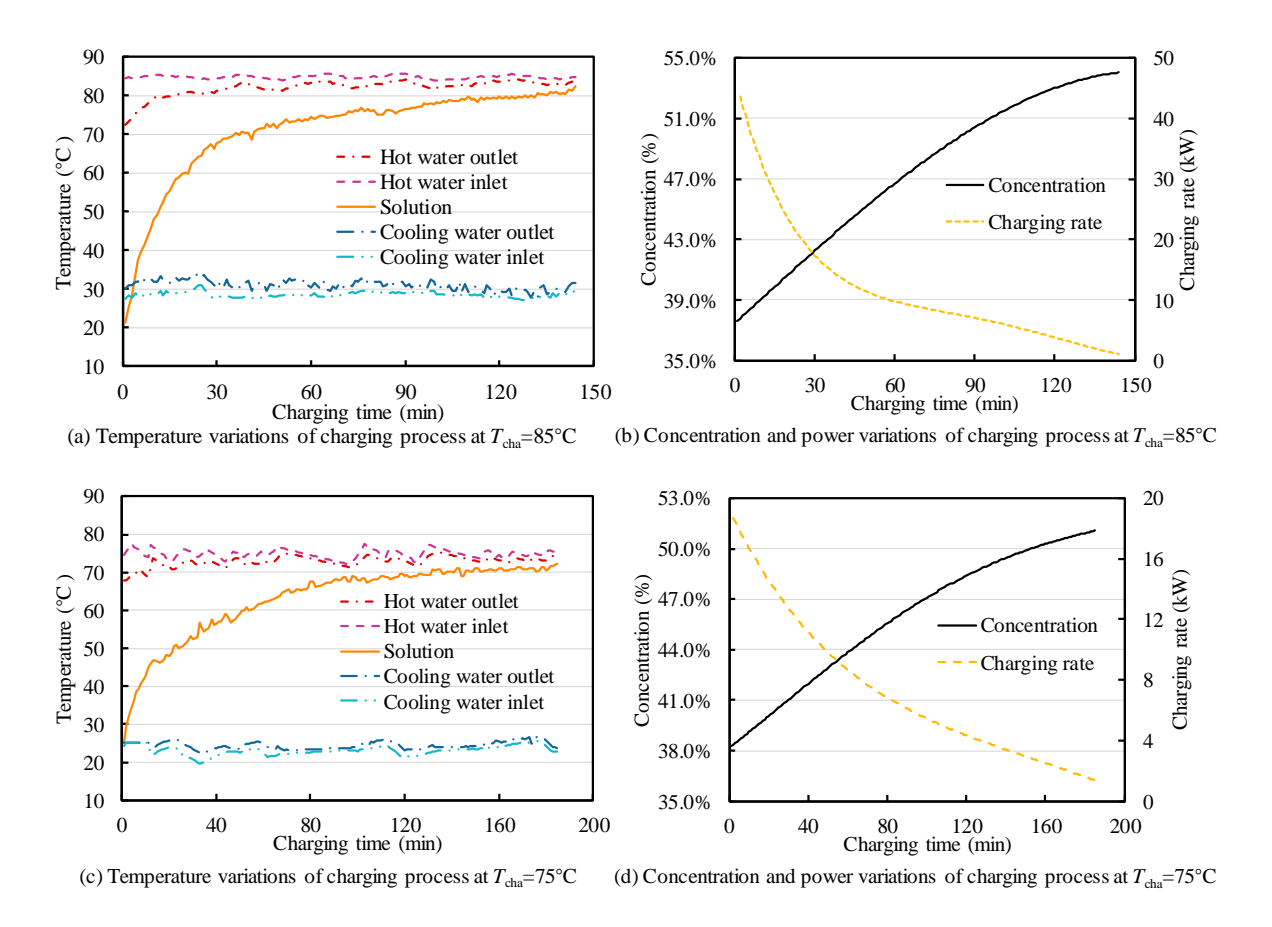


Figure 6.4 Dynamic charging characteristics of closed three-phase absorption TES at different charging temperatures. (a), (b) Charging at 85°C; (c), (d) Charging at 75°C

## 6.2.2 Dynamic discharging characteristics under different evaporation temperatures

Figure 6.5 (a)-(f) shows the dynamic discharging characteristics, including the variation of temperatures, concentration, crystallization ratio and discharging rate. To better reveal the three-phase process, the crystallization ratio and concentration variations are depicted in the Figure 6.5 (a)-(f). The crystallization ratio is defined as the mass of crystalized salt in the solution to the total mass of salt. The concentration only considers the LiCl concentration variations in solution's liquid phase. The concentration glide considers the ratio of the total mass of LiCl to the total mass of the solution, ignoring the variations in solubility due to temperature changes. For the heating, combined heating and cooling, and cooling applications, their concentration glides are 52.6%-40.95%, 52.80%-40.19%, and 52.16%-40.84% respectively.

For the 50°C heating application, the solution temperature gradually increases at the first 60 minutes, which is shown in Figure 6.5 (a). The crystallization ratio drops and concentration rises with the LiCl solubility increase and vapor absorption. The heating discharges after the solution temperature exceed 45°C. The initial crystallization ratio is around 12%. In the first 60 minutes, the absorption heat is mainly used for the solution's temperature rise, which can be seen in Figure 6.5 (b). During this process, the solution temperature gradually increases until it reaches the discharging temperature. As the temperature rises, the crystals gradually dissolve. The concentration of the solution equals the solubility before the crystals are fully dissolved. After 60 mins, the solution temperature is kept above 50°C. As the discharging process progresses, the solution pressure gradually increases due to dilution, and thus reduces the absorption and discharging rate. The discharging process lasts for around 240 minutes until the solution's temperature, concentration, and pressure reach an equilibrium state, and the discharging rate keeps low.

For the combined 40°C heating and 20°C cooling application, the cooling discharges throughout the discharging process while Figure 6.5 (d) shows that the heating and cooling discharging rates are highly correlated, which shows that the evaporated vapor can be effectively absorbed by the solution, which is similar to that of two-phase absorption cycle.

For the 10°C cooling application, since there's no heating output requirement, the solution temperature is kept at a lower level. It can be seen from the Figure 6.5 (e) that, the solution temperature, refrigerant temperature, and chilled water inlet and outlet temperatures fluctuate during the discharging process. Since no heating output is required, the discharging heat is released to ambient and solution temperature is kept at around 22°C (i.e. ambient temperature at during experiments). Consequently, the whole discharging process take longer time to finish. The complete dissolution of LiCl crystals also takes a longer time to achieve since the solution

temperature is maintained at a lower level. Combining Figure 6.5 (e) and Figure 6.5 (f), it can be observed that the discharging rate is influenced by both the solution temperature and the refrigerant temperature. During the period from 150 to 200 minutes, a slight increase in refrigerant temperature and a slight decrease in solution temperature result in a reduced slope of the discharging rate curve. Between 220 and 300 minutes, even though the refrigerant temperature continues to decrease, the discharging rate also declines to zero, indicating the completion of the discharging process.

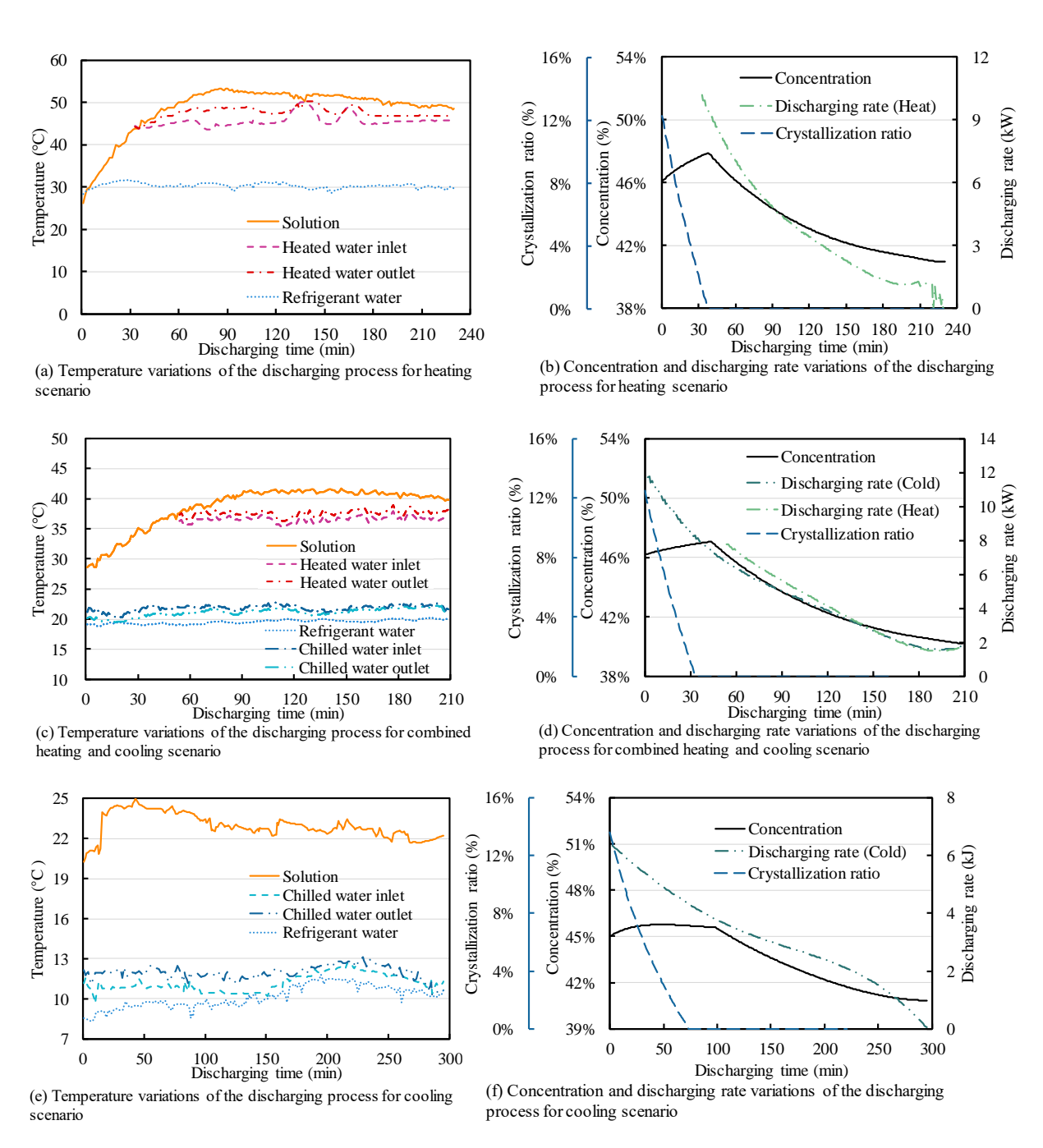


Figure 6.5 Dynamic discharging characteristics of closed three-phase absorption TES system for different application scenarios: (a), (b) Discharging for heating scenario; (c), (d) Discharging for combined heating and cooling scenario; (e), (f) Discharging for cooling scenario.

Table 6.1 summarizes the main results of the charging and discharging experiments. It can be found that the large concentration difference increases both charging heat and ESD. The total charging and discharging heat are calculated based on the temperature difference of the inlet and outlet water (i.e. heat transfer fluids) of the heat exchanger. Therefore, the heat loss and measurement error are included in the experimental results. Nevertheless, the ESD is still high due to the large concentration difference in three-phase absorption TES. The maximum ESD recorded is 519.2 kJ/kg solution at a concentration difference of 52.8%-40.2% for cooling discharge at 20°C.

Table 6.1 Summary of the charging and discharging process

		Total Q <sub>cha</sub> /	Charging heat	ESD (kJ/kg	Concentration	Time
		$Q_{\mathrm{dis}}\left(\mathrm{kJ}\right)$	(kJ/kg solution)	solution)	glide (%)	(mins)
Charging at 75°C		103796	902.57	/	38.00-50.81	185
Charging at 85°C		114210	993.13	/	38.00-54.26	152
Discharging for heating		46237	/	402.06	52.60-40.95	230
Discharging for	Heating	30854	/	268.30		
combined heating and cooling	Cooling	59711	/	519.23	52.80-40.19	209
Discharging for cooling		49799	/	433.03	52.16-40.84	295

The ESD values of three-phase absorption derived from experiments are compared with the theoretical ESD of the two-phase and three-phase absorption TES. The theoretical results are calculated based on the temperature and concentration variations of the solution during charging and discharging. The theoretical ESD of two-phase absorption TES using the same working fluid is discussed in our previous work. The results are presented in Fig. 7. It can be seen that the experimental results have minor differences from theoretical results, which is mainly due to heat loss and measurement errors. Compared to the theoretical results of two-phase absorption TES, the experimental results indicate a significant enhancement in ESD, even when accounting for the difference from theoretical results. The enhancement ranges from 19.3%-80.3%, depending on the working conditions, particularly the concentration difference.

## 6.2.3 Model validation and performance mapping

The validation of the model is conducted by comparing solution temperature and concentration variations during charging and discharging processes with experimental results, which is shown in Figure 6.6. The model inputs are aligned with the experimental conditions. It can be seen that the overall trend matches the experimental results. Some minor deviations can be observed at the beginning of the charging and discharging process, where the solution temperature rises faster and concentration changes slower in the simulation model. For temperature variation, the model neglects the heat capacity of the component and heat loss, resulting in a faster solution temperature increase than the experimental results in both charging and discharging processes. For concentration variation, the concentration of LiCl's equals the solubility at the beginning discharging process due to the dissolution of LiCl crystals. The rise in concentration is driven by the fast temperature increase at the start of discharging. Once the solution temperature reaches  $T_{\rm dis}$ , the concentration remains at solubility until all the crystals are dissolved. Additionally, measurement errors can contribute to some of the observed

deviations. Overall, the established model demonstrates feasible for studying the charging and discharging performance.

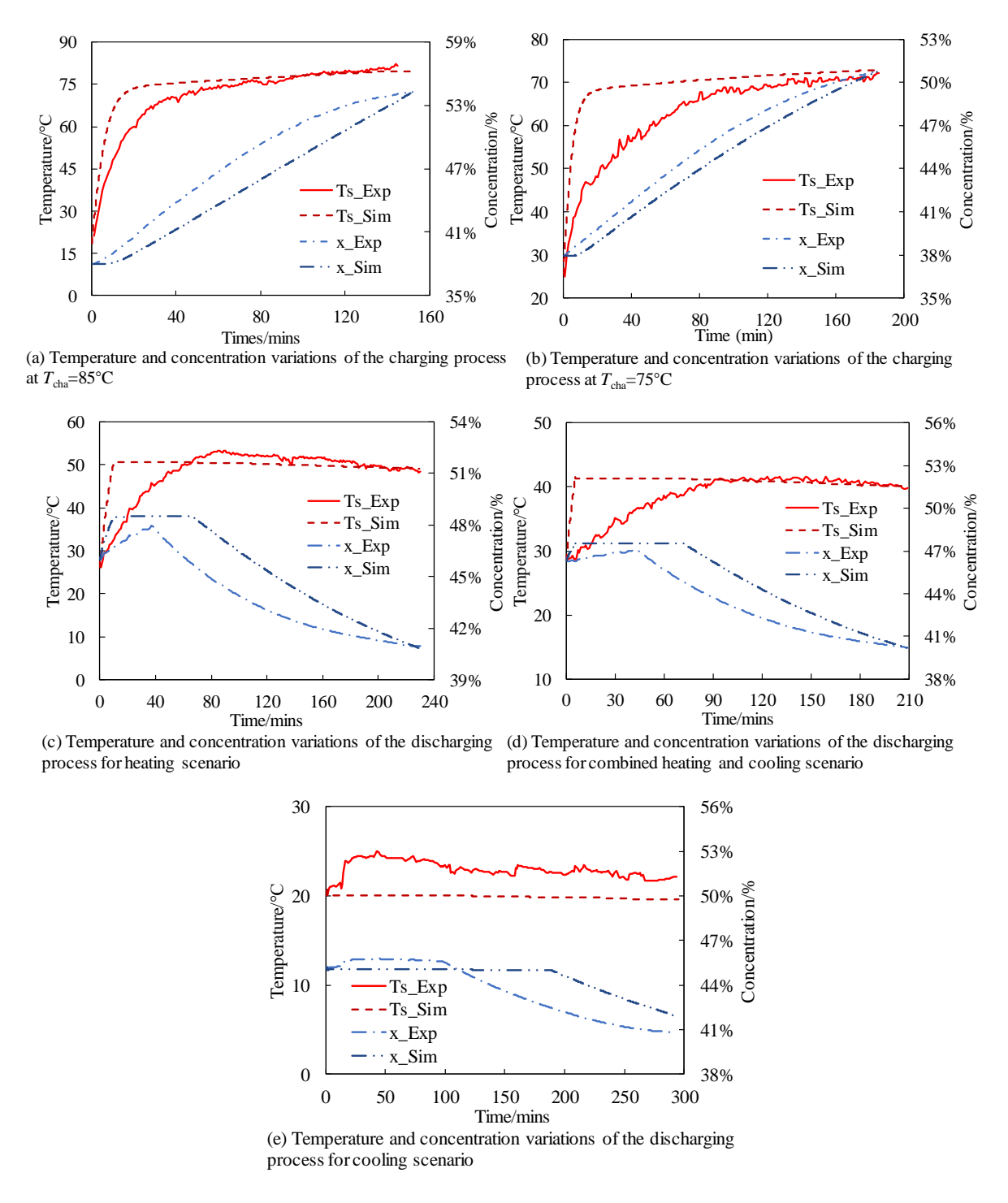


Figure 6.6 Validation of the closed three-phase absorption TES model (a), (b) Temperature and concentration variations in the charging process; (c), (d), (e) Temperature and concentration variations in the discharging process

The ESD of three-phase absorption from experiment are also compared with the simulation results, both two-phase and three-phase absorption. The results are displayed in Figure 6.7. In the simulation, the total charging and discharging heat is calculated by thermodynamic properties of LiCl solution. Therefore, the ESD from simulation can be regarded as the theoretical values. It can be seen that the experimental results have minor differences with simulation results. The main differences lie in heat loss and measurement error. Despite this, three-phase absorption can significantly enhance the ESD compared with two-phase absorption. The simulation results further demonstrate the feasibility of the model.

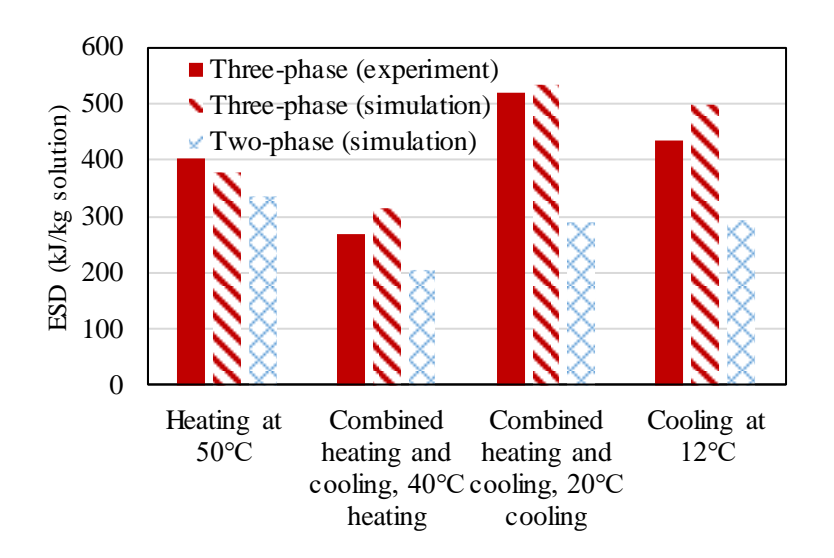


Figure 6.7 Comparison of the ESD of three-phase and two-phase absorption TES

# 6.3 Performance Evaluation of Three-phase Absorption TES

#### **6.3.1** Charging performance

In absorption TES system, the charging process is mainly governed by the  $T_{\rm cha}$  and  $T_{\rm con}$ . Generally, higher  $T_{\rm cha}$  and lower  $T_{\rm con}$  lead to larger concentration glide through influencing the pressure level during charging process. For three-phase absorption TES,  $T_{\rm cha}$  can be even higher, and the theoretical mass fraction of LiCl during charging process can exceed the solubility at ambient temperature (around 46%) and reach up to 70.2% (i.e. the mass fraction of LiCl in LiCl monohydrate crystals).

For the charging performance evaluation, the  $T_{\rm cha}$  ranges from 60-85°C and  $T_{\rm con}$  ranges from 20-35°C, covering the temperature range of the charging process. The solution initial concentration is 38%. Therefore, the concentration glide can be reflected by LiCl's mass fraction after charging, which is determined by  $T_{\rm cha}$  and  $T_{\rm con}$ . Figure 6.8 shows the relationship between total charging heat and concentration difference at different charging temperature and condensation temperature. The total charging heat is almost linear to the LiCl's mass fraction after charging despite the variations of the  $T_{\rm cha}$  and condensation temperature. The charging heat can be divided into two parts, one is used for temperature increase (i.e. sensible heat), the other one is used for vapor desorption (i.e. desorption heat). The sensible heat slightly increases with an increase in  $T_{\rm cha}$ , which is negligible compared with the increase in vapor desorption heat. The vapor desorption heat is also linear with the concentration glide. Since the sensible heat will be released back to the ambient during the storage process, only the desorption heat can be regarded as the heat stored. At larger concentration difference, a larger proportion of heat is used for desorption. Compared with two-phase absorption under largest concentration glide (i.e. with a LiCl's mass fraction of 46%), the charging heat is 2.5 times higher when LiCl solution becomes complete LiCl monohydrates, indicating the potential high ESD.

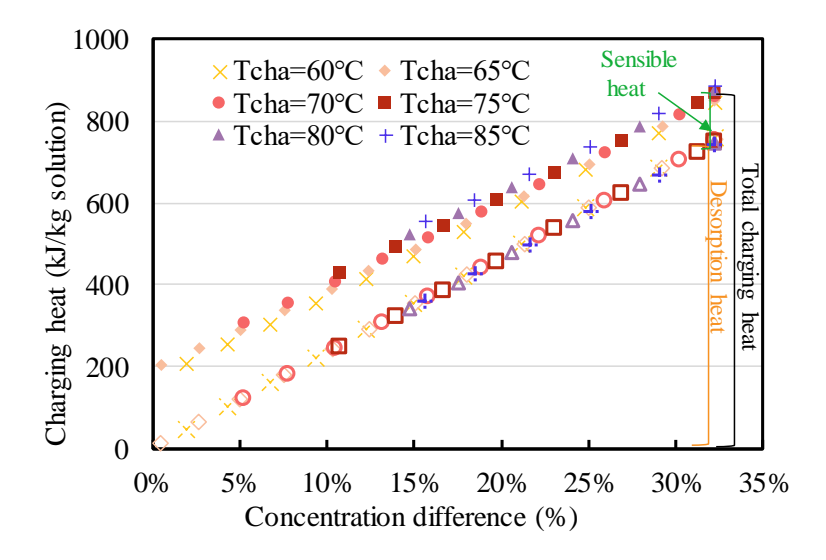


Figure 6.8 Impact of concentration difference on the charging heat

#### **6.3.2** Discharging performance

For the discharging process, the  $T_{\rm eva}$  determines the evaporation pressure, and the evaporation pressure and  $T_{\rm dis}$  determine the equilibrium state of solution after discharging. (i.e. the concentration difference of discharging process). Generally, higher  $T_{\rm eva}$  and lower  $T_{\rm dis}$  lead to larger concentration glide. In the discharging performance evaluation,  $T_{\rm eva}$  and  $T_{\rm dis}$  also covers the full temperature range of discharging process.  $T_{\rm eva}$  ranges from 10~30°C. The  $T_{\rm dis}$  is 60°C, 55°C, 50°C, 45°C, 40°C for heating output and 20°C, 15°C, 10°C for cooling output.

Figure 6.9 shows the relationship between ESD and concentration difference. It is evident that the ESD increases with an increase in the concentration difference for all  $T_{\rm dis}$ , which also underscore the significance of concentration difference as a critical factor in the performance of the absorption TES system. For two-phase absorption TES, the concentration difference is usually lower than 10%, which limits the ESD for both heating and cooling. The heat storage density is lower than cold storage density since part of the heat discharged is used to rise the solution temperature to meet  $T_{\rm dis}$ .

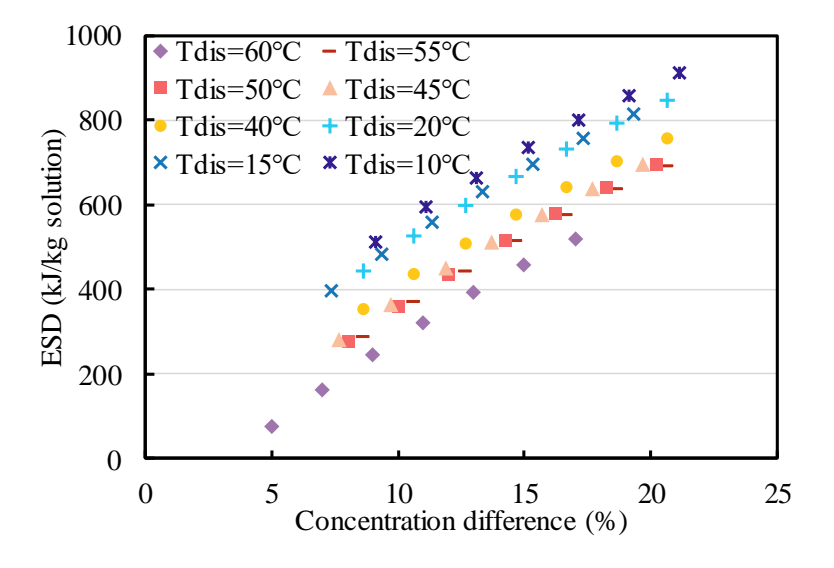


Figure 6.9 Impact of concentration difference on ESD

# **6.4 Summary**

In this study, a closed three-phase absorption TES system experimental test rig was established to exploit the energy storage potential of three-phase absorption TES. Three-phase absorption cycle, characterized by high ESD with large concentration difference via crystallization and dissolution, is realized experimentally. The charging and discharging experiments were conducted under three working conditions, namely heating, combined cooling and heating, and cooling conditions. The dynamic charging and discharging characteristics and energy performance under experimental working conditions were studied. Also, a mathematical model was established and validated using experimental data. The performance of closed three-phase absorption TES at all working conditions was studied comprehensively. The main conclusions are drawn as follows:

- 1. In the charging process, a higher charging temperature leads to a higher concentration difference, higher charging rate and larger total charging heat. The total charging heat is almost linear to the concentration difference. A large concentration glide is also beneficial to exploit the storage potential of absorption TES.
- 2. The closed three-phase absorption TES can significantly enhance ESD compared with the two-phase absorption cycle. The results demonstrate significant enhancements in ESD attributed to the large concentration difference, outperforming traditional two-phase absorption systems.
- 3. The charging heat and ESD are mainly dependent on the concentration difference. The impact of temperature conditions can be concentrated on the concentration difference.
  The increase in concentration difference brings higher charging heat and ESD.

# Chapter 7 Enhanced load following strategy for capacity design and operational control of absorption thermal energy storage in distributed energy systems

# 7.1 Description of the proposed distributed energy systems (DES)

Figure 7.1 shows the schematic of the distributed energy system (DES). The DES system consists of distributed generators (DGs), an electric chiller, an absorption chiller, an absorption TES, buildings, and the power grid. Buildings with electricity, heating, and cooling loads serve as the end users. The DGs in the DES include PV for electricity generation and combined heat and power (CHP) for electricity generation and heating supply. The DES operates in grid-connected mode, where electricity generated by PV and CHP supplements building loads, with bidirectional energy exchange to the grid during supply-demand mismatches. The electric chiller and absorption chiller are used to provide cooling to buildings. The electric chiller is driven by electricity produced or imported, while the absorption chiller is driven by the waste heat from CHP. Absorption TES is used to accommodate the excess waste heat and balance the heating and cooling demand. The optimal design of the system was conducted in a previous study by our research team. The capacity and specifications of the components are in Table 7.1.

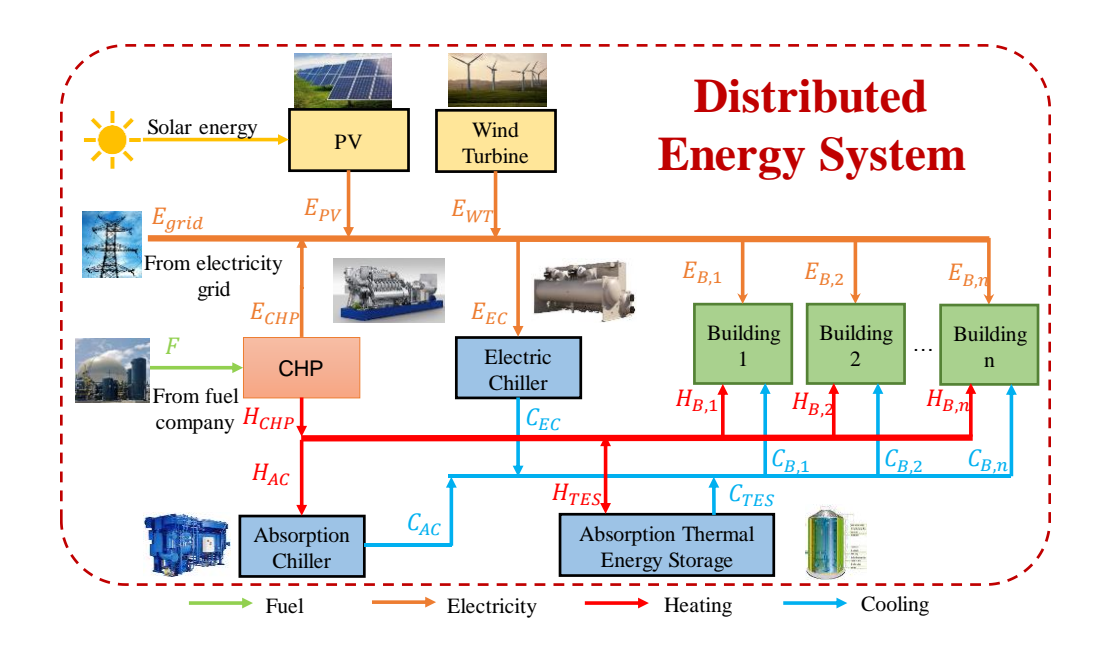


Figure 7.1 Schematic of distributed energy system

Table 7.1 Specifications of the major heating and cooling components

Equipment	Parameters	Value	
СНР	Rated capacity (kW)	1500	
Building HVAC	Indoor setting(°C)	23	
	Comfort range(°C)	21-25	
	Operation period	7~21	
Electric chiller	Full load capacity (kW)	5000	
Absorption chiller	Full load capacity (kW)	3000	

To evaluate the performance of the DES without absorption TES, a case study is conducted. The building contains four ASHRAE prototype office buildings with a total area of 100000 m<sup>2</sup> in total. The building model is established using TRNBuild. The meteorological data from the Hong Kong Observatory is used in the simulation. Figure 7.2 shows the load patterns of the DES without absorption TES, including electricity load, heating load, cooling load, and waste heat load. The electricity load of the buildings mainly comes from lighting and equipment. The cooling load mainly comes from internal heat gains and external envelope, while the heating load mainly comes from service water. It can be seen that for the office buildings, the load profile exhibits typical patterns, with a high cooling load during the daytime and a low cooling load during the nighttime.

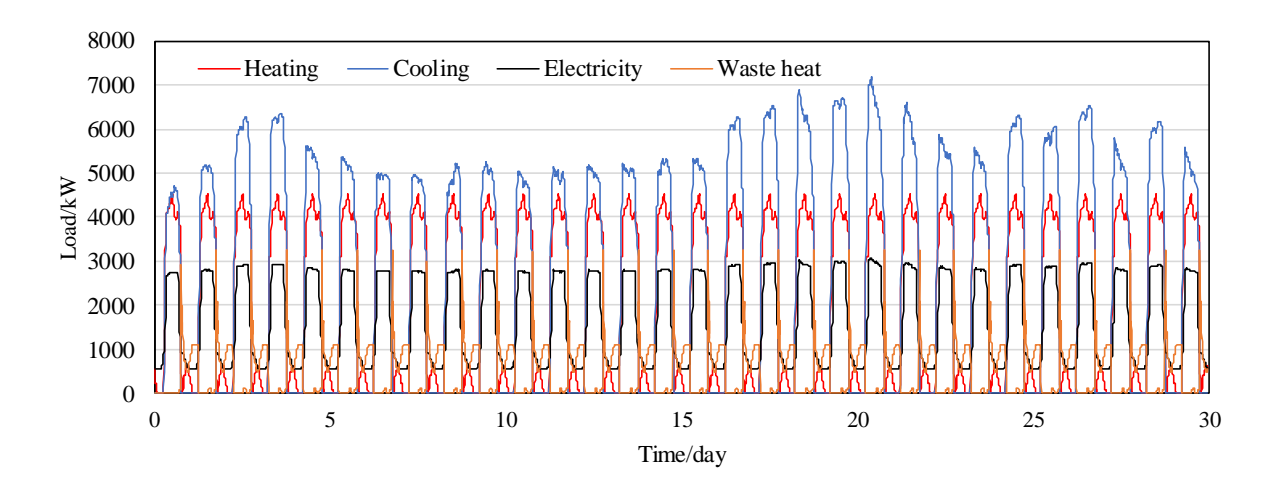


Figure 7.2 Load patterns of DES in July

The operational mode of the CHP is heat-led, where its electricity generation is dynamically coupled to the system's thermal demand. This thermal demand originates primarily from two sources: (1) the heat input required to drive the absorption chiller and (2) direct building heating requirements. The absorption chiller operates only when the cooling load exceeds its rated capacity, prioritizing base-load cooling supply, while the electric chiller compensates for the residual cooling demand. The CHP unit adjusts its output to match the total thermal demand (absorption chiller input + building heating). However, a critical constraint arises from the CHP's minimum power threshold: excess waste heat will inevitably be generated when the thermal load falls below this threshold. The integration of absorption TES can help better utilize this excess waste heat and reduce the electricity consumption of electric chillers.

# 7.2 Optimal design and operational control of absorption TES in DES

This study establishes a novel framework for optimizing absorption TES integration in DES, focusing on two interrelated objectives: (1) capacity design driven by dynamic thermal characteristics, and (2) operational control using an enhanced load following strategy.

Figure 7.3 shows the framework of optimal design and operational control of absorption TES in DES. Absorption TES is designed to recover waste heat from CHP and supply cooling for buildings. The load patterns of the DES are first obtained using TRNSYS. Then, based on

the load patterns, especially the waste heat load of DES, the capacity of absorption TES (i.e. solution mass) is estimated with several target waste heat recovery ratios. Next, the performance of DES with the integration of absorption TES is simulated. To better capture the transient behavior of absorption TES in the simulation, the dynamic charging and discharging characteristics of absorption TES are taken into consideration. An enhanced load following strategy is proposed for the control of absorption TES. For each target recovery ratio, the optimal design and control are conducted simultaneously to find the minimum absorption TES capacity required.

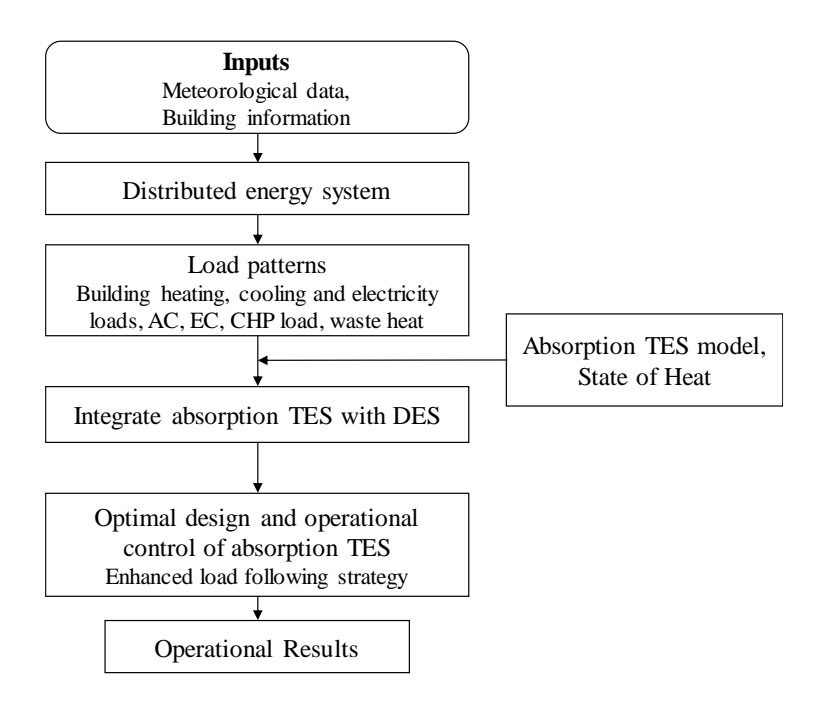


Figure 7.3 Framework of capacity design and operational control

For the absorption TES, the dynamic charging and discharging models established in the previous sections are used during capacity design and operational control. Considering the dynamic charging characteristics of absorption TES, the charging rate of the solution ( $P_{cha}$ ) is influenced by its temperature and concentration. Therefore, the charging rate does not always follow the waste heat load. Large variations of waste heat can lead to inefficient recovery. The recovery ratio is defined as the waste heat recovered by the solution to the total waste heat, as shown in Eq.(1). The target recovery ratios are set at 70%, 80%, 90%, 99%. The objective of

the capacity design is to obtain the minimum required solution mass that can meet each recovery ratio.

Recovery ratio = 
$$\frac{\int m_{\text{sol}} q_{\text{cha}} dt}{\int P_{\text{wh}} dt}$$
 (1)

State of heat (SOH) is utilized as a dynamic control parameter. SOH is defined as the ratio of accumulated thermal energy to maximum storage capacity, as shown in Eq.(2). In principle, the SOH is influenced by the concentration and temperature of the solution during charging and discharging. Therefore, the real-time SOH can be used as an indicator to reveal the current state of the solution, including the storage potential during charging and energy output potential during discharging. Meanwhile, SOH can also be used to estimate the charging and discharging power variations and thus help update the control. During the simulation, the SOH is updated simultaneously by Eq.(3).

$$SOH = \sum \frac{\int P_{cha}dt}{m_{sol}q_{cha,max}} - \sum \frac{\int P_{dis}dt}{m_{sol}q_{dis,max}}$$
 (2)

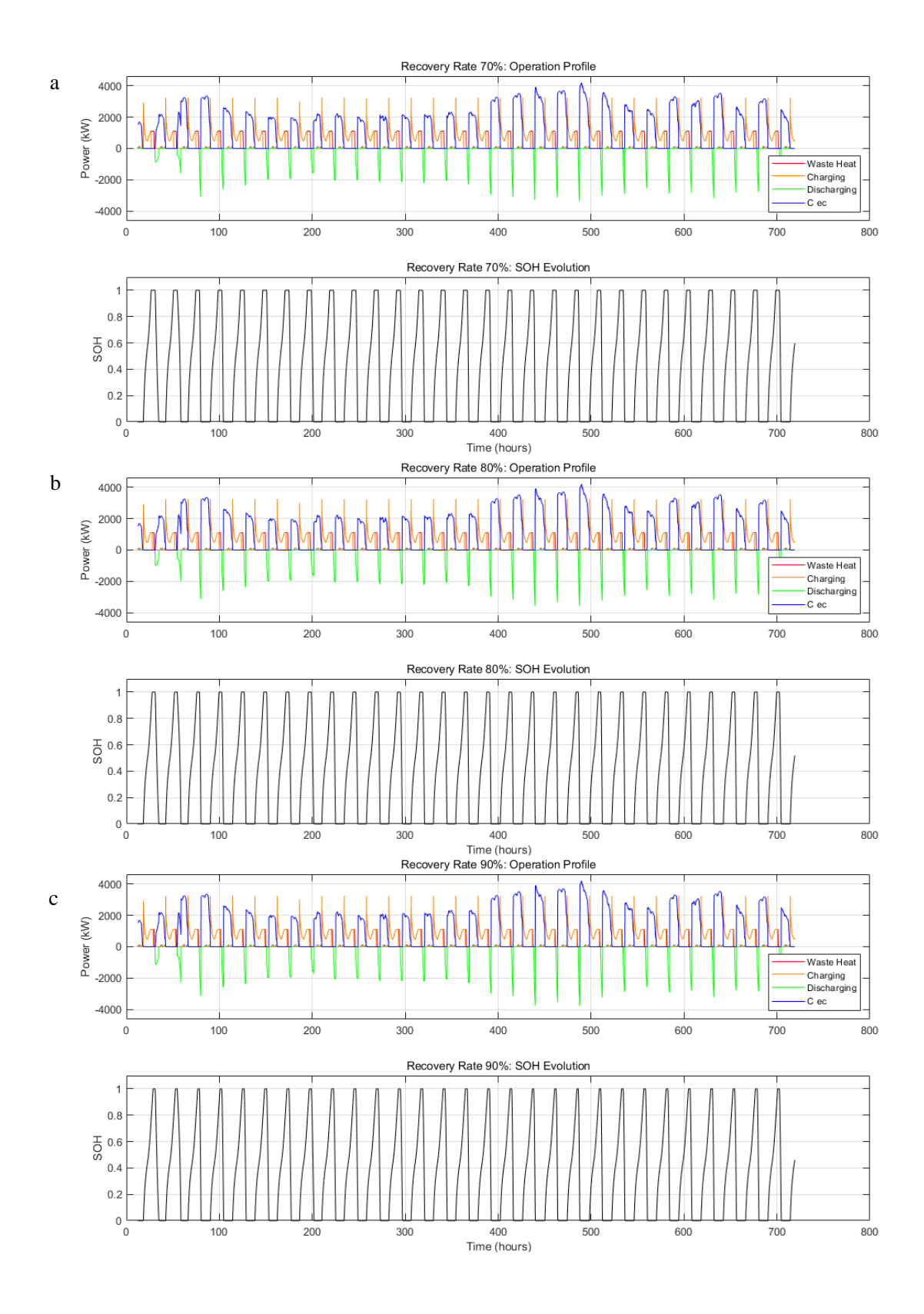
$$SOH(t+1) = SOH(t) + \frac{P_{cha}\Delta t}{m_{sol}q_{cha,max}} - \frac{P_{dis}\Delta t}{m_{sol}q_{dis,max}}$$
(3)

Compared with the conventional load-following strategy that follows waste heat load during charging and electricity load during discharging, the proposed strategy incorporates SOH to regulate the operation of absorption TES. The sequential variation of SOH is recorded as an indicator for continuous charging during waste heat periods and continuous discharging under peak cooling demand hours. The optimal control also regulates the charging and discharging rate based on load pattern and SOH, so as to balance the waste supply and cooling demand. The proposed strategy can help best utilize the storage potential for waste heat recovery and load reduction.

### 7.3 Results and discussions

Figure 7.4 (a)-(d) shows the operational results of DES at each waste heat recovery ratio. Key parameters, including surplus waste heat, absorption TES charging/discharging rates, and electric chiller cooling output, demonstrate distinct operational patterns. The charging and discharging processes exhibit periodic cycles without abrupt mode transitions, showing the feasibility of enhanced load following strategy. The charging rates are dynamically adjusted during the charging process, following the waste heat load. The increase in the recovery rate can be observed from the increasingly close match between the waste heat and the charging rate. The discharging rate also follows the electric cooling supply. Similarly, discharging rates align with the electric chiller's cooling demand, though full coverage remains unattainable due to the inherent disparity between the chiller's total cooling load (predominantly driven by building demand) and the absorption TES's storage capacity.

The variations in SOH further validate the control logic: during each cycle, the SOH consistently varies between its maximum (1.0) or minimum (0.0), indicating full utilization of the TES's storage potential. This periodic behavior aligns with the load pattern, which maximizes the storage potential. Additionally, it reduces the energy loss associated with frequent switching between charging and discharging modes, as the charging process involves a portion of energy being used to raise the temperature of the solution, which does not contribute to effective waste heat recovery.



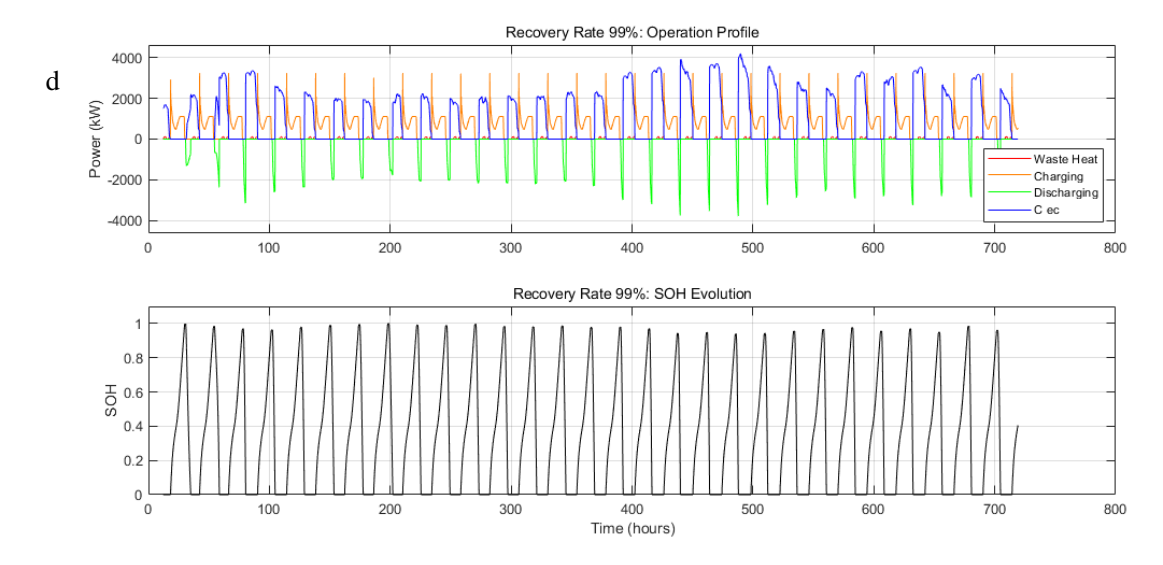


Figure 7.4 Variations of key parameters of DES integrated with absorption TES

Figure 7.5 presents the relationship between the waste heat recovery ratio, solution mass, and electric chiller electricity consumption. To better reveal the impact of the recovery ratio, 75%, 85% and 95% recovery ratios are added to the simulation. It can be seen that while the required solution mass is almost linear to the recovery ratio, it shows an increasing trend when the recovery ratio approaches 99% (since 100% recovery of waste heat is almost impossible, the maximum recovery ratio is set at 99%). This disproportion shows that the marginal gains in waste heat utilization required disproportionately large storage capacities, which can be more significant if the waste heat pattern exhibits greater randomness.

Correspondingly, the electricity consumption by the chiller (E\_EC) can be reduced by 13%-17.5% with the increase in the recovery ratio (i.e., solution mass), indicating a high energy-saving potential of the proposed enhanced load-following strategy.

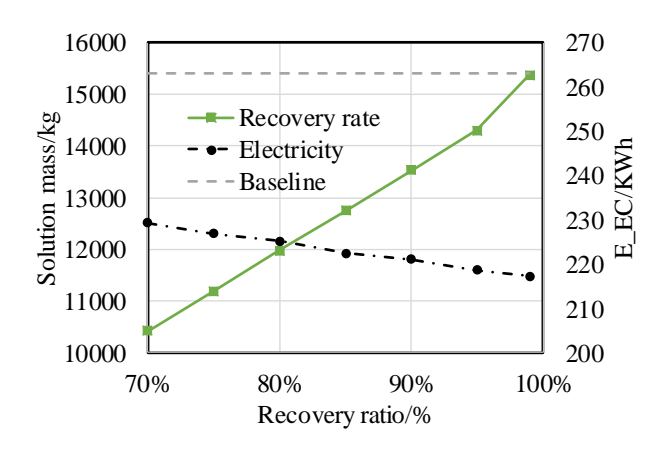


Figure 7.5 Impact of recovery ratio on solution mass and energy saving

# 7.4 Summary

This chapter investigates the integration of absorption thermal energy storage (TES) into district energy systems (DES), focusing on capacity design and dynamic operational control. An enhanced load-following strategy is proposed to utilize real-time variations of waste heat supply and energy demand considering the storage state of the solution, quantified by the SOH. The results demonstrate that the proposed strategy dynamically aligns charging/discharging processes with waste heat availability and cooling demand while minimizing operational mode transitions. Also, the introduction of SOH reduces the frequent switching between charging and discharging, achieving a high energy efficiency at its maximum storage potential. The key findings and contributions are summarized as follows:

The proposed strategy facilitates the capacity design for target waste heat recovery ratios. The results reveal a nonlinear relationship between solution mass and recovery efficiency: increasing the recovery ratio from 70% to 95% brings a 37% rise in solution mass (10,415 kg to 15,377 kg). However, when the recovery rate increases to 99%, the required mass will be much higher.

The proposed enhanced load following strategy introduces SOH as a critical control parameter to regulate charging/discharging cycles. The operation of absorption TES adapts

continuously to waste heat supply and cooling demand while considering its thermodynamic state. The proposed strategy also improves energy efficiency by eliminating partial charge-discharge cycles, ensuring full utilization of the TES's storage capacity during each operational cycle.

The integration of absorption TES reduced reliance on the electric chiller, lowering its electricity consumption by 13–17.5% across recovery ratios.

# **Chapter 8** Conclusions and Recommendations

Absorption TES systems rely on reversible sorption and desorption reactions with large binding heat, which enables the absorption TES to have high ESD potential. Three-phase absorption TES have even higher ESD since the concentration difference is larger. However, in real operation, high concentration increases the crystallization of working fluids. Also, the heat and mass transfer inside the heat exchangers have always been a challenge in absorption TES systems.

The main contributions of this thesis are the ESD enhancement of absorption TES system from material, cycle, component and experimental level, and system level comprehensively. At the material level, a novel modified LiCl solution with ethylene glycol (EG) and silica nanoparticles (SNPs) as additives is developed. The modified solution aims at enhancing ESD by expanding concentration glide. Both EG and SNPs optimize the properties of the LiCl solution at high concentration, and therefore allow the solution to function at high concentration. To be specific, the introduction of EG increases the solubility of LiCl, while SNPs serve as nucleation sites for heterogeneous crystallization, promoting the growth of fine crystals, ensuring the fluidity of working fluids for three-phase absorption, and allowing the modified solution to operate at even higher concentrations than with EG alone. At the cycle level, the closed three-phase absorption TES cycle is proposed and evaluated with the assist of the proposed working fluids. A methametical model is established to evaluate its energy storage performance. At the component and experimental level, an experimental test rig with noveldesigned heat exchangers with narrow and wide channels is established. The proposed heat exchanger has high heat and mass transfer efficiency. The wide channels provide large contact area for mass transfer with minor pressure drop. Then, an experimental test rig is constructed using the proposed novel heat exchanger. The experimental test rig is designed to realize both the two-phase and three-phase absorption TES cycles. The dynamic heat and mass transfer

characteristics and energy performance of the two-phase and three-phase absorption TES systems were experimentally investigated. The feasibility of using ethylene glycol (EG) as an additive was confirmed. The proposed mathematical model is validated using experimental data, after that, the energy performance at all working conditions is evaluated. At the system level, the absorption TES model is integrated with a distributed energy system (DES). The capacity of absorption TES is designed and its operational control method is proposed. For the capacity design, the capacity at different waste heat recovery ratio is obtained. For operational control, an enhanced load-following strategy is proposed to utilize variations in waste heat supply and energy demand, considering the storage state of the solution, quantified by the state of heat (SOH).

#### Conclusions on Main Contribution

- 1. The addition of EG increases LiCl solubility, expanding the working concentration range and boosting ESD. The modified solution's concentration after charging increased from 44% (conventional) to 48% with EG and up to 53% with both EG and SNPs. Compared to conventional LiCl solutions, the modified fluids exhibit significantly higher ESD, up to 24.8% increase in heat storage density and 156.0% in cold storage density with the optimal LiCl:EG:SNPs ratio of 50:8.5:1.5.
- 2. A novel test rig with specially designed heat exchangers was constructed to experimentally validate two-phase and three-phase absorption TES cycles. The introduction of EG extended concentration glide and enhanced ESD. The LiCl solution containing 5% EG achieving the highest ESD values of 123 kWh/m³ for heating mode, 177 kWh/m³ for combined heating and cooling mode, and 108 kWh/m³ for cooling mode. These enhancements represent increases of 18%, 46%, and 48%, respectively, achieving recordhigh experimental values for closed two-phase absorption TES.

- 3. The three-phase cycle demonstrated superior performance, with charging temperature increases leading to higher concentration differences and charging rates. Discharging experiments showed ESD improvements of 19.3% to 80.3% over two-phase cycles, with solution temperatures exceeding 40–50°C and sustained discharging power above 2 kW. A validated closed absorption TES model revealed strong correlations between concentration difference, charging heat, and ESD, providing insights into system behavior under varying conditions.
- 4. The integration of absorption TES with DES shows promising results. The proposed enhanced load-following strategy reduces frequent mode switching, improves energy efficiency, and decreases reliance on electric chillers, achieving electricity savings of 13–17.5%.

#### Recommendations for Future Study

This study mainly concentrates on the dynamic characterization and performance enhancement of absorption TES systems from several aspects, including the modification of working fluids, the development of the advanced closed three-phase absorption cycle, dynamic characterization and energy performance analysis of modified working fluids in two-phase and three-phase absorption TES systems, and the control strategies in energy systems. Future research on the following aspects would be valuable for the further development and application of absorption TES systems.

 Future research could expand the types and concentrations of additives to maximize the ESD with better thermal and physical properties, which is the fundamental of absorption TES systems.

- 2. The design of heat exchangers could be improved in terms of the compactness and efficiency of the absorption TES system, especially considering the non-Newtonian behavior of the modified working fluids.
- The long-term stability and reliability of the modified working fluids should be assessed, which is critical for the application of absorption TES systems in long-term or mobilized TES systems.
- 4. Integration absorption TES systems with renewable energy sources and energy systems can further expand their application scenarios. However, practical challenges such as system size, operational strategy relies highly on the system itself. Developing system design and control method with high performance and good generalizability requires further investigations.

# **Appendix**

Programming Code of Absorption Thermal Energy Storage Processes

# Charging process

```
Program charging
    Implicit none
    !for subscripts, 0 indicates previous time step, 1 indicates present
time step.
    real UAg, UAc!UA value of heat exchanger in generator and condenser
    real Tgi, Tci, Tgo, Tco, Tg, Tgmax, Tc, T, pc, pg !Generator in, condenser in,
generator out, condenser out, generator, condenser temperature
    real Ms, Mw, mc, mg, mv, x, xt, xi, xmax, sol, MsO, Ms1, mvO, mv1 !xi is the initial
concentration, which is used to correct the concentration during iteration
    real Cps, Cpw
    real qci, qco, qgi, qgo, qchaenth, qchalt
    real hw, hv, hs, hs0, hs1
    real Tg0, Tg1, Tg2 !Tg1 is the temperature at previous time step, Tg2 is
the temperature at next time step
    real i
    i=1
    !Check the initial working conditions
    print*, "Please check the initial temperature Tgi, Tci, and initial
concentration x"
    UAg=4.4; UAc=3.2; mg=1.2; mc=0.8; Ms=100; Mw=62.05; qchaenth=0; qcha1t=0
    !Initial status
    print*, "please input the charging temperature"
    read*, Tg; Tgi=Tg
    !print*, "please input the condensation temperature"
    !read*, Tc
    Tc=30
    Tgmax=1.1194*Tc+39.297
    call vaporpressure (Tc, pc)
    if (Tg<Tgmax) then
        pg=pc
        call solveconcentration(pc, Tg, xt)
        xmax=xt
    else if (Tg>Tgmax .or. Tg==Tgmax) then
        xmax=1.0687*10.**(-5)*Tg**2+9.4577*10.**(-6)*Tg+0.45801
    end if
```

```
print*, xmax
    print*, "please input the initial temperature of solution"
    read*, T
    x=(Ms-Mw)/Ms; TgO=T; Tg1=T; Tg=T; xi=x! Fix the value of xi
    call enthalpy (Tg, x, hs)
    hs0=hs:Ms0=Ms:Ms1=Ms0
    Tci=Tc-3
    !print*, "please input the condensation temperature"
    !read*, Tc
    xmax = 0.5081
    do while (x<xmax)
            qco=10;qci=1
    x = (Ms0-Mw)/Ms0
    !Heat exchange inside condenser
    call solutionCpw(T, Cpw)
    Tco=Tc-(Tc-Tci)/exp(UAc/(Cpw*mc))
    qco=Cpw*mc*(Tco-Tci)
    call vaporpressure (Tc, pc)
    call waterenthalpy (T, hw)
    !Assume the initial value of heat exchange inside and outside the
generator to initiate the cycle
    qgo=10;qgi=100
    Tg2=Tg1+2; Tg=0.5*(Tg1+Tg2)
    so1=2.725E-12*Tg**6-7.545E-10*Tg**5+7.502E-8*Tg**4-2.826E-6*Tg**3-
6. 49E-8*Tg**2+3. 29E-3*Tg+0. 3975
    if (xt>sol .or. xt==sol) then
        x = sol
    else if (xt<sol) then
        x=xt
    end if
    !Choose a proper pressure formula
    if (Tg>59) then
        call solpressure (Tg, x, pg)
    else if (Tg < 59 \cdot or. Tg == 59) then
        call solutionpressure (Tg, x, pg)
    end if
    x=xt
```

!Dynamic charging characteristics during preheating stage

```
if ((pg < pc) \cdot or \cdot pg == pc) then
    do while (abs(qgi-qgo)>0.5)
        if (qgo>qgi) then
             Tg1=Tg; Tg=0.5*(Tg1+Tg2)
        else if (qgo<qgi .or. qgo==qgi) then
             Tg2=Tg; Tg=0.5*(Tg1+Tg2)
        end if
        mv=0; xt=x; x=xi
        call enthalpy (Tg, x, hs)
        hs1=hs;qgi=Ms0*(hs1-hs0)
        T=Tg
        call solutionCpw(t, cpw)
        Tgo=Tg-(Tg-Tgi)/exp(UAg/(Cpw*mg))
        qgo=UAg*(Tgi-Tgo)/log((Tgi-Tg)/(Tgo-Tg))
    end do
    !print*, "1", Tg, x, Tgi, Tgo
    !print*, Tc, Tci, Tco, mv
    print*, qgi, qgo, qci, qco
    !print*, pc, pg
    hs0=hs1;Tg0=Tg;Tg1=Tg;Tg2=Tg1+2
    qchaenth=qchaenth+qgo
end if
!Dynamic charging characteristics during desorption stage
if (pg > pc . and. i > 0.5) then
    do while (abs(qci-qco)>0.2)
        i=i+1
        if (i>10000) then
             !print*, "infinite", i
             if (qci>qco) then
                 !print*, "(qci-qco)>1", qci, qco, i
             else if (qci<qco) then
                 !print*, "(qci-qco)<-1", qci, qco, i
             end if
             exit
        end if
        if (qci>qco) then
             !print*, "qci>qco", Tci, Tco, Tc
             Tg1=Tg; Tg=0.5*(Tg1+Tg2)
        else if (qci<qco) then
             !print*, "qci<qco", Tci, Tco, Tc
             Tg2=Tg; Tg=0.5*(Tg1+Tg2)
         !print*, "1", qci, qco, Tg, Tgi, Tgo
```

```
T=Tg; x=(MsO-Mw)/MsO
                 call solutionCpw(t, cpw)
                 Tgo=Tg-(Tg-Tgi)/exp(UAg/(Cpw*mg))
                 qgo=UAg*(Tgi-Tgo)/log((Tgi-Tg)/(Tgo-Tg))
                 call vaporenthalpy (T, hv)
                 !Compares the concentration and solubility
                 so1=2.725E-12*Tg**6-7.545E-10*Tg**5+7.502E-8*Tg**4-2.826E-
6*Tg**3-6. 49E-8*Tg**2+3. 29E-3*Tg+0. 3975
                 if (xt>sol .or. xt==sol) then
                     x = sol
                 else if (xt<sol) then
                     x=xt
                 end if
                 call enthalpy (Tg, x, hs)
                 mv0=0: mv1=1: mv=0.5*(mv0+mv1)
                 qgi=Ms1*hs1-Ms0*hs0+mv*(2500.6-Tg*2.4)
                 x=xt
                 do while (abs(qgi-qgo)>0.2)
                     i = i + 1
                     if (i>10000) then
                         !print*, "infinite", i
                         if (qci>qco) then
                              !print*, "(qgi-qgo)>1", qgi, qgo, i
                         else if (qci<qco) then
                              !print*, "(qgi-qgo)<-1", qgi, qgo, i
                         end if
                         exit
                     end if
                     if (qgi>qgo) then
                         !print*, "qgi>qgo", Tgi, Tgo, Tg
                         mv1=mv:mv=0.5*(mv0+mv1)
                     else if (qgi<qgo .or. qgi==qgo) then
                         !print*, "qgi<qgo", Tgi, Tgo, Tg
                         mv0=mv; mv=0.5*(mv0+mv1)
                     end if
                     xt = (MsO-Mw) / (MsO-mv)
                     T=Tg
                     so1=2.725E-12*Tg**6-7.545E-10*Tg**5+7.502E-8*Tg**4-
2. 826E-6*Tg**3-6. 49E-8*Tg**2+3. 29E-3*Tg+0. 3975
```

```
x = sol
                     else if (xt<sol) then
                         x=xt
                     end if
                     call enthalpy (Tg, x, hs)
                     hs1=hs;Ms1=Ms0-mv
                     qgi=Ms1*hs1-Ms0*hs0+mv*(2500.6-Tg*2.4)
                     x=xt
                     if (qgi>qgo .and. mv==0) then
                         !print*, "qgi<qgo"
                         Tg2=Tg+0.2*(Tg2-Tg1); Tg=0.5*(Tg1+Tg2)
                         T=Tg; x=(MsO-Mw)/MsO
                         call solutionCpw(t,cpw)
                         Tgo=Tg-(Tg-Tgi)/exp(UAg/(Cpw*mg))
                         qgo=UAg*(Tgi-Tgo)/log((Tgi-Tg)/(Tgo-Tg))
                         mv0=0; mv1=1; mv=0.5*(mv0+mv1)
                         qgi=Ms1*hs1-Ms0*hs0+mv*(2500.6-Tg*2.4)
                     end if
                 end do
                 if (mv>0) then
                     so1=2.725E-12*Tg**6-7.545E-10*Tg**5+7.502E-8*Tg**4-
2. 826E-6*Tg**3-6. 49E-8*Tg**2+3. 29E-3*Tg+0. 3975
                     if (xt>sol .or. xt==sol) then
                         x = sol
                     else if (xt<sol) then
                         x=xt
                     end if
                     if (Tg>59) then
                         call solpressure (Tg, x, pg)
                     else if (Tg < 59 \cdot or. Tg == 59) then
                         call solutionpressure (Tg, x, pg)
                     end if
                     x=xt
                     call waterpressure (pg, Tc)
                     qci=(Tg-Tc)*1.84*mv+mv*(2500.6-Tc*2.4)
                     T=Tc
                     call solutionCpw(T, Cpw)
```

if (xt>sol .or. xt==sol) then

```
Tco=Tc-(Tc-Tci)/exp(UAc/(Cpw*mc))
                     qco=UAc*(Tco-Tci)/log((Tc-Tci)/(Tc-Tco))
                     if (abs(qco-qci)>1) then
                         Ms1=Ms0:hs1=hs0:x=(Ms0-Mw)/Ms0
                     end if
                 else if (mv==0) then
                     qci=0;qco=0;Tg=Tg0
                     exit
                 end if
            end do
            i=1
            !print*, "2", Tg, x, Tgi, Tgo
            !print*, Tc, Tci, Tco, mv
            print*, qgi, qgo, qci, qco
            !print*, pc, pg
            Mw=Mw-mv;MsO=Ms1;hsO=hs1;TgO=Tg;Tg1=Tg
            qchaenth=qchaenth+qgo-mv*(2500.6-Tg*2.4)
            qcha1t=qcha1t+mv*(2500.6-Tg*2.4)
        end if
        !write(*,'(11(f10.6,""))'),pg,pc
    end do
    print*, qchaenth, qchalt, qchaenth+qchalt, xmax, x
    contains
    !Specific heat capacity of water and solution
    subroutine solutionCpw(T, Cpw)
    real T, Cpw, theta, cpf1, cpf2, cps
    theta=(T+273.15)/228-1
    Cpw=88.7891-120.1958*theta**0.02-
16. 9264*theta**0. 04+52. 4654*theta**0. 06+0. 10826*theta**1. 8+0. 46988*theta**8
    cpf1=0.12825+0.62934*x/100
    cpf2=58. 5225*theta**0. 02-105. 6343*theta**0. 04+47. 7948*theta**0. 06
    Cps = Cpw * (1-cpf1 * cpf2)
    end subroutine
    !Calculate the enthalpy of saturated water
    subroutine waterenthalpy (T, hw)
    real T, hw
    hw=0.6+4.18443*T
    end subroutine
    !Calculate the enthalpy of water vapor
    subroutine vaporenthalpy (T, hv)
    real T, hv
```

```
hv=2501+1.84*41.53
    end subroutine
    subroutine solutionpressure (Tg, x, pg)
    real Tg, Tk, pg, x, xmole
    xmo1e=1000*x/(42.39*(1-x))
    Tk = Tg + 273.15
    pg=10**((8.202988-0.1353801*xmo1e+0.0179222*xmo1e**2-
0.0005292*xmo1e**3) + (-1727.8+58.3845*xmo1e-
10. 208*xmo1e**2+0. 3125*xmo1e**3)/Tk+(-95014-
4701.526*xmo1e+929.081*xmo1e**2-31.766*xmo1e**3)/Tk**2)*0.133322*0.95
    end subroutine
    !New concentration solve metrix based on my proposed regression model
    subroutine solveconcentration (pc, Tg, xt)
    real pc, Tg, xt
    xt = (pc*1000/(2.099*Tg**2-238.74*Tg+7165.2))**(1/(0.0166*Tg-3.5946))
    end subroutine
    !Solve solution concentration by solution pressure and temperature,
have error near the crystallization line
    subroutine solvepressure (pg, Tg, xt)
    real pg, Tg, Tk, xmolel, xmole2, xmolet, xt, s1, s2, stemp
    Tk = Tg + 273.15
    xmo1e1=3; xmo1e2=30
    xmolet=0.5*(xmole1+xmole2)
    s1=pg/0.133322-10**(((8.202988-0.1353801*xmole1+0.0179222*xmole1**2-
0.0005292*xmo1e1**3) + (-1727.8+58.3845*xmo1e1-
10. 208*xmo1e1**2+0. 3125*xmo1e1**3) /Tk+(-95014-
4701. 526*xmole1+929. 081*xmole1**2-31. 766*xmole1**3)/Tk**2))
    s2=pg/0.133322-10**(((8.202988-0.1353801*xmole2+0.0179222*xmole2**2-
0.0005292*xmo1e2**3) + (-1727.8+58.3845*xmo1e2-
10. 208*xmo1e2**2+0. 3125*xmo1e2**3) /Tk+(-95014-
4701. 526*xmo1e2+929. 081*xmo1e2**2-31. 766*xmo1e2**3) /Tk**2))
    stemp=pg/0.133322-10**(((8.202988-0.1353801*xmolet+0.0179222*xmolet**2-
0.0005292*xmolet**3) + (-1727.8+58.3845*xmolet-
10. 208*xmolet**2+0. 3125*xmolet**3) /Tk+(-95014-
4701. 526*xmolet+929. 081*xmolet**2-31. 766*xmolet**3) /Tk**2))
    do while (abs(s1-s2)>0.01)
        if (s1*stemp<0) then
           xmole2=xmolet; xmolet=0.5*(xmole1+xmole2)
           s2=pg/0.133322-10**((8.202988-
0. 1353801*xmo1e2+0. 0179222*xmo1e2**2-0. 0005292*xmo1e2**3)+(-
```

```
1727. 8+58. 3845*xmo1e2-10. 208*xmo1e2**2+0. 3125*xmo1e2**3)/Tk+(-95014-
4701.526*xmo1e2+929.081*xmo1e2**2-31.766*xmo1e2**3)/Tk**2))
                                        stemp=pg/0.133322-10**(((8.202988-
0. 1353801*xmolet+0. 0179222*xmolet**2-0. 0005292*xmolet**3)+(-
1727.8+58.3845*xmolet-10.208*xmolet**2+0.3125*xmolet**3)/Tk+(-95014-10.208*xmolet**2+0.3125*xmolet**3)/Tk+(-95014-10.208*xmolet**2+0.3125*xmolet**3)/Tk+(-95014-10.208*xmolet**2+0.3125*xmolet**3)/Tk+(-95014-10.208*xmolet**3)/Tk+(-95014-10.208*xmolet**3)/Tk+(-95014-10.208*xmolet**3)/Tk+(-95014-10.208*xmolet**3)/Tk+(-95014-10.208*xmolet**3)/Tk+(-95014-10.208*xmolet**3)/Tk+(-95014-10.208*xmolet**3)/Tk+(-95014-10.208*xmolet**3)/Tk+(-95014-10.208*xmolet**3)/Tk+(-95014-10.208*xmolet**3)/Tk+(-95014-10.208*xmolet**3)/Tk+(-95014-10.208*xmolet**3)/Tk+(-95014-10.208*xmolet**3)/Tk+(-95014-10.208*xmolet**3)/Tk+(-95014-10.208*xmolet**3)/Tk+(-95014-10.208*xmolet**3)/Tk+(-95014-10.208*xmolet**3)/Tk+(-95014-10.208*xmolet**3)/Tk+(-95014-10.208*xmolet**3)/Tk+(-95014-10.208*xmolet**3)/Tk+(-95014-10.208*xmolet**3)/Tk+(-95014-10.208*xmolet**3)/Tk+(-95014-10.208*xmolet**3)/Tk+(-95014-10.208*xmolet**3)/Tk+(-95014-10.208*xmolet**3)/Tk+(-95014-10.208*xmolet**3)/Tk+(-95014-10.208*xmolet**3)/Tk+(-95014-10.208*xmolet**3)/Tk+(-95014-10.208*xmolet**3)/Tk+(-95014-10.208*xmolet**3)/Tk+(-95014-10.208*xmolet**3)/Tk+(-95014-10.208*xmolet**3)/Tk+(-95014-10.208*xmolet**3)/Tk+(-95014-10.208*xmolet**3)/Tk+(-95014-10.208*xmolet**3)/Tk+(-95014-10.208*xmolet**3)/Tk+(-95014-10.208*xmolet**3)/Tk+(-95014-10.208*xmolet**3)/Tk+(-95014-10.208*xmolet**3)/Tk+(-95014-10.208*xmolet**3)/Tk+(-95014-10.208*xmolet**3)/Tk+(-95014-10.208*xmolet**3)/Tk+(-95014-10.208*xmolet**3)/Tk+(-95014-10.208*xmolet**3)/Tk+(-95014-10.208*xmolet**3)/Tk+(-95014-10.208*xmolet**3)/Tk+(-95014-10.208*xmolet**3)/Tk+(-95014-10.208*xmolet**3)/Tk+(-95014-10.208*xmolet**3)/Tk+(-95014-10.208*xmolet**3)/Tk+(-95014-10.208*xmolet**3)/Tk+(-95014-10.208*xmolet**3)/Tk+(-95014-10.208*xmolet**3)/Tk+(-95014-10.208*xmolet**3)/Tk+(-95014-10.208*xmolet**3)/Tk+(-95014-10.208*xmolet**3)/Tk+(-95014-10.208*xmolet**3)/Tk+(-95014-10.208*xmolet**3)/Tk+(-95014-10.208*xmolet**3)/Tk+(-95014-10.208*xmolet**3)/Tk+(-95014-10.208*xmolet**3)/Tk+(-95014-10.208*xmolet**3)/Tk+(-95014-10.208*xmolet**3)/Tk+(-95014-10.208*xmol
4701.526*xmolet+929.081*xmolet**2-31.766*xmolet**3)/Tk**2))
                             end if
                             if (s1*stemp>0) then
                                        xmole1=xmolet:xmolet=0.5*(xmole1+xmole2)
                                        s1=pg/0.133322-10**((8.202988-
0.1353801*xmo1e1+0.0179222*xmo1e1**2-0.0005292*xmo1e1**3)+(-10.0179222*xmo1e1**3)+(-10.0179222*xmo1e1**3)+(-10.0179222*xmo1e1**3)+(-10.0179222*xmo1e1**3)+(-10.0179222*xmo1e1**3)+(-10.0179222*xmo1e1**3)+(-10.0179222*xmo1e1**3)+(-10.0179222*xmo1e1**3)+(-10.0179222*xmo1e1**3)+(-10.0179222*xmo1e1**3)+(-10.0179222*xmo1e1**3)+(-10.0179222*xmo1e1**3)+(-10.0179222*xmo1e1**3)+(-10.0179222*xmo1e1**3)+(-10.0179222*xmo1e1**3)+(-10.0179222*xmo1e1**3)+(-10.0179222*xmo1e1**3)+(-10.0179222*xmo1e1**3)+(-10.0179222*xmo1e1**3)+(-10.0179222*xmo1e1**3)+(-10.0179222*xmo1e1**3)+(-10.0179222*xmo1e1**3)+(-10.0179222*xmo1e1**3)+(-10.0179222*xmo1e1**3)+(-10.0179222*xmo1e1**3)+(-10.0179222*xmo1e1**3)+(-10.0179222*xmo1e1**3)+(-10.0179222*xmo1e1**3)+(-10.0179222*xmo1e1**3)+(-10.0179222*xmo1e1**3)+(-10.0179222*xmo1e1**3)+(-10.0179222*xmo1e1**3)+(-10.0179222*xmo1e1**3)+(-10.0179222*xmo1e1**3)+(-10.0179222*xmo1e1**3)+(-10.0179222*xmo1e1**3)+(-10.0179222*xmo1e1**3)+(-10.0179222*xmo1e1**3)+(-10.0179222*xmo1e1**3)+(-10.0179222*xmo1e1**3)+(-10.0179222*xmo1e1**3)+(-10.0179222*xmo1e1**3)+(-10.0179222*xmo1e1**3)+(-10.0179222*xmo1e1**3)+(-10.0179222*xmo1e1**3)+(-10.0179222*xmo1e1**3)+(-10.0179222*xmo1e1**3)+(-10.0179222*xmo1e1**3)+(-10.0179222*xmo1e1**3)+(-10.0179222*xmo1e1**3)+(-10.0179222*xmo1e1**3)+(-10.0179222*xmo1e1**3)+(-10.0179222*xmo1e1**3)+(-10.0179222*xmo1e1**3)+(-10.0179222*xmo1e1**3)+(-10.0179222*xmo1e1**3)+(-10.0179222*xmo1e1**3)+(-10.0179222*xmo1e1**3)+(-10.017922*xmo1e1**3)+(-10.017922*xmo1e1**3)+(-10.01792*xmo1e1**3)+(-10.01792*xmo1e1**3)+(-10.01792*xmo1e1**3)+(-10.01792*xmo1e1**3)+(-10.01792*xmo1e1**3)+(-10.01792*xmo1e1**3)+(-10.01792*xmo1e1**3)+(-10.01792*xmo1e1**3)+(-10.01792*xmo1e1**3)+(-10.01792*xmo1e1**3)+(-10.01792*xmo1e1**3)+(-10.01792*xmo1e1**3)+(-10.01792*xmo1e1**3)+(-10.01792*xmo1e1**3)+(-10.01792*xmo1e1**3)+(-10.01792*xmo1e1**3)+(-10.01792*xmo1e1**3)+(-10.01792*xmo1e1**3)+(-10.01792*xmo1e1**3)+(-10.01792*xmo1e1**3)+(-10.01792*xmo1e1**3)+(-10.01792*xmo1e1**3)+(-10.01792*xmo1e1**3)+(-10.01792*xmo1e1**3)+(-10.01792*xmo1e1**3
1727. 8+58. 3845*xmole1-10. 208*xmole1**2+0. 3125*xmole1**3) /Tk+(-95014-
4701. 526*xmo1e1+929. 081*xmo1e1**2-31. 766*xmo1e1**3) /Tk**2))
                                       stemp=pg/0.133322-10**((8.202988-
0. 1353801*xmolet+0. 0179222*xmolet**2-0. 0005292*xmolet**3)+(-
1727. 8+58. 3845*xmolet-10. 208*xmolet**2+0. 3125*xmolet**3) /Tk+(-95014-
4701. 526*xmolet+929. 081*xmolet**2-31. 766*xmolet**3) /Tk**2))
                             end if
                             if (s1*stemp==0) then
                                        s1=stemp
                             end if
                              !print*, xmolel !Check the iteration process
              xt=1-1/(1+xmole1*42.39/1000)
              end subroutine
               !Calculate the vapor pressure of saturated water
              subroutine vaporpressure (Tc, pc)
              real Tc, pc, ts
              ts=373.15/(tc+273.15)
              pc=10**(-7.90298*(ts-1)+5.02808*log10(ts)-1.3816*10**(-7.90298*(ts-1)+5.02808*log10(ts)-1.3816*10**(-7.90298*(ts-1)+5.02808*]
7)*(10**(11.344*(1-1/ts))-1)+8.1328*10**(-3)*(10**(-3.49149*(ts-1))-1)
1) +\log 10 (1013.25))/10
              end subroutine
               !Calculate vapor temperature from solution pressure using water vapor
pressure formula
               subroutine waterpressure(pg, Tc)
              real Tc, pg
              Tc=5132/(20.386-\log(pg/0.133322))-273.15
              end subroutine
               !Simple pressure formula, applicable when Tg is higher than 60
               subroutine solpressure (Tg, x, pg)
```

```
pg=0.95*(2.099*Tg**2-238.74*Tg+7165.2)*x**(0.0166*Tg-3.5946)/1000
   end subroutine
   subroutine enthalpy (Tg, x, hs) !Calculate the enthaply of solution at
each point
      integer i, j, k
      real x, Tg, m1, hs, h1, h2, hw! 0 is the inlet parameter, 1 is the outlet
parameter m is the mass flow rate h is the enthalpy
      real Xa(1,5), Ta(3,1), C(5,3), Ha(1,3), Xb(1,5), Tb(3,1), Hb(1,3)! define
the coefficient matrix of the enthalpy formula
      real a0, a1, a2 !Formula for enthalpy and temperature
      a0=-1.31231
      a1=6.17767
      a2=-5.03479
      h1=0; hw=126280
      hs=0
      h1=a0+a1*x+a2*x**2.5-(Tg+273.15)/373.15
      data ((C(i, j), i=1, 5), j=1, 3)/-66.23, 11.27, -0.80, 0.022, -0.00017, 4.58, -
0.0000000026/
         do i=1, 5
             Xa(1, i) = x**(i-1) !Concentration matrix
         end do
         do j=1, 3
             Ta(j, 1) = Tg ** (j-1)
         end do
         Ha=matmul(Xa, C)
         do i=1, 3
             hs=hs+Ha(1,i)*Ta(i,1)
         end do
          !print*, h0
   end subroutine
End program charging
```

#### Discharging process

Program discharging
Implicit none

real Tg, x, pg

```
!for subscripts, 0 indicates previous time step, 1 indicates present
time step.
    real UAg, UAc! UA value of heat exchanger in generator and condenser
    real Tgi, Tci, Tgo, Tco, Tg, Tc, T, Tdis, pc, pg, sol !Generator in, condenser
in, generator out, condenser out, generator (solution), condenser (water)
temperature, T is only the variable of subroutine
    real Ms, Mw, Mwt, mc, mg, mv, x, xt, xi, xmin, MsO, Ms1, mvmax, mvO, mv1 !Mw is the
water in solution, Mwt is the refrigerant water in water tank. xi is the
initial concentration.
    real Cps, Cpw
    real qci, qco, qgi, qgo !qci, qco, qgi, qgo is the heat exchange inside
evaporator, outside evaporator, inside absorber, ourside absorber
    real qevai, qevao, qdisi, qdiso
    real hw, hv, hs, hs0, hs1
    real TgO, Tg1, Tg2, TcO, Tc1, Tc2!Tg1 is the temperature at previous time
step, Tg2 is the temperature at next time step, only used for iteration
    integer i, j
    gevai=0;gevao=0;gdisi=0;gdiso=0
    i=0; j=0
    !print*, "please input the UA value of generator and condenser."
    !read*, UAg, UAc
    !print*, "please input the inlet temperature in the heat exchanger of
generator and condenser."
    !read*, Tgi, Tci
    !print*, "please input the mass flow rate inside the heat exchanger of
generator and condenser."
    !read*, mg, mc
    !print*, "please input the initial mass of solution and refrigerant."
    !read*, Ms, Mw
    UAg=4.4; UAc=0.8; mg=0.6; mc=0.6; Ms=80.59; Mw=38.04; Mwt=30; Tgo=0
    x=1-Mw/Ms
    !Discharging conditions
    print*, "please input the evaporation temperature"
    read*, Tc
    Tci=Tc+3
    call vaporpressure (Tc, pc)
    print*, pc
    T=Tc-10
    call solutionCpw(T, x, Cpw, Cps)
    T_{co}=T-(T-T_{ci})/\exp(UA_{c}/(C_{pw*mc}))
    qco=Cpw*mc*(Tco-Tci);qci=qco
    mv = -qco/(2500.6 - Tc*2.4)
```

```
print*, "please input the discharging temperature"
    read*, Tdis
    !Pressure difference between pg and pc affects the mass transfer
    Tg=Tdis;pg=pc-1;Tgi=Tg
    call solvepressure (pg, Tg, xt)
    xmin=xt
    print*, "xmin=", xmin
    !Initial status
    print*, "please input the initial temperature of solution"
    read*, T
    x=(Ms-Mw)/Ms; Tg0=T; Tg=T; xi=x! Fix the value of xi
    call enthalpy (Tg, x, hs)
    hs0=hs:Ms0=Ms:Ms1=Ms0
    !Heat exchange inside evaporator
    !Assume the initial value of heat exchange inside and outside the
generator to initiate the cycle
    qgo=10;qgi=100
    !Calculate gco and my
    T=T_{C}
    call solutionCpw(T, x, Cpw, Cps)
    Tco=Tc-(Tc-Tci)/exp(UAc/(Cpw*mc))
    qci=-Cpw*mc*(Tco-Tci)
    mv = -qci/(2500.6 - Tc*2.4)
    qevai=0;qevao=0;qdisi=0;qdiso=0
    qgi=0;qgo=0
    do while (x>xmin)
        !so1=2.725E-12*Tg**6-7.545E-10*Tg**5+7.502E-8*Tg**4-2.826E-6*Tg**3-
6. 49E-8*Tg**2+3. 29E-3*Tg+0. 3975
        !xt=x
        !if (xt>sol .or. xt=sol) then
        ! x=sol
        !else if (xt<sol) then
             x=xt
        !end if
        !Choose a proper pressure formula
        if (Tg>59) then
            call solpressure (Tg, x, pg)
        else if (Tg<59 \cdot or. Tg==59) then
            call solutionpressure (Tg, x, pg)
```

mvmax=mv; mv0=0; mv1=mvmax

```
end if
        ! x = x t
        !call waterpressure(pg, Tc)
        !T=Tc:Tc0=Tc
        call vaporpressure (Tc, pc)
        !print*, Tc, pc
        call waterenthalpy (T, hw)
        !Assume the temperautre difference between heat exchange fluids and
the evaporated
        Tc0=Tc+2.8;Tc1=Tc0-0.4;Tc2=Tc0+0.5
        call vaporpressure (Tc, pc)
        !print*, pc, pg
        !if ((pc-pg) < -0.1) then
             exit
        !end if
        if ((pc-pg)>1.1 \text{ and. } (Tg-Tdis)<2.6 \text{ and. } j==0) then
             !Flash evaporation considering pressure difference
            pg=pg+1.2
            call waterpressure (pg, Tc)
            T=Tc; pg=pg-1.2
             !Whether the Solubility reaches Concentration
            so1=2.725E-12*Tg**6-7.545E-10*Tg**5+7.502E-8*Tg**4-2.826E-
6*Tg**3-6. 49E-8*Tg**2+3. 29E-3*Tg+0. 3975
            if (xt>sol .or. xt==sol) then
                x = sol
            else if (xt<sol) then
                x=xt
            end if
            call solutionCpw(T, x, Cpw, Cps)
            Tco=Tc-(Tc-Tci)/exp(UAc/(Cpw*mc))
            qci=-Cpw*mc*(Tco-Tci);qco=qci
            call vaporenthalpy (T, hv)
            mv=qco/hv
            if (xt>sol .or. xt==sol) then
                x = sol
            else if (xt<sol) then
                x=xt
```

```
end if
                                                                call enthalpy (Tg, x, hs)
                                                                hs0=hs
                                                                Ms1=Ms0+mv; Tg=Tg+mv*hv/Ms1; xt=(Ms0-Mw)/(Ms0+mv)
                                                                 if (xt>sol .or. xt==sol) then
                                                                                 x = sol
                                                                else if (xt<sol) then
                                                                                x=xt
                                                                end if
                                                                call enthalpy (Tg, x, hs)
                                                                hs1=hs
                                                                qgo=Ms0*hs0-Ms1*hs1+mv*(2500-2.4*Tg)
                                                                  !Calculate the pressure with concentration in liquid phase
                                                                 if (Tg>59) then
                                                                                      call solpressure (Tg, x, pg)
                                                                else if (Tg<59 \cdot or. Tg==59) then
                                                                                      call solutionpressure (Tg, x, pg)
                                                                 end if
                                                                x=xt
                                                                  !print*, Tg, x, Tgi, Tgo, Tc
                                                                  !print*, Tci, Tco, mv, MsO, Mwt
                                                                print*, qgi, qgo, qci, qco
                                                                Tc=Tci-3; x=xt
                                           else if ((pc-pg) < 1.1 \cdot or. (Tg-Tdis) > 2.6 \cdot or. j==1) then
                                                                Ms1=Ms0*xt/xmin
                                                                x=xmin;Tg=Tdis
                                                                print*, "xmin=", xmin, "xt=", xt, "Ms1=", Ms1, "Ms0=", Ms0
                                                                call enthalpy (Tg, x, hs)
                                                                hs1=hs0
                                                                qgi=Ms0*hs0-Ms1*hs1+(Ms1-Ms0)*(2500-2.4*Tc)+4.2*(Ms1-Ms0)*(Tc-Ms0)*(Tc-Ms0)*(Tc-Ms0)*(Tc-Ms0)*(Tc-Ms0)*(Tc-Ms0)*(Tc-Ms0)*(Tc-Ms0)*(Tc-Ms0)*(Tc-Ms0)*(Tc-Ms0)*(Tc-Ms0)*(Tc-Ms0)*(Tc-Ms0)*(Tc-Ms0)*(Tc-Ms0)*(Tc-Ms0)*(Tc-Ms0)*(Tc-Ms0)*(Tc-Ms0)*(Tc-Ms0)*(Tc-Ms0)*(Tc-Ms0)*(Tc-Ms0)*(Tc-Ms0)*(Tc-Ms0)*(Tc-Ms0)*(Tc-Ms0)*(Tc-Ms0)*(Tc-Ms0)*(Tc-Ms0)*(Tc-Ms0)*(Tc-Ms0)*(Tc-Ms0)*(Tc-Ms0)*(Tc-Ms0)*(Tc-Ms0)*(Tc-Ms0)*(Tc-Ms0)*(Tc-Ms0)*(Tc-Ms0)*(Tc-Ms0)*(Tc-Ms0)*(Tc-Ms0)*(Tc-Ms0)*(Tc-Ms0)*(Tc-Ms0)*(Tc-Ms0)*(Tc-Ms0)*(Tc-Ms0)*(Tc-Ms0)*(Tc-Ms0)*(Tc-Ms0)*(Tc-Ms0)*(Tc-Ms0)*(Tc-Ms0)*(Tc-Ms0)*(Tc-Ms0)*(Tc-Ms0)*(Tc-Ms0)*(Tc-Ms0)*(Tc-Ms0)*(Tc-Ms0)*(Tc-Ms0)*(Tc-Ms0)*(Tc-Ms0)*(Tc-Ms0)*(Tc-Ms0)*(Tc-Ms0)*(Tc-Ms0)*(Tc-Ms0)*(Tc-Ms0)*(Tc-Ms0)*(Tc-Ms0)*(Tc-Ms0)*(Tc-Ms0)*(Tc-Ms0)*(Tc-Ms0)*(Tc-Ms0)*(Tc-Ms0)*(Tc-Ms0)*(Tc-Ms0)*(Tc-Ms0)*(Tc-Ms0)*(Tc-Ms0)*(Tc-Ms0)*(Tc-Ms0)*(Tc-Ms0)*(Tc-Ms0)*(Tc-Ms0)*(Tc-Ms0)*(Tc-Ms0)*(Tc-Ms0)*(Tc-Ms0)*(Tc-Ms0)*(Tc-Ms0)*(Tc-Ms0)*(Tc-Ms0)*(Tc-Ms0)*(Tc-Ms0)*(Tc-Ms0)*(Tc-Ms0)*(Tc-Ms0)*(Tc-Ms0)*(Tc-Ms0)*(Tc-Ms0)*(Tc-Ms0)*(Tc-Ms0)*(Tc-Ms0)*(Tc-Ms0)*(Tc-Ms0)*(Tc-Ms0)*(Tc-Ms0)*(Tc-Ms0)*(Tc-Ms0)*(Tc-Ms0)*(Tc-Ms0)*(Tc-Ms0)*(Tc-Ms0)*(Tc-Ms0)*(Tc-Ms0)*(Tc-Ms0)*(Tc-Ms0)*(Tc-Ms0)*(Tc-Ms0)*(Tc-Ms0)*(Tc-Ms0)*(Tc-Ms0)*(Tc-Ms0)*(Tc-Ms0)*(Tc-Ms0)*(Tc-Ms0)*(Tc-Ms0)*(Tc-Ms0)*(Tc-Ms0)*(Tc-Ms0)*(Tc-Ms0)*(Tc-Ms0)*(Tc-Ms0)*(Tc-Ms0)*(Tc-Ms0)*(Tc-Ms0)*(Tc-Ms0)*(Tc-Ms0)*(Tc-Ms0)*(Tc-Ms0)*(Tc-Ms0)*(Tc-Ms0)*(Tc-Ms0)*(Tc-Ms0)*(Tc-Ms0)*(Tc-Ms0)*(Tc-Ms0)*(Tc-Ms0)*(Tc-Ms0)*(Tc-Ms0)*(Tc-Ms0)*(Tc-Ms0)*(Tc-Ms0)*(Tc-Ms0)*(Tc-Ms0)*(Tc-Ms0)*(Tc-Ms0)*(Tc-Ms0)*(Tc-Ms0)*(Tc-Ms0)*(Tc-Ms0)*(Tc-Ms0)*(Tc-Ms0)*(Tc-Ms0)*(Tc-Ms0)*(Tc-Ms0)*(Tc-Ms0)*(Tc-Ms0)*(Tc-Ms0)*(Tc-Ms0)*(Tc-Ms0)*(Tc-Ms0)*(Tc-Ms0)*(Tc-Ms0)*(Tc-Ms0)*(Tc-Ms0)*(Tc-Ms0)*(Tc-Ms0)*(Tc-Ms0)*(Tc-Ms0)*(Tc-Ms0)*(Tc-Ms0)*(Tc-Ms0)*(Tc-Ms0)*(Tc-Ms0)*(Tc-Ms0)*(Tc-Ms0)*(Tc-Ms0)*(Tc-Ms0)*(Tc-Ms0)*(Tc-Ms0)*(Tc-Ms0)*(Tc-Ms0)*(Tc-Ms0)*(Tc-Ms0)*(Tc-Ms0)*(Tc-Ms0)*(Tc-Ms0)*(Tc-Ms0)*(Tc-Ms0)*(Tc-Ms0)*(Tc-Ms0)*(Tc-Ms0)*(Tc-Ms0)*(Tc-Ms0)*(Tc-Ms0)*(Tc-Ms0)*(Tc-Ms0)*(Tc-Ms0)*(Tc-Ms0)*(Tc-Ms0)*(Tc-Ms0)*(Tc-Ms0)*(Tc-Ms0)*(Tc-Ms
Tg)
                                                                 qgo=Ms0*hs0-Ms1*hs1+(Ms1-Ms0)*(2500-2.4*Tc)+4.2*(Ms1-Ms0)*(Tc-Ms0)*(Tc-Ms0)*(Tc-Ms0)*(Tc-Ms0)*(Tc-Ms0)*(Tc-Ms0)*(Tc-Ms0)*(Tc-Ms0)*(Tc-Ms0)*(Tc-Ms0)*(Tc-Ms0)*(Tc-Ms0)*(Tc-Ms0)*(Tc-Ms0)*(Tc-Ms0)*(Tc-Ms0)*(Tc-Ms0)*(Tc-Ms0)*(Tc-Ms0)*(Tc-Ms0)*(Tc-Ms0)*(Tc-Ms0)*(Tc-Ms0)*(Tc-Ms0)*(Tc-Ms0)*(Tc-Ms0)*(Tc-Ms0)*(Tc-Ms0)*(Tc-Ms0)*(Tc-Ms0)*(Tc-Ms0)*(Tc-Ms0)*(Tc-Ms0)*(Tc-Ms0)*(Tc-Ms0)*(Tc-Ms0)*(Tc-Ms0)*(Tc-Ms0)*(Tc-Ms0)*(Tc-Ms0)*(Tc-Ms0)*(Tc-Ms0)*(Tc-Ms0)*(Tc-Ms0)*(Tc-Ms0)*(Tc-Ms0)*(Tc-Ms0)*(Tc-Ms0)*(Tc-Ms0)*(Tc-Ms0)*(Tc-Ms0)*(Tc-Ms0)*(Tc-Ms0)*(Tc-Ms0)*(Tc-Ms0)*(Tc-Ms0)*(Tc-Ms0)*(Tc-Ms0)*(Tc-Ms0)*(Tc-Ms0)*(Tc-Ms0)*(Tc-Ms0)*(Tc-Ms0)*(Tc-Ms0)*(Tc-Ms0)*(Tc-Ms0)*(Tc-Ms0)*(Tc-Ms0)*(Tc-Ms0)*(Tc-Ms0)*(Tc-Ms0)*(Tc-Ms0)*(Tc-Ms0)*(Tc-Ms0)*(Tc-Ms0)*(Tc-Ms0)*(Tc-Ms0)*(Tc-Ms0)*(Tc-Ms0)*(Tc-Ms0)*(Tc-Ms0)*(Tc-Ms0)*(Tc-Ms0)*(Tc-Ms0)*(Tc-Ms0)*(Tc-Ms0)*(Tc-Ms0)*(Tc-Ms0)*(Tc-Ms0)*(Tc-Ms0)*(Tc-Ms0)*(Tc-Ms0)*(Tc-Ms0)*(Tc-Ms0)*(Tc-Ms0)*(Tc-Ms0)*(Tc-Ms0)*(Tc-Ms0)*(Tc-Ms0)*(Tc-Ms0)*(Tc-Ms0)*(Tc-Ms0)*(Tc-Ms0)*(Tc-Ms0)*(Tc-Ms0)*(Tc-Ms0)*(Tc-Ms0)*(Tc-Ms0)*(Tc-Ms0)*(Tc-Ms0)*(Tc-Ms0)*(Tc-Ms0)*(Tc-Ms0)*(Tc-Ms0)*(Tc-Ms0)*(Tc-Ms0)*(Tc-Ms0)*(Tc-Ms0)*(Tc-Ms0)*(Tc-Ms0)*(Tc-Ms0)*(Tc-Ms0)*(Tc-Ms0)*(Tc-Ms0)*(Tc-Ms0)*(Tc-Ms0)*(Tc-Ms0)*(Tc-Ms0)*(Tc-Ms0)*(Tc-Ms0)*(Tc-Ms0)*(Tc-Ms0)*(Tc-Ms0)*(Tc-Ms0)*(Tc-Ms0)*(Tc-Ms0)*(Tc-Ms0)*(Tc-Ms0)*(Tc-Ms0)*(Tc-Ms0)*(Tc-Ms0)*(Tc-Ms0)*(Tc-Ms0)*(Tc-Ms0)*(Tc-Ms0)*(Tc-Ms0)*(Tc-Ms0)*(Tc-Ms0)*(Tc-Ms0)*(Tc-Ms0)*(Tc-Ms0)*(Tc-Ms0)*(Tc-Ms0)*(Tc-Ms0)*(Tc-Ms0)*(Tc-Ms0)*(Tc-Ms0)*(Tc-Ms0)*(Tc-Ms0)*(Tc-Ms0)*(Tc-Ms0)*(Tc-Ms0)*(Tc-Ms0)*(Tc-Ms0)*(Tc-Ms0)*(Tc-Ms0)*(Tc-Ms0)*(Tc-Ms0)*(Tc-Ms0)*(Tc-Ms0)*(Tc-Ms0)*(Tc-Ms0)*(Tc-Ms0)*(Tc-Ms0)*(Tc-Ms0)*(Tc-Ms0)*(Tc-Ms0)*(Tc-Ms0)*(Tc-Ms0)*(Tc-Ms0)*(Tc-Ms0)*(Tc-Ms0)*(Tc-Ms0)*(Tc-Ms0)*(Tc-Ms0)*(Tc-Ms0)*(Tc-Ms0)*(Tc-Ms0)*(Tc-Ms0)*(Tc-Ms0)*(Tc-Ms0)*(Tc-Ms0)*(Tc-Ms0)*(Tc-Ms0)*(Tc-Ms0)*(Tc-Ms0)*(Tc-Ms0)*(Tc-Ms0)*(Tc-Ms0)*(Tc-Ms0)*(Tc-Ms0)*(Tc-Ms0)*(Tc-Ms0)*(Tc-Ms0)*(Tc-Ms0)*(Tc-Ms0)*(Tc-Ms0)*(Tc-Ms0)*(Tc-Ms0)*(Tc-Ms0)*(Tc-Ms0)*(Tc-Ms0)*(Tc-Ms0)*(Tc-Ms0)*(Tc-Ms0)*(Tc-Ms0)*(Tc-Ms0)*(Tc-Ms0)*(Tc-Ms0)*(Tc-Ms0)*(Tc-Ms
Tg)
                                                                 qco = (Ms1 - Ms0) * (2500 - 2.4 * Tc)
                                                                qci=qco
                                                                                        !print*, Tg, x, Tgi, Tgo, Tc
                                                                                       !print*, Tci, Tco, mv, MsO, Mwt
                                                                                      print*, x, qgi, qgo, qci, qco
                                                                                       qdisi=qdisi+qgi;qdiso=qdiso+qgo
                                           end if
```

```
Mw=Mw+mv; MsO=Ms1; hsO=hs1; TgO=Tg; TcO=Tc; xt=x; Mwt=Mwt-mv! Calculate
the new solution mass, temperature, concentration, enthalpy
        qevai=qevai+qci;qevao=qevao+qco
    print*, "qevai=", qevai, "qevao=", qevao, "qdisi=", qdisi, "qdiso=", qdiso
    contains
    !Specific heat capacity of water and solution
    subroutine solutionCpw(T, x, Cpw, Cps)
    real T, x, Cpw, theta, cpf1, cpf2, cps
    theta=(T+273.15)/228-1
    Cpw=88.7891-120.1958*theta**0.02-
16.9264*theta**0.04+52.4654*theta**0.06+0.10826*theta**1.8+0.46988*theta**8
    cpf1=0.12825+0.62934*x/100
    cpf2=58.5225*theta**0.02-105.6343*theta**0.04+47.7948*theta**0.06
    Cps = Cpw*(1-cpf1*cpf2)*(115*0.37/x-5.75)/(115*0.37/x)
    end subroutine
    !Calculate the enthalpy of saturated water
    subroutine waterenthalpy (T, hw)
    real T, hw
    hw=0.6+4.18443*T
    end subroutine
    !Calculate the enthalpy of water vapor
    subroutine vaporenthalpy (T, hv)
    real T, hv
    hv=2501+1.84*T
    end subroutine
    subroutine solutionpressure(Tg, x, pg)
    real Tg, Tk, pg, x, xmole
    xmo1e=1000*x/(42.39*(1-x))
    Tk = Tg + 273.15
    pg=10**((8.202988-0.1353801*xmo1e+0.0179222*xmo1e**2-
0.0005292*xmo1e**3) + (-1727.8+58.3845*xmo1e-
10. 208*xmole**2+0. 3125*xmole**3) /Tk+(-95014-
4701. 526*xmo1e+929. 081*xmo1e**2-31. 766*xmo1e**3) /Tk**2) *0. 133322*0. 95
    end subroutine
    !New concentration solve based on my proposed regression model
    subroutine solveconcentration (pc, Tg, xt)
    real pc, Tg, xt
    xt = (pc*1000/(2.099*Tg**2-238.74*Tg+7165.2))**(1/(0.0166*Tg-3.5946))
```

#### end subroutine

```
!Solve solution mole fraction by solution pressure and temperature
            subroutine solvepressure (pg. Tg. xt)
            real pg, Tg, Tk, xmolel, xmole2, xmolet, xt, s1, s2, stemp
            Tk = Tg + 273.15
            xmo1e1=3:xmo1e2=30
            xmolet=0.5*(xmole1+xmole2)
            s1=pg/0.133322-10**(((8.202988-0.1353801*xmole1+0.0179222*xmole1**2-
0.0005292*xmo1e1**3) + (-1727.8+58.3845*xmo1e1-
10. 208*xmole1**2+0. 3125*xmole1**3)/Tk+(-95014-
4701. 526*xmo1e1+929. 081*xmo1e1**2-31. 766*xmo1e1**3) /Tk**2))
            s2=pg/0.133322-10**(((8.202988-0.1353801*xmole2+0.0179222*xmole2**2-
0.0005292*xmo1e2**3) + (-1727.8+58.3845*xmo1e2-
10. 208*xmo1e2**2+0. 3125*xmo1e2**3) /Tk+(-95014-
4701.526*xmole2+929.081*xmole2**2-31.766*xmole2**3)/Tk**2))
            stemp=pg/0.133322-10**(((8.202988-0.1353801*xmolet+0.0179222*xmolet**2-
0.0005292*xmolet**3) + (-1727.8+58.3845*xmolet-
10. 208*xmolet**2+0. 3125*xmolet**3) /Tk+(-95014-
4701. 526*xmolet+929. 081*xmolet**2-31. 766*xmolet**3) /Tk**2))
            do while (abs(s1-s2)>0.01)
                        if (s1*stemp<0) then
                                  xmole2=xmolet:xmolet=0.5*(xmole1+xmole2)
                                  s2=pg/0.133322-10**((8.202988-
0. 1353801*xmo1e2+0. 0179222*xmo1e2**2-0. 0005292*xmo1e2**3)+(-
1727. 8+58. 3845*xmo1e2-10. 208*xmo1e2**2+0. 3125*xmo1e2**3)/Tk+(-95014-
4701. 526*xmo1e2+929. 081*xmo1e2**2-31. 766*xmo1e2**3) /Tk**2))
                                  stemp=pg/0.133322-10**(((8.202988-
0. 1353801*xmolet+0. 0179222*xmolet**2-0. 0005292*xmolet**3)+(-
1727. 8+58. 3845*xmolet-10. 208*xmolet**2+0. 3125*xmolet**3) /Tk+(-95014-
4701.526*xmolet+929.081*xmolet**2-31.766*xmolet**3)/Tk**2))
                        end if
                        if (s1*stemp>0) then
                                  xmole1=xmolet; xmolet=0.5*(xmole1+xmole2)
                                  s1=pg/0.133322-10**((8.202988-
0.1353801*xmo1e1+0.0179222*xmo1e1**2-0.0005292*xmo1e1**3)+(-10.0179222*xmo1e1**3)+(-10.0179222*xmo1e1**3)+(-10.0179222*xmo1e1**3)+(-10.0179222*xmo1e1**3)+(-10.0179222*xmo1e1**3)+(-10.0179222*xmo1e1**3)+(-10.0179222*xmo1e1**3)+(-10.0179222*xmo1e1**3)+(-10.0179222*xmo1e1**3)+(-10.0179222*xmo1e1**3)+(-10.0179222*xmo1e1**3)+(-10.0179222*xmo1e1**3)+(-10.0179222*xmo1e1**3)+(-10.0179222*xmo1e1**3)+(-10.0179222*xmo1e1**3)+(-10.0179222*xmo1e1**3)+(-10.0179222*xmo1e1**3)+(-10.0179222*xmo1e1**3)+(-10.0179222*xmo1e1**3)+(-10.0179222*xmo1e1**3)+(-10.0179222*xmo1e1**3)+(-10.0179222*xmo1e1**3)+(-10.0179222*xmo1e1**3)+(-10.0179222*xmo1e1**3)+(-10.0179222*xmo1e1**3)+(-10.0179222*xmo1e1**3)+(-10.0179222*xmo1e1**3)+(-10.0179222*xmo1e1**3)+(-10.0179222*xmo1e1**3)+(-10.0179222*xmo1e1**3)+(-10.0179222*xmo1e1**3)+(-10.0179222*xmo1e1**3)+(-10.0179222*xmo1e1**3)+(-10.0179222*xmo1e1**3)+(-10.0179222*xmo1e1**3)+(-10.0179222*xmo1e1**3)+(-10.0179222*xmo1e1**3)+(-10.0179222*xmo1e1**3)+(-10.0179222*xmo1e1**3)+(-10.0179222*xmo1e1**3)+(-10.0179222*xmo1e1**3)+(-10.0179222*xmo1e1**3)+(-10.0179222*xmo1e1**3)+(-10.0179222*xmo1e1**3)+(-10.0179222*xmo1e1**3)+(-10.0179222*xmo1e1**3)+(-10.0179222*xmo1e1**3)+(-10.0179222*xmo1e1**3)+(-10.0179222*xmo1e1**3)+(-10.0179222*xmo1e1**3)+(-10.0179222*xmo1e1**3)+(-10.0179222*xmo1e1**3)+(-10.0179222*xmo1e1**3)+(-10.0179222*xmo1e1**3)+(-10.0179222*xmo1e1**3)+(-10.0179222*xmo1e1**3)+(-10.0179222*xmo1e1**3)+(-10.0179222*xmo1e1**3)+(-10.017922*xmo1e1**3)+(-10.017922*xmo1e1**3)+(-10.01792*xmo1e1**3)+(-10.01792*xmo1e1**3)+(-10.01792*xmo1e1**3)+(-10.01792*xmo1e1**3)+(-10.01792*xmo1e1**3)+(-10.01792*xmo1e1**3)+(-10.01792*xmo1e1**3)+(-10.01792*xmo1e1**3)+(-10.01792*xmo1e1**3)+(-10.01792*xmo1e1**3)+(-10.01792*xmo1e1**3)+(-10.01792*xmo1e1**3)+(-10.01792*xmo1e1**3)+(-10.01792*xmo1e1**3)+(-10.01792*xmo1e1**3)+(-10.01792*xmo1e1**3)+(-10.01792*xmo1e1**3)+(-10.01792*xmo1e1**3)+(-10.01792*xmo1e1**3)+(-10.01792*xmo1e1**3)+(-10.01792*xmo1e1**3)+(-10.01792*xmo1e1**3)+(-10.01792*xmo1e1**3)+(-10.01792*xmo1e1**3)+(-10.01792*xmo1e1**3
1727. 8+58. 3845*xmole1-10. 208*xmole1**2+0. 3125*xmole1**3) /Tk+(-95014-
4701. 526*xmo1e1+929. 081*xmo1e1**2-31. 766*xmo1e1**3) /Tk**2))
                                  stemp=pg/0.133322-10**(((8.202988-
0. 1353801*xmolet+0. 0179222*xmolet**2-0. 0005292*xmolet**3)+(-
1727.8+58.3845*xmo1et-10.208*xmo1et**2+0.3125*xmo1et**3)/Tk+(-95014-10.208*xmo1et**2+0.3125*xmo1et**3)/Tk+(-95014-10.208*xmo1et**2+0.3125*xmo1et**3)/Tk+(-95014-10.208*xmo1et**2+0.3125*xmo1et**3)/Tk+(-95014-10.208*xmo1et**3)/Tk+(-95014-10.208*xmo1et**3)/Tk+(-95014-10.208*xmo1et**3)/Tk+(-95014-10.208*xmo1et**3)/Tk+(-95014-10.208*xmo1et**3)/Tk+(-95014-10.208*xmo1et**3)/Tk+(-95014-10.208*xmo1et**3)/Tk+(-95014-10.208*xmo1et**3)/Tk+(-95014-10.208*xmo1et**3)/Tk+(-95014-10.208*xmo1et**3)/Tk+(-95014-10.208*xmo1et**3)/Tk+(-95014-10.208*xmo1et**3)/Tk+(-95014-10.208*xmo1et**3)/Tk+(-95014-10.208*xmo1et**3)/Tk+(-95014-10.208*xmo1et**3)/Tk+(-95014-10.208*xmo1et**3)/Tk+(-95014-10.208*xmo1et**3)/Tk+(-95014-10.208*xmo1et**3)/Tk+(-95014-10.208*xmo1et**3)/Tk+(-95014-10.208*xmo1et**3)/Tk+(-95014-10.208*xmo1et**3)/Tk+(-95014-10.208*xmo1et**3)/Tk+(-95014-10.208*xmo1et**3)/Tk+(-95014-10.208*xmo1et**3)/Tk+(-95014-10.208*xmo1et**3)/Tk+(-95014-10.208*xmo1et**3)/Tk+(-95014-10.208*xmo1et**3)/Tk+(-95014-10.208*xmo1et**3)/Tk+(-95014-10.208*xmo1et**3)/Tk+(-95014-10.208*xmo1et**3)/Tk+(-95014-10.208*xmo1et**3)/Tk+(-95014-10.208*xmo1et**3)/Tk+(-95014-10.208*xmo1et**3)/Tk+(-95014-10.208*xmo1et**3)/Tk+(-95014-10.208*xmo1et**3)/Tk+(-95014-10.208*xmo1et**3)/Tk+(-95014-10.208*xmo1et**3)/Tk+(-95014-10.208*xmo1et**3)/Tk+(-95014-10.208*xmo1et**3)/Tk+(-95014-10.208*xmo1et**3)/Tk+(-95014-10.208*xmo1et**3)/Tk+(-95014-10.208*xmo1et**3)/Tk+(-95014-10.208*xmo1et**3)/Tk+(-95014-10.208*xmo1et**3)/Tk+(-95014-10.208*xmo1et**3)/Tk+(-95014-10.208*xmo1et**3)/Tk+(-95014-10.208*xmo1et**3)/Tk+(-95014-10.208*xmo1et**3)/Tk+(-95014-10.208*xmo1et**3)/Tk+(-95014-10.208*xmo1et**3)/Tk+(-95014-10.208*xmo1et**3)/Tk+(-95014-10.208*xmo1et**3)/Tk+(-95014-10.208*xmo1et**3)/Tk+(-95014-10.208*xmo1et**3)/Tk+(-95014-10.208*xmo1et**3)/Tk+(-95014-10.208*xmo1et**3)/Tk+(-95014-10.208*xmo1et**3)/Tk+(-95014-10.208*xmo1et**3)/Tk+(-95014-10.208*xmo1et**3)/Tk+(-95014-10.208*xmo1et**3)/Tk+(-95014-10.208*xmo1et**3)/Tk+(-95014-10.208*xmo1et**3)/Tk+(-95014-10.208*xmo1et**3)/Tk+(-95014-10.208*xmo1
4701.526*xmolet+929.081*xmolet**2-31.766*xmolet**3)/Tk**2))
                        end if
                        if (s1*stemp==0) then
```

```
s1=stemp
                     end if
                     !print*, xmolel !Check the iteration process
          xt=1-1/(1+xmole1*42.39/1000)
          end subroutine
          !Calculate the vapor pressure of saturated water
          subroutine vaporpressure (Tc, pc)
          real Tc, pc, ts
          ts=373.15/(Tc+273.15)
          !pc=10**(-7.90298*(ts-1)+5.02808*log10(ts)-1.3816*10**(-7.90298*(ts-1)+5.02808*log10(ts)-1.3816*10**(-7.90298*(ts-1)+5.02808*log10(ts)-1.3816*10**(-7.90298*(ts-1)+5.02808*log10(ts)-1.3816*10**(-7.90298*(ts-1)+5.02808*log10(ts)-1.3816*10**(-7.90298*(ts-1)+5.02808*log10(ts)-1.3816*10**(-7.90298*(ts-1)+5.02808*log10(ts)-1.3816*10**(-7.90298*(ts-1)+5.02808*(ts-1)+5.02808*(ts-1)+5.02808*(ts-1)+5.02808*(ts-1)+5.02808*(ts-1)+5.02808*(ts-1)+5.02808*(ts-1)+5.02808*(ts-1)+5.02808*(ts-1)+5.02808*(ts-1)+5.02808*(ts-1)+5.02808*(ts-1)+5.02808*(ts-1)+5.02808*(ts-1)+5.02808*(ts-1)+5.02808*(ts-1)+5.02808*(ts-1)+5.02808*(ts-1)+5.02808*(ts-1)+5.02808*(ts-1)+5.02808*(ts-1)+5.02808*(ts-1)+5.02808*(ts-1)+5.02808*(ts-1)+5.02808*(ts-1)+5.02808*(ts-1)+5.02808*(ts-1)+5.02808*(ts-1)+5.02808*(ts-1)+5.02808*(ts-1)+5.02808*(ts-1)+5.02808*(ts-1)+5.02808*(ts-1)+5.02808*(ts-1)+5.02808*(ts-1)+5.02808*(ts-1)+5.02808*(ts-1)+5.02808*(ts-1)+5.02808*(ts-1)+5.02808*(ts-1)+5.02808*(ts-1)+5.02808*(ts-1)+5.02808*(ts-1)+5.02808*(ts-1)+5.02808*(ts-1)+5.02808*(ts-1)+5.02808*(ts-1)+5.02808*(ts-1)+5.02808*(ts-1)+5.02808*(ts-1)+5.02808*(ts-1)+5.02808*(ts-1)+5.02808*(ts-1)+5.02808*(ts-1)+5.02808*(ts-1)+5.02808*(ts-1)+5.02808*(ts-1)+5.02808*(ts-1)+5.02808*(ts-1)+5.02808*(ts-1)+5.02808*(ts-1)+5.02808*(ts-1)+5.02808*(ts-1)+5.02808*(ts-1)+5.02808*(ts-1)+5.02808*(ts-1)+5.02808*(ts-1)+5.02808*(ts-1)+5.02808*(ts-1)+5.02808*(ts-1)+5.02808*(ts-1)+5.02808*(ts-1)+5.02808*(ts-1)+5.02808*(ts-1)+5.02808*(ts-1)+5.02808*(ts-1)+5.02808*(ts-1)+5.02808*(ts-1)+5.02808*(ts-1)+5.02808*(ts-1)+5.02808*(ts-1)+5.02808*(ts-1)+5.02808*(ts-1)+5.02808*(ts-1)+5.02808*(ts-1)+5.02808*(ts-1)+5.02808*(ts-1)+5.02808*(ts-1)+5.02808*(ts-1)+5.02808*(ts-1)+5.02808*(ts-1)+5.02808*(ts-1)+5.02808*(ts-1)+5.02808*(ts-1)+5.02808*(ts-1)+5.02808*(ts-1)+5.02808*(ts-1)+5.02808*(ts-1)+5.02808*(ts-1)+5.02808*(ts-1)+5.02808*(ts-1)+5.02808*(ts-1)+5.02808*(ts-1)+5.02808*(ts-1)+5.02808*(ts-1)+5.02808*(ts-1)+5.02808*(ts-1)+5.02808*(ts-1)+5.02808*(ts-1)+5.0280*(ts-1)+5.0280*(ts-1)+5.0280*(ts-1)+5.0280*(ts-1)+5.0280
7)*(10**(11.344*(1-1/ts))-1)+8.1328*10**(-3)*(10**(-3.49149*(ts-1))-1)
1) + \log 10 (1013.25)) / 10
          pc = exp(20.386-5132/(Tc+273.15))*0.133322
          end subroutine
          !Calculate vapor temperature from solution pressure using water vapor
pressure formula
          subroutine waterpressure (pg, Tc)
          real Tc, pg
          Tc=5132/(20.386-\log(pg/0.133322))-273.15
          end subroutine
          !Simple pressure formula, applicable when Tg is higher than 60
          subroutine solpressure (Tg, x, pg)
          real Tg, x, pg
          pg=0.95*(2.099*Tg**2-238.74*Tg+7165.2)*x**(0.0166*Tg-3.5946)/1000
          end subroutine
          subroutine enthalpy (Tg, x, hs) !Calculate the enthaply of solution at
each point
                  integer i, j, k
                  real x, Tg, ml, hs, h1, h2, hw! 0 is the inlet parameter, 1 is the outlet
parameter m is the mass flow rate h is the enthalpy
                  real Xa(1,5), Ta(3,1), C(5,3), Ha(1,3), Xb(1,5), Tb(3,1), Hb(1,3)! define
the coefficient matrix of the enthalpy formula
                  real a0, a1, a2 !Formula for enthalpy and temperature
                  a0=-1.31231
                  a1=6.17767
                  a2=-5.03479
                  h1=0:hw=126280
                  hs=0
                  h1=a0+a1*x+a2*x**2.5-(Tg+273.15)/373.15
```

```
data ((C(i, j), i=1, 5), j=1, 3)/-66.23, 11.27, -0.80, 0.022, -0.00017, 4.58, -
0. 15, 0. 0063, -0. 00014, 0. 0000011, -0. 00081, 0. 00022, -0. 000014, 0. 00000032, -
0.0000000026/
           do i=1, 5
               Xa(1, i) = x**(i-1) !Concentration matrix
           end do
           do j=1, 3
               Ta(j, 1) = Tg ** (j-1)
           end do
           Ha=matmul(Xa,C)
           do i=1, 3
               hs=hs+Ha(1, i)*Ta(i, 1)
           end do
           !print*, h0
    end subroutine
    End program discharging
```

## References

Arabi M, Dehghani MR. Measurement of solubility and density of water + lithium bromide + lithium chloride and water + lithium bromide plus sodium formate systems. International Journal of Refrigeration-Revue Internationale Du Froid, 2015,56:99-104.

Al-Ugla AA, El-Shaarawi MAI, Said SAM. Alternative designs for a 24-hours operating solar-powered LiBr-water absorption air-conditioning technology. International Journal of Refrigeration-Revue Internationale Du Froid, 2015,53:90-100.

Bales C, Nordlander S. TCA evaluation: lab measurements, modelling and system simulations 2005.

Barbieri ES, Melino F, Morini M. Influence of the thermal energy storage on the profitability of micro-CHP systems for residential building applications. Applied Energy, 2012,97:714-22.

Beckmann W. Crystallization: basic concepts and industrial applications: John Wiley & Sons; 2013.

Bi Y, Zang G, Qin L, et al. Study on the characteristics of charging/discharging processes in three-phase energy storage coupling in solar air conditioning system. Energy and Buildings, 2019,204:109456.

Chaudhari SK, Patil KR. Thermodynamic Properties of Aqueous Solutions of Lithium Chloride. Physics and Chemistry of Liquids, 2002,40(3):317-25.

Cherrad N, Ghiaus A-G. Numerical study of solar absorption heat storage system applied to Bucharest city. Building Simulation, 2021,14(3):601-16.

Choi HW, Jeong J, Kang YT. Optimal discharging of solar driven sorption thermal battery for building cooling applications. Energy, 2024,296:131087.

Conde MR. Properties of aqueous solutions of lithium and calcium chlorides: formulations for use in air conditioning equipment design. International Journal of Thermal Sciences, 2004,43(4):367-82.

Crespo A, Fernández C, Vérez D, et al. Thermal performance assessment and control optimization of a solar-driven seasonal sorption storage system for residential application. Energy, 2023,263:125382.

Ding Z, Sui Y, Lin H, et al. Experimental study on a two-stage absorption thermal battery with absorption-enhanced generation for high storage density and extremely low charging temperature (~50 °C). Applied Energy, 2024,363.

Ding Z, Sui Y, Zhai C, et al. Transient supply-demand matching and numerical parametric study of solar absorption thermal battery for space cooling. Energy Conversion and Management, 2023,288:117177.

Ding Z, Wu W. A hybrid compression-assisted absorption thermal battery with high energy storage density/efficiency and low charging temperature. Applied Energy, 2020,282:116068.

Ding Z, Wu W. A novel double-effect compression-assisted absorption thermal battery with high storage performance for thermal energy storage. Renewable Energy, 2022,191:902-18.

Ding ZX, Wu W, Chen YM, et al. Dynamic characteristics and performance improvement of a high-efficiency double-effect thermal battery for cooling and heating. Applied Energy, 2020,264.

Eisa MAR, Diggory PJ, Holland FA. A Study of the Operating Characteristics of an Experimental Absorption Cooler Using Water Lithium Bromide Ethylene-Glycol as a Ternary Working System. International Journal of Energy Research, 1988,12(3):459-72.

ElBahloul AA, Zeidan E-SB, El-Sharkawy II, et al. Recent advances in multistage sorption thermal energy storage systems. Journal of Energy Storage, 2022,45:103683.

El-Shaarawi MAI, Al-Ugla AA. Hybrid storage designs for continuous operation of solar-powered LiBr-water absorption air-conditioning. International Journal of Energy Research, 2016,40(6):791-805.

Forman C, Muritala IK, Pardemann R, et al. Estimating the global waste heat potential. Renewable and Sustainable Energy Reviews, 2016,57:1568-79.

Fumey B, Weber R, Baldini L. Sorption based long-term thermal energy storage - Process classification and analysis of performance limitations: A review. Renewable & Sustainable Energy Reviews, 2019,111:57-74.

Gao J, Xu Z. Performance evaluation of absorption thermal energy storage/transmission using ionic liquid absorbents. Energy and Built Environment, 2023,4(3):259-69.

Gao JT, Xu ZY, Wang RZ. Experimental study on a double-stage absorption solar thermal storage system with enhanced energy storage density. Applied Energy, 2020,262.

Him S, Myerson A. Metastable solution thermodynamic properties and crystal growth kinetics. Industrial & Engineering Chemistry Research, 1996,35(4):1078-84.

Hu Z, Deng Z, Gao W, et al. Experimental study of the absorption refrigeration using ocean thermal energy and its under-lying prospects. Renewable Energy, 2023,213:47-62.

Hu Z, Wan Y, Zhang C, et al. Compression-assisted absorption refrigeration using ocean thermal energy. Renewable Energy, 2022,186:755-68.

Hui L, N'Tsoukpoe KE, Lingai L. Evaluation of a seasonal storage system of solar energy for house heating using different absorption couples. Energy Conversion and Management, 2011,52(6):2427-36.

Ibrahim NI, Al-Sulaiman FA, Ani FN. Performance characteristics of a solar driven lithium bromide-water absorption chiller integrated with absorption energy storage. Energy Conversion and Management, 2017,150:188-200.

Ibrahim NI, Al-Sulaiman FA, Ani FN. Solar absorption systems with integrated absorption energy storage-A review. Renewable & Sustainable Energy Reviews, 2018,82:1602-10.

Ibrahim NI, Rehman S, Al-Sulaiman FA, et al. A systematic thermodynamic performance assessment of a solar-driven double-effect absorption chiller integrated with absorption energy storage. Applied Thermal Engineering, 2023,221:119868.

Inada T, Tomita H, Takemura F, et al. Crystallization temperature, vapor pressure, density and viscosity of lithium bromide + lithium iodide + ethylene glycol + water system for absorption refrigerators for automotive use. International Journal of Refrigeration-Revue Internationale Du Froid, 2019,100:274-83.

Itaya Y, Ichihashi N, Nagatani K, et al. Performance of absorption heat pump using fine particle slurry of LIBR crystal. HEFAT 2012, 2012.

Jin Z, Li S, Zhou R, et al. Effects of absorption pressure and temperature on NH3-H2O-LiBr-TiO2 nanofluid absorption performance and system COP. Applied Thermal Engineering, 2023,219:119353.

Khan Z, Khan Z, Ghafoor A. A review of performance enhancement of PCM based latent heat storage system within the context of materials, thermal stability and compatibility. Energy Conversion and Management, 2016,115:132-58.

Kim J, Lee H. Solubilities, vapor pressures, densities, and viscosities of the LiBr+LiI+HO(CH2)3OH+H2O system. Journal of Chemical and Engineering Data, 2001,46(1):79-83.

Koo K, Lee H, Jeong S, et al. Solubilities, vapor pressures, and heat capacities of the water + lithium bromide + lithium nitrate + lithium iodide + lithium chloride system. International Journal of Thermophysics, 1999,20(2):589-600.

Krolikowska M, Hofman T. The influence of bromide-based ionic liquids on solubility of {LiBr (1) + water (2)} system. Experimental (solid + liquid) phase equilibrium data. Part 1. Journal of Molecular Liquids, 2019,273:606-14.

Le Pierres N, Huaylla F, Stutz B, et al. Long-term solar heat storage process by absorption with the KCOOH/H2O couple: Experimental investigation. Energy, 2017,141:1313-23.

Li Y, Zhang X, Xiao F, et al. Modeling and management performances of distributed energy resource for demand flexibility in Japanese zero energy house. Building Simulation, 2023,16(11):2177-92.

Lin Y, Xiao F, Wang S. A novel modified LiCl solution for three-phase absorption thermal energy storage and its thermal and physical properties. International Journal of Refrigeration, 2021,130:44-55.

Liu X, Geng K, Lin B, et al. Combined cogeneration and liquid-desiccant system applied in a demonstration building. Energy and Buildings, 2004,36(9):945-53.

Liu W, Chen G, Yan B, et al. Hourly operation strategy of a CCHP system with GSHP and thermal energy storage (TES) under variable loads: A case study. Energy and Buildings, 2015,93:143-53.

Lui H, N'Tsoukpoe KE, Luo L. Evaluation of a seasonal storage system of solar energy for house heating using different absorption couples. Energy Conversion and Management, 2011,52(6):2427-36.

Luo J, Joybari MM, Panchabikesan K, et al. Performance of a self-learning predictive controller for peak shifting in a building integrated with energy storage. Sustainable Cities and Society, 2020,60:102285.

Mago PJ, Luck R. Evaluation of a base - loaded combined heating and power system with thermal storage for different small building applications. International Journal of Energy Research, 2013,37(2):179-88.

Mehari A, Wang R, Xu Z. Experimental analysis of a high-performance open sorption thermal storage system with absorption-crystallization-adsorption processes. Energy Conversion and Management, 2022,270:116220.

Mehari A, Wang RZ, Xu ZY. Evaluation of a high-performance evaporative cooler-assisted open three-phase absorption thermal energy storage cycle for cooling. Applied Energy, 2022,325:119818.

Mehari A, Xu Z, Wang R. Thermal energy storage using absorption cycle and system: A comprehensive review. Energy Conversion and Management, 2020,206:112482.

Mehari A, Xu ZY, Wang RZ. Thermally-pressurized sorption heat storage cycle with low charging temperature. Energy, 2019,189.

Mehari A, Xu ZY, Wang RZ. Thermodynamic evaluation of three-phase absorption thermal storage in humid air with energy storage density over 600 kWh/m3. Energy Conversion and Management, 2022,258:115476.

Monnin C, Dubois M, Papaiconomou N, et al. Thermodynamics of the LiCl+H2O system. Journal of Chemical and Engineering Data, 2002,47(6):1331-6.

N'Tsoukpoe KE, Le Pierres N, Luo L. Experimentation of a LiBr-H2O absorption process for long-term solar thermal storage: Prototype design and first results. Energy, 2013,53:179-98.

N'Tsoukpoe KE, Le Pierres N, Luo L. Numerical dynamic simulation and analysis of a lithium bromide/water long-term solar heat storage system. Energy, 2012,37(1):346-58.

N'Tsoukpoe KE, Liu H, Le Pierres N, et al. A review on long-term sorption solar energy storage. Renewable & Sustainable Energy Reviews, 2009,13(9):2385-96.

Said SAM, El-Shaarawi MAI, Siddiqui MU. Alternative designs for a 24-h operating solar-powered absorption refrigeration technology. International Journal of Refrigeration, 2012,35(7):1967-77.

Stokes JR, Telford JH, Williamson AM. The flowability of ice suspensions. Journal of Rheology, 2005,49(1):139-48.

Sui Y, Ding Z, Zhai C, et al. Crystallization-free and low-cost deep eutectic solvents for absorption thermal battery utilizing ultra-low-grade energy. Energy Conversion and Management, 2023,284:116984.

Tang H, Wang S, Li H. Flexibility categorization, sources, capabilities and technologies for energy-flexible and grid-responsive buildings: State-of-the-art and future perspective. Energy, 2021,219:119598.

Tang H, Wang S. Life-cycle economic analysis of thermal energy storage, new and second-life batteries in buildings for providing multiple flexibility services in electricity markets. Energy, 2023,264:126270.

Ulrich J, Strege C. Some aspects of the importance of metastable zone width and nucleation in industrial crystallizers. Journal of Crystal Growth, 2002,237:2130-5.

Wang K, Abdelaziz O, Kisari P, et al. State-of-the-art review on crystallization control technologies for water/LiBr absorption heat pumps. International Journal of Refrigeration-Revue Internationale Du Froid, 2011,34(6):1325-37.

Wang L, Liu X, Yang Z, et al. Experimental study on a novel three-phase absorption thermal battery with high energy density applied to buildings. Energy, 2020,208:118311.

Wang S, Hoes P-J, Hensen JL, et al., editors. Investigating the use cases of a novel heat battery in Dutch residential buildings. Building Simulation; 2023: Springer.

Weber R, Dorer V. Long-term heat storage with NaOH. Vacuum, 2008,82:708–16.

Wen T, Luo Y, Sheng L. Experimental study on the corrosion behavior and regeneration performance of KCOOH aqueous solution. Solar Energy, 2020,201:638-48.

Wu W, Ding Z, Sui Y, et al. Comparative dynamic performance of hybrid absorption thermal batteries using H2O/1,3-dimethylimidazolium dimethylphosphate. Energy Conversion and Management, 2021,228:113690.

Wu W, Bai Y, Huang H, et al. Charging and Discharging Characteristics of Absorption Thermal Energy Storage using Ionic-liquid-based Working Fluids. Energy, 2019:116126.

Wu W, Wang B, Shi W, et al. An overview of ammonia-based absorption chillers and heat pumps. Renewable and Sustainable Energy Reviews, 2014,31:681-707.

Wu W, You T, Leung M. Screening of novel water/ionic liquid working fluids for absorption thermal energy storage in cooling systems. International Journal of Energy Research, 2020,44(12):9367-81.

Xu ZY, Wang RZ. A sorption thermal storage system with large concentration glide. Energy, 2017,141:380-8.

Xu ZY, Wang RZ. Absorption seasonal thermal storage cycle with high energy storage density through multi-stage output. Energy, 2018,167:1086-96.

Yoon J, Kwon O. Cycle analysis of air-cooled absorption chiller using a new working solution. Energy, 1999,24(9):795-809.

Youssef Z, Delahaye A, Huang L, et al. State of the art on phase change material slurries. Energy Conversion and Management, 2013,65:120-32.

Yu N, Wang R, Lu Z, et al. Evaluation of a three-phase sorption cycle for thermal energy storage. Energy, 2014,67:468-78.

Yu N, Wang RZ, Wang LW. Sorption thermal storage for solar energy. Progress in Energy and Combustion Science, 2013,39(5):489-514.

Yuan J, Cui C, Xiao Z, et al. Performance analysis of thermal energy storage in distributed energy system under different load profiles. Energy Conversion and Management, 2020,208:112596.

Yuan J, Xiao Z, Zhang C, et al. A control strategy for distributed energy system considering the state of thermal energy storage. Sustainable Cities and Society, 2020,63:102492.

Zang X, Li H, Wang S. Optimal design of energy-flexible distributed energy systems and the impacts of energy storage specifications under evolving time-of-use tariff in cooling-dominated regions. Journal of Energy Storage, 2023,72:108462.

Zhang F, Yin Y, Zhang X. Performance analysis of a solar-driven liquid desiccant cooling system with solution storage under adjustable recirculation ratio. Solar Energy, 2018,172:32-45.

Zhang H, Yi Y, Xie X. Performance and optimization of absorption heat exchanger under different flow rate ratio conditions. Applied Thermal Engineering, 2022,212:118603.

Zhang X, Li M, Shi W, et al. Experimental investigation on charging and discharging performance of absorption thermal energy storage system. Energy Conversion and Management, 2014,85:425-34.

Zhang Y, Wang R. Sorption thermal energy storage: Concept, process, applications and perspectives. Energy Storage Materials, 2020,27:352-69.

Zhou J, Zhang X, Xiao F. Study on heat and mass transfer characteristics of internally-cooled hollow fiber membrane-based liquid desiccant dehumidifiers. Applied Thermal Engineering, 2022,212:118525.